In Vitro Evaluation of Medical Gases and Sprays Using Nasal Replicas

by

John Chen

A thesis submitted in partial fulfillment of the requirements for the degree of

Doctor of Philosophy

Department of Mechanical Engineering
University of Alberta

Abstract

The objective of this thesis is to describe two new methodologies for evaluating medical gas and nasal spray delivery, respectively, *in vitro* using nasal replicas. The first half of the body of thesis describes the development of a new *in vitro* benchtop method for evaluating the delivery of medical gases across different modalities (e.g. delivery of pulsed vs. continuous flows). The second half describes the design and validation of an idealized nasal replica which mimics the average *in vitro* and *in vivo* regional deposition of nasal sprays in adult subjects.

Chapter 1 provides the background and justification for the use of nasal replicas in *in vitro* evaluations of the delivery of medical gas and nasal sprays. For medical gases, previous researchers have relied on highly simplified geometries, which cannot simulate physiologically accurate pressure changes in the airways during breathing, nor account for the effect of intersubject variability in patient airway geometries on gas delivery. For sprays and aerosols, an extensive history of *in vitro* studies evaluating regional intranasal deposition using realistic nasal replicas already exists. These studies tend to be performed with a single geometry, which is unlikely to be representative of the population at large, highlighting the potential utility of a standardized idealized geometry which would mimic average regional *in vivo* and *in vitro* deposition across an adult population.

Chapter 2 introduces the problem of equivalency between continuous flow and pulse flow delivery of supplemental oxygen and describes the development of a predictive *in vitro* model for inhaled oxygen delivery using a set of realistic nasal airway replicas.

Experiments are reported to compare pulse flow delivery from a commercial portable oxygen concentrator (POC) with continuous flow from a compressed oxygen cylinder. A volume-averaged fraction of inspired oxygen (FiO2) was calculated by numerically integrating inhaled oxygen flow rates sampled at the exit of each replica and used as a common basis for comparison between continuous and pulse flow. Pulse flow delivered consistently lower FiO2 than continuous flow rates equivalent to nominal pulse flow settings. To the extent that the POC triggered successfully at the start of inhalation, intersubject variability in airway geometries had a minimal effect on FiO2. Testing using airway replicas was also useful in identifying cases of impaired device function or failure.

Chapter 3 investigates the relative performance of four POCs both against each other and against continuous flow oxygen using a single realistic nasal replica which had a reliably high triggering pressure and which delivered a medium FiO2 compared to the full replica set. Oxygen delivery to the deep lung was also analyzed *in silico* by combining *in vitro* oxygen concentration waveforms over time and a single-path mathematical model of the lungs. Significant differences in POC performance based on FiO2 were found between continuous and pulse flow, and between pulse modes in different POCs at the same nominal device setting. *In silico* simulations revealed that while pulse flow is a more efficient mode of delivery than continuous flow, continuous flow ultimately delivers a greater volume of oxygen per breath.

Chapter 4 describes the manufacture and *in vitro* validation experiments needed for the development of an idealized nasal replica, based on a geometry previously developed using

in silico simulations. This replica, manufactured in plastic, was validated by comparing with regional deposition in realistic, sectioned nasal replicas obtained from *in vitro* deposition experiments and in previously published *in vivo* data. A commercial nasal spray pump was actuated repeatably into each realistic or idealized nasal replica under a steady inspiratory flow at two different orientations. It was found that regional deposition in the idealized replica agreed well with average regional deposition in the realistic replicas and with previously published *in vivo* gamma scintigraphy data.

In Chapter 5, an aluminum version of the idealized nasal replica from Chapter 4 was used in order to facilitate further *in vitro* experiments with a wider set of intranasal drug formulations (one aqueous solution, one aqueous suspension and one propellant-based formulation). Good agreement was seen between deposition measured using the idealized replica and *in vivo* deposition patterns for all three nasal drug formulations that were tested.

Chapter 6 summarizes the main conclusions of the thesis and provides possible directions for future research.

Preface

This thesis is written in manuscript format and consists of 4 main chapters and 6 chapters in total.

Chapter 1 contains significant material from the journal article "Chen J, Martin AR, Finlay WH. Recent In Vitro and In Silico Advances in the Understanding of Intranasal Drug Delivery. Current Pharmaceutical Design [Internet]. 2021;27:1482–97". I carried out the literature review and wrote the manuscript drafts. Andrew Martin and Warren Finlay provided feedback and assisted with writing the manuscript.

Chapter 2 has been previously published as the journal article "Chen JZ, Katz IM, Pichelin M, Zhu K, Caillibotte G, Noga ML, et al. Comparison of pulsed versus continuous oxygen delivery using realistic adult nasal airway replicas. International Journal of COPD. 2017;12:2559–71". All authors contributed to conceptualizing and planning the study. I carried out the experiments, performed all the data analysis and wrote the drafts of the manuscript. Michelle Noga provided patient nasal airway computed tomography scans and checked the scans for anatomical abnormalities. Kaixian Zhu provided portable oxygen concentrator oxygen concentration data. Ira Katz, Marine Pichelin, Georges Caillibotte, Kaixian Zhu, Andrew Martin, Warren Finlay and Michelle Noga reviewed and provided feedback on the manuscript.

Chapter 3 has been previously published as the journal article "Chen JZ, Katz IM, Pichelin M, Zhu K, Caillibotte G, Finlay WH, et al. In vitro–in silico comparison of pulsed oxygen delivery from portable oxygen concentrators versus continuous flow oxygen delivery.

Respiratory Care. 2019;64:117–29". Ira Katz, Marine Pichelin, George Caillibotte, Andrew Martin, Warren Finlay and I contributed to the study design. Andrew Martin and I performed the literature review. I performed the bulk of the data collection and analysis, with contributions from Ira Katz, Marine Pichelin and Georges Caillibotte and Kaixian Zhu. I wrote the manuscript drafts. Ira Katz, Marine Pichelin, Georges Caillibotte, Kaixian Zhu, Andrew Martin, and Warren Finlay reviewed and provided feedback on the manuscript.

Chapter 4 has been previously published as a journal article, "In vitro assessment of an idealized nose for nasal spray testing: Comparison with regional deposition in realistic nasal replicas. International Journal of Pharmaceutics [Internet]. Elsevier; 2020;582:119341". Minor nomenclature changes have been made to ensure consistency with the other thesis chapters. All authors contributed to the study design. Milad Kiaee assisted me with preparing the idealized nasal replica for 3D printing. I performed the literature review and performed the data collection I performed bulk of the data analysis with contributions from the other authors. I wrote the manuscript drafts. Andrew Martin, Warren Finlay and Milad Kiaee reviewed the manuscript and provided feedback.

Chapter 5 will be submitted as a peer-reviewed journal article. All authors contributed to the study design. I performed the literature search and data collection. I performed the bulk of the data analysis with contributions from the other authors. I wrote the manuscript draft. Andrew Martin and Warren Finlay reviewed the manuscript and provided feedback.

To my parents.

Acknowledgments

I consider myself truly fortunate to have had my two supervisors as wonderful as Professors Andrew Martin and Warren Finlay, to whom I would like to offer my deepest and sincerest expressions of gratitude. Their knowledge, guidance, advice, support and the professional opportunities they have provided me have been invaluable to me throughout my PhD and will continue to remain so throughout my career. Many thanks also to the final member of my supervisory committee, Professor Reinhard Vehring, for his insightful feedback and for his enthusiasm in putting the fruits of this research into practical use.

My fellow labmates, colleagues and co-authors, Kelvin Duong, Scott Tavernini, Conor Ruzycki, Kineshta Pillay, Solbee Seo have been nothing but friendly, helpful, capable and considerate. The work in this thesis would not have been possible without their cooperation. My gratitude also extends the many past members of the Aerosol Research Lab of Alberta who I have been fortunate enough to meet in my career, all of whom are, either happily or sadly, no longer at the University.

I would like to further extend my thanks to my gracious hosts at Air Liquide, Ira Katz, Marine Pichelin, Georges Caillibotte and Spyros Montesantos. Their scientific acumen propelled my research forward and their warmth and candor were a comfort to me as I was navigating an unfamiliar country.

I am also grateful for the help of the Mechanical Engineering Shop staff, who persisted in offering their services despite the difficult ongoing circumstances. The careful proofreading

services and generous encouragement provided by Luba Slabyj are also gratefully appreciated.

Finally, I would also like to thank my parents, who have been consistently kind, patient and supportive over the course of this degree.

Table of Contents

Abstract ii

Preface v

Acknowledgments viii

List of Tables xv

List of Figures xvii

Chapter 1: Introduction 1

1.1 Nasal replicas and medical gases 2

1.2 Nasal replicas and medical aerosols 3

1.3 Review of *in vitro* nasal replica literature 5

1.3.1 Intranasal delivery of medical gases 6

1.3.2 Intranasal deposition of medical aerosols and sprays 7

1.4 Summary 13

Chapter 2: Comparison of Pulsed vs. Continuous Oxygen Delivery using Realistic Adult Nasal Airway Replicas 15

2.1 Introduction 15

2.2 Methods 17

2.2.1 Realistic airway replicas 17

2.2.2 Representative breathing patterns 20

2.2.3 Flow rate and oxygen concentration measurements 22

2.2.3 Calculation of SF and PF FiO2 23

2.2.4 Measurement of pulse characteristics 24

2.2.4 Prediction of PF FiO2 25

2.2.5 Pressure drop measurements 27

2.3 Results 27

2.3.1 Oxygen concentration and flow rate waveforms 27

2.3.2 SF and PF FiO2 31

2.3.3 Pressure drop measurements 33

2.3.4 Predicting PF FiO2 34

2.4 Discussion 35

2.4.1 Comparison with the in vivo case 36

2.4.2 Breath detection in POCs 37

2.4.3 Comparison of SF and PF delivery 38

2.4.4 Predicting PF FiO2 based on pulse characteristics 41

2.4.5 Study limitations 42

2.5 Conclusions 44

Chapter 3: In Vitro-In Silico Comparison of Pulsed Oxygen Delivery from Portable Oxygen Concentrators versus Continuous Flow Oxygen Delivery 45

3.1 Introduction 45

3.2 Methodology 47

3.2.2 Selection of a representative airway replica 47

3.2.3 Airway experiments 48

3.2.4 Calculation of volume-averaged tracheal FiO2 51

3.2.5 Measurement of pulse characteristics 53

3.2.6 Prediction of PF volume-averaged FiO2 53

3.2.7 Mathematical modelling of oxygen transport through the conducting airways 54

3.3 Results 57

3.3.1 Comparisons of POC performance 57

3.3.2 Prediction of volume-averaged tracheal FiO2 using measured pulse characteristics 61

3.3.3 Mathematical modelling 63

3.4 Discussion 66

3.5 Conclusions 69

Chapter 4: In Vitro Assessment of an Idealized Nose for Nasal Spray Testing: Comparison with Regional Deposition in Realistic Nasal Replicas 71

4.1 Introduction 71

4.2. Methodology 73

4.2.1 CT scan segmentation and smoothing 73

4.2.2 Creation of the realistic nasal replicas 74

4.2.3 Creation of the idealized geometry using CFD 75

4.2.4 Manufacture of the idealized replica 76

4.2.5 Deposition experiments 77

4.3. Results 81

4.4. Discussion 86

4.5 Conclusion 88

Chapter 5: *In Vitro* Regional Deposition of Nasal Sprays in an Idealized Nasal Inlet: Comparison with *In Vivo* Gamma Scintigraphy 90

5.1. Introduction 90

5.2. Materials and Methods 92

5.2.1 Intranasal drug formulations 92

5.2.2 Actuation parameters 93

5.2.2 Experimental procedure 95

5.2.3 In vitro data analysis 96

5.3. Results 97

5.3.1. NasalCrom 97

5.3.2. Nasonex 101

5.3.3. QNASL 103

5.4. Discussion 106

5.5. Conclusions 108

Chapter 6: Conclusions 110

6.1 Summary 110

6.2 Directions for future research 112

References 114

Appendix A 131

List of Tables

Table 2.1. Airway replica volumes and surface areas for 15 adult nasal airway replicas. ... 19

Table 2.2. Breathing parameters of representative breathing profiles for COPD patients at rest, doing light exercise and while asleep. ... 22

Table 2.3. SimplyGo oxygen pulse characteristics at pulse flow (PF) setting numbers of 2.0 and 6.0 using various breathing frequencies. ... 25

Table 2.4. Number of breathing replicas indicating incomplete pulse delivery out of the total number of replicas used to calculate volume-averaged fraction of inspired oxygen (FiO2) at each setting/breathing pattern combination. ... 31

Table 3.1. Specifications for portable oxygen concentrators used in this study. ... 49

Table 3.2. Breathing parameters of representative breathing profiles for COPD patients at rest, doing light exercise and while asleep. ... 49

Table 3.3. Cylindrical airway dimensions of tracheobronchial airways at each generation in lung model. ... 55

Table 3.4. Subgroups with statistically similar volume-averaged tracheal FiO2 ($P > 0.05$) segregated by device setting/CFO flow and breathing pattern. For each breathing pattern, subgroups are separated with a line and have significant differences ($P < 0.05$) in volume-averaged FIO2 with other subgroups. Additionally, for each breathing pattern subgroups are arranged by magnitude of FiO2, in descending order, top to bottom. The One G4 does not feature device settings above 3.0, and only the SimplyGo features pulse settings up to 6.0. ... 60

Table 4.1. Actuation parameters for automated repeatable mechanic actuation of the nasal spray pump. Obtained from Doughty et al. (2011) [78]. Actuation force is the maximum force during the actuation, rise time is the time required to reach the maximum force while actuating the pump, release velocity is the velocity in releasing the pump and expected stroke length is the maximum displacement of the pump during actuation. Each parameter is a mean value averaged across 20 healthy adults..... 78
Table 5.1. Actuation parameters for automated repeatable mechanic actuation of the nasal spray pump obtained from Doughty et al. (2011) [78]. Actuation force is the maximum force during the actuation, rise time is the time required to reach the maximum force while actuating the pump, release velocity is the velocity in releasing the pump and expected stroke length is the maximum displacement of the pump during actuation. Each parameter is a mean value averaged across 20 healthy adults..... 94

List of Figures

Figure 2.1. Solid 3D nose–throat airways of the 15 replicas tested in the present study. Note: The top row displays airways derived from MRI, while the bottom two rows display airways derived from CT images. 20

Figure 2.2. Schematic of experimental apparatus. Arrows indicate direction of oxygen flow. 21

Figure 2.3. Example oxygen mole fraction and flow rate waveforms indicating (a) steady flow (SF) oxygen delivery, (b) complete pulse delivery and (c) incomplete pulse delivery. Waveforms in (a) and (c) were taken from experiment using Subject CT7; waveforms in (b) were from experiment using Subject CT9. Positive flow rates indicate inspiration; negative flow rates indicate expiration. Numbers indicate points of interest in the oxygen waveform (see Results section). 28

Figure 2.4. Comparison of volume-averaged FiO2 at SF 2.0 L/min and PF setting number 2.0, averaged over n different airway replicas, measured using 5 successive breaths per replica. For exercise and rest breathing patterns, n = 15. For the sleep breathing pattern combined with Pulse Mode, n = 12; with Sleep Mode, n = 14. Error bars indicate one standard deviation. 32

Figure 2.5. Comparison of volume-averaged FiO2 at SF 6.0 L/min and PF setting number 6.0, averaged over n different airway replicas, measured using 5 successive breaths per replica. For exercise and rest breathing patterns, n = 15. For the sleep breathing pattern combined with Pulse Mode, n = 11; with Sleep Mode, n = 14. Error bars indicate one standard deviation. 33

Figure 2.6. Pressure drop measured at the cannula as a function of inspiratory flow rate, averaged over 3 measurements. Error bars represent one standard deviation. 34
Figure 2.7. Comparison of volume-averaged FiO2 estimated from airway experiments and FiO2 predicted using pulse characteristics. Airway experiment FiO2 values were averaged over n airway replicas, measured using 5 successive breaths per replica. For all experiments with exercise and rest breathing patterns, n = 15. For the sleep breathing pattern combined with Pulse Mode setting number 2.0, n = 12; with Pulse Mode setting number 6.0, n = 11; with Sleep Mode setting numbers 2.0 and 6.0, n = 14. Error bars indicate one standard deviation. 35
Figure 3.1. Comparison of volume-averaged FiO2 using Subject MRI2 with mean volume-averaged FiO2 across 15 airway replicas. Data for both pulse deliveries from a Philips SimplyGo portable oxygen concentrator and continuous flow oxygen from a stationary source of compressed oxygen are included. Error bars indicate one standard deviation. 48
Figure 3.2. Photograph of commercial portable oxygen concentrators tested in this study manufactured by Phillips Respironics and Inogen. 50
Figure 3.3. Schematic of apparatus used in experiments involving airway replicas. Arrows indicate direction of oxygen flow. 51
Figure 3.4. Sample flow and oxygen fraction waveforms generated by the experimental apparatus for pulsed delivery of oxygen..... 52
Figure 3.5. Volume-averaged FiO2 and pulse characteristics for each of the tested portable oxygen concentrators and continuous flow oxygen across three breathing patterns. FiO2

values were averaged over 5 consecutive breaths. Other pulse characteristics averaged over 20 consecutive breaths. Error bars indicate one standard deviation. 58
Figure 3.6. Pulse flow curves generated by the O2 Conserver Testing System for each POC at setting 2 for each device and breathing frequency of 17 breaths per minute. 59
Figure 3.7. Comparisons of volume-averaged FiO2 measured in airway experiments with volume-averaged FiO2 predicted using pulse characteristics. Vertical error bars indicate one standard deviation of FiO2 determined from airway experiments over five consecutive breaths. Horizontal error bars indicate one standard deviation of FiO2 determined using pulse characteristics over twenty consecutive breaths. Identity line shown for comparison. 63
Figure 3.8. Sample output of MATLAB simulation (SimplyGo Mini, exercise breathing pattern, device setting 5). The Trachea line represents oxygen concentration passing the trachea over time determined by the in vitro experiments. Oxygen passing generation 14 enters the gas exchange regions of the lung. 64
Figure 3.9. Volumes of oxygen passing through the trachea, passing into the alveolar region, and the ratio of these two numbers (i.e. a measure of the fraction of the oxygen passing the trachea that reaches the alveolar region) for all tested portable oxygen concentrators and continuous flow oxygen. 65
Figure 4.1. Three computer rendered perspective views of the idealized replica. Anatomical regions of interest are labeled as follows: 1) nasal entrance, 2) turbinates, 3) olfactory region, 4) nasopharynx. 77
Figure 4.2. Schematic of experimental setup. 80

Figure 4.3. Regional deposition of cromolyn sodium in 5 realistic nasal replicas (number indicates the subject number; L for left nostril; R for right nostril) delivered in separate experiments into the right and left nostrils of each replica, administered at an angle of 60° from the horizontal, inhalation flow rate of 7.5 L/min. Three experimental repeats were done for each geometry; error bars indicate one standard deviation. 82
Figure 4.4. Regional deposition of cromolyn sodium in 5 realistic nasal replicas (number indicates the subject number; L for left nostril; R for right nostril) delivered in separate experiments into the right and left nostrils of each replica, administered at an angle of 45° from the horizontal, inhalation flow rate of 7.5 L/min. Three experimental repeats were done for each geometry; error bars indicate one standard deviation. 83
Figure 4.5. Comparison of regional deposition of cromolyn sodium in realistic vs. idealized nasal replicas (60°). Deposition in realistic replicas presented as average over all realistic nasal replicas. Error bars for the realistics indicate one standard deviation (measured across geometries). Error bars for the idealized also indicate one standard deviation (variation in three experimental repeats). 84
Figure 4.6. Comparison of regional deposition of cromolyn sodium in realistic vs. idealized nasal replicas (45°). Deposition in realistic replicas presented as average over all realistic nasal replicas. Error bars indicate one standard deviation (measured across geometries). Error bars for the idealized also indicate one standard deviation (variation in three experimental repeats). 85

Figure 4.7. Comparison of regional deposition of cromolyn sodium in realistic vs. idealized nasal replicas (60°) with y-axis magnified to show olfactory and filter deposition. Values below our range of detectability are not shown. 85
Figure 4.8. Comparison of regional deposition of cromolyn sodium in realistic vs. idealized nasal replicas (45°) with y-axis magnified to show olfactory and filter deposition. Values below our range of detectability are not shown. 86

Chapter 1: Introduction

The nose can be an attractive pathway for delivery of medical therapeutics. Delivery of medical gases such as oxygen and nitric oxide via nasal is ubiquitous in both the hospital and outpatient settings, and the large nasal mucosa surface is well-suited for topical drug delivery and the high permeability and low enzymatic activity of the nasal epithelium makes it an attractive target for systemic delivery of vaccines, pain medication, and other drugs [1–5].

Despite the invaluable feedback that they would generate, the cost and time requirements of *in vivo* studies are such that these studies are rarely conducted in the early stages of product development. Accordingly, predictive *in vitro* test methods which aim to expedite early product development have been developed [6]. These methods work by providing rapid feedback to developers narrowing down parameter spaces for the clinical phase of development. *In vitro* assessments with realistic or idealized nasal replicas offer a middle ground between *in vitro* assessment methods based on the measurement of the chemical or physical properties of the therapeutic in question and *in vivo* studies.

An ideal nasal replica strikes a balance between ease of use and ability to quickly iterate on the one hand, and anatomical fidelity and ability to reproduce *in vivo* data on the other. The objective of this thesis is to extend the usefulness of such replicas in two novel ways with respect to the assessment of delivery and dosing of medical gases and nasal sprays. Chapters 2 and 3 describe how realistic 3D printed nasal replicas can be integrated into an *in vitro* test bench setup to evaluate the delivery of supplemental oxygen, which not only

allows comparisons between different delivery modalities on the basis of the fraction of inspired oxygen (FiO2), but also gives insight into the dynamic oxygen concentrations at the trachea and potential modes of failure in portable oxygen concentrators (POCs). Chapters 4 and 5 focus on the design and validation of an idealized nasal replica mimicking both average *in vivo* and *in vitro* regional deposition across a wide patient population in several nasal spray products, aimed towards both researchers and industry for use in the drug development process.

1.1 Nasal replicas and medical gases

An emerging use case for nasal replicas is in the *in vitro* evaluation of the concentration of inhaled medical gases. For example, the delivery of oxygen in long term oxygen therapy (LTOT) has historically been provided as a continuous, steady flow supplied to the patient interface, typically via nasal cannula [4]. More recently, intermittent delivery methods triggered by a patient's breathing have been developed as portable or cost saving alternatives [5–7]. Portable oxygen concentrators (POCs) are devices developed relatively recently in response to demand for a lightweight, portable source of supplemental oxygen [5]. POCs commonly incorporate intermittent delivery methods to conserve oxygen. While most frequently prescribed to patients needing LTOT, POCs can play a role in any application requiring a source of supplemental oxygen. For example, POCs have been evaluated as a possible solution to supplemental oxygen requirements in military settings and high-altitude environments [8–10].

LTOT has historically been provided as a continuous, steady flow supplied to the patient interface and is typically prescribed in litres per minute [8]. The challenge of establishing equivalence between continuous flow oxygen (CFO) and nominal pulse flow device settings on different devices is well known and provides motivation for the development of physiologically representative testing methods [7,11]. Here, *in vitro* methods based on nasal replicas offer an advantage with regards to speed, reproducibility and cost when compared with *in vivo* protocols looking to capture a similar data set. Testing with a large number of different replicas can also aid in accounting for variability in the airway geometry of different patients more easily; i.e. intersubject variability [12]. In addition, the precise control of breathing patterns possible in benchtop experiments eliminates a significant source of variance that may be present during *in vivo* studies. Use of nasal replicas also enables real-time monitoring of gas concentrations at different points in the airway during breathing, which would otherwise require invasive procedures to establish *in vivo*.

1.2 Nasal replicas and nasal sprays

As a pathway for administration of topical medical sprays, the intranasal route can be optimal for targeting a wide variety local or systemic conditions. The large nasal mucosa surface is well-suited for topical drug delivery and the high permeability and low enzymatic activity of the nasal epithelium makes it an attractive target for systemic administration of vaccines, pain medication, and other drugs [1–3]. In many applications, a broad coating of drug in the nasal mucosa is sufficient or preferable for effective drug delivery. However, in some cases, such as in chronic sinusitis and nasal polyposis, targeting to the middle and superior meatuses is important [16–18]. In addition, the olfactory region has received

considerable attention as a promising route for direct drug delivery to the brain via the olfactory nerve, bypassing the blood-brain-barrier [19]. In addition to the pharmacokinetic properties of the therapeutic agent, nose-to-brain drug delivery is also influenced by the deposition pattern within the nasal cavity, volume and method of administration, and physical properties of the formulation that can influence drug pathways to the brain [20].

A United States Food and Drug Administration (FDA) draft guidance on nasal spray devices recommends *in vitro* testing of the physical properties of aqueous nasal sprays and nasal pressurized metered dose inhalers, such as reproducibility of plume characteristics, dose repeatability, and droplet size distribution (which define the characteristics of the particle cloud as it enters the nasal cavity and the likelihood of deposition by inertial impaction into the nasal walls) as a way to assess bioavailability and bioequivalence [6,18,21,22]. For both solution-based and suspension-based formulations, these tests are recommended as means to assess bioavailability and bioequivalence of different intranasal devices, since these tend to be reproducible and thus discriminating between different products, and, for solution-based formulations, are considered sufficient to evaluate bioequivalence without supplementary *in vivo* studies [6].

The use of nasal replicas offers a middle ground between *in vitro* assessment methods based on spray-property measurement and *in vivo* experiments in humans, allowing researchers to approximate the *in vivo* behaviour of medical sprays and quickly assess how each of the physical properties of the spray influence deposition and the relative importance of each property. With this information, researchers can then specify the parameter space to

be used in the often costly and expensive process of conducting clinical trials. *In vitro* benchtop testing using realistic 3D-printed nasal replicas based on airway geometries obtained from magnetic resonance imaging (MRI) or computerized tomography (CT) scans have proven invaluable in providing a fast, convenient and non-invasive research and development tool that can be used prior to clinical studies [12,21–23].

Nasal replicas, to varying degrees, reproduce the anatomy of the nasal cavity, with various trade-offs exiting between ease of manufacture, simplicity of the replica geometry and representativeness of *in vivo* deposition of the agent in question. Thus, an ideal replica would be easy to use, easy to manufacture and generate a deposition pattern which would be representative, on average, of the *in vivo* data taken from a broad section of the relevant population.

1.3 Review of *in vitro* nasal replica literature

One of the first attempts to construct an anatomically accurate model of the human nasal airway was described by Guilmette and Gagliano in an attempt to overcome the limitations of morphometric data taken from cadavers [26,27]. Subsequently, this model, based on a magnetic resonance imaging (MRI) scan of a healthy adult male human originally collected in 1989, became a standard in several subsequent studies, demonstrating the potential usefulness of a standardized geometry. However, this standardized replica would most preferably mimic average deposition across different subjects, instead of being limited to the geometry of a single particular individual which is unlikely to be representative of the wider population.

With the introduction of high-resolution imaging, computer-controlled machining techniques and 3D-printing techniques such as rapid prototyping, the ability of researchers to accurately reconstruct even the fine details of the nasal airways has recently taken a decisive step forward [28]. Thanks to the increasing ease and prevalence of 3D printing, *in vitro* nasal replica studies have become increasingly more feasible and their recent history is marked by an increasing anatomical fidelity of the replicas in use.

1.3.1 Intranasal delivery of medical gases

To account for device triggering, the anatomical dead space of the upper airways and other *in vivo* phenomena, benchtop evaluation of medical gas delivery must include an appropriate volume upstream of a test lung, or breath simulation instrument, to simulate the nares and the conducting airways. Bliss et al. (1999) used a highly simplified model of the upper airways in their benchtop setup to investigate the nominal equivalency of continuous flow oxygen (CFO) and demand oxygen delivery systems (DODS) in L/min [29]. They found that there was no equivalency in terms of fraction of inspired oxygen (FiO2) between CFO and DODS, which could be partially explained by the effect of pooling at lower respiratory frequencies in the anatomical reservoir during the end of the expiratory phase of breathing. The discovery of this pooling effect is one advantage that usage of nasal airway replicas has over simply evaluating performance based on nominal oxygen flow rates alone. In a follow-up study in 2004, the same authors investigated factors affecting performance in a wider range of DODS devices, with a focus on maximum output [6]. They confirmed that DODS and CFO did not deliver equivalent oxygen as measured by FiO2, and that the

maximum output between devices differed greatly, implying possible clinical implications when prescribing oxygen.

Zhou and Chatburn examined the effect of elimination of the anatomic reservoir on FiO2 in continuous flow oxygen delivery [30]. They found that FiO2 was reduced in breathing in which the pooling effect of the anatomic reservoir was removed. In those breathing waveforms, expiratory flow was not allowed to slowly decay to zero, which shortened the period of time in which expiratory flow was sufficiently low to permit supplemental oxygen to pool in the nasal airway.

1.3.2 Intranasal deposition of medical aerosols and sprays

In Cheng et al. (2002), both total deposition of monodisperse aerosol particles (1 to 9 μm) and regional deposition from four nasal spray pumps were assessed [31]. Foo et al. studied regional nasal deposition using a much larger parameter space that included, in addition to spray angle and particle size, administration angle (angle of spray nozzle relative to the horizontal), viscosity and inhalation flow rate [32]. The former study is noteworthy for being one of the first to systematically examine intranasal deposition *in vitro* using a realistic nasal replica, while the wide parameter space in the latter study allows the resultant deposition data to be analyzed in terms of trends across both administration and spray angles.

Guo et al. also investigated the effect of breathing pattern and formulation on regional deposition. Here, the replica was constructed based on a male cadaver, in contrast to the replicas based on *in vivo* imaging in the two aforementioned studies [33]. The inside of the

replica was coated in a mixture of dish liquid detergent and acetone to minimize re-entrainment, migration, and dripping of impacted droplets. Realistic breathing patterns were also obtained and generated using a breathing simulation system. These breathing patterns (fast and slow) were used alongside constant flows during administration to assess the effect that inspiration flow profiles might have on deposition patterns.

Kundoor and Dalby later introduced an innovative, inexpensive and quantitative colourimetry-based method for easy visualization of nasal spray deposition without the need for radiolabeling or time-consuming chemical assays [34]. First, the authors coated a transparent silicone nasal replica (Koken Co., Ltd.) using Sar-Gel (a water sensitive paste which changes colour from white to purple upon contact with liquid water). After administering the drug, the replica was photographed and regions of colour change could be quantified. The areas of colour change within each section of the replica could then be compared to the total area of colour change, allowing for quantification of the regional deposition of the spray. Preliminary regional deposition data in three nasal sprays revealed high deposition in the region of the replica anterior to the nasal valve, with some turbinate deposition and little to no olfactory deposition. The authors also evaluated the deposition pattern of a nasal nebulizer, which they found to be much more effective at depositing drug in the posterior region of the nasal cavity while covering a much larger surface area. Inspiratory flow rate had minimal influence on deposition pattern, corroborating the work done in Guo et al. (2005) and Foo et al. (2007) [32,33].

Using the same experimental methodology, the authors then conducted a more in-depth study investigating the effect of administration and formulation variables on nasal spray deposition, including head tilt angle, droplet size distribution, spray geometry, nasal insertion depth and administration angle [35]. In general, it was found that administration angle and head tilt angle had a greater effect than nozzle insertion depth. Tilting the head backwards (while maintaining constant administration angle measured relative to the nasal replica) tended to increase deposition in the turbinates, whereas tilting the head forwards increased deposition in the anterior region near the nasal valve. For low administration angles (≤45°), droplets were better able to penetrate the nasal valve, but it was also found that decreasing the administration angle tended to reduce the total overall area of deposition, with drug tending to pool in the bottom of the replica. With respect to formulation variables, the authors found that the widest spray angle, lowest particle size formulation maximized the total coverage within the nose, but they did not give further information as to the regional distribution of the deposited drug.

A later study by Pu et al. using the Kundoor and Dalby methodology examined the effect of various viscosity enhancers in nasal sprays on spray properties (droplet size distribution and spray angle) and regional deposition [36]. They found that in general, a narrow spray angle gave greater posterior deposition, but also that the type of viscosity enhancer (in this study Avicel and hydroxypropyl methylcellulose (HPMC)), more than the viscosity itself, had a significant impact on the deposition pattern. Formulations prepared with HPMC dramatically shifted deposition to the posterior regions of the replica when compared with the Avicel formulations.

Xi et al. improved on the original technique of Kundoor and Dalby by introducing correlations between the intensity of SarGel colour change and the mass of applied liquid water [34,37]. Whereas the original methodology could only detect the presence or absence of water deposited in an area, this modification also allowed for quantification of the amount of water, and therefore the amount of drug, within any given area. In this study, the authors assessed deposition in the olfactory region of the nose using a set of four nasal spray pumps and four nasal nebulizers. They found that only a small portion of the nasal spray droplets (up to 4.6%) reached the olfactory region of the nose, with most being deposited near the nasal valve region. For the nebulizers, they found that total deposition decreased when compared to the spray pumps, with a significant fraction exiting the nasopharyngeal region. Although more droplets were able to penetrate the nasal valve, they were not able to deposit in the olfactory region in significant amounts. The authors observed more posterior deposition when switching to a point-release method that injected nebulized aerosols at a specific point in the nostril, with up to 9% of the dose reaching the olfactory region. The same authors used the same in vitro methodology to later compare delivery of nebulized aerosol particles to the olfactory region using the bi-directional delivery technique with standard delivery [38]. To simulate bi-directional delivery *in vitro*, the authors modified a nasal replica from a previous study by sealing the entrance to the nasopharynx [37]. The authors found significantly increased deposition of nebulized aerosol in the upper regions of the nasal cavity when the bi-directional technique was used. For the bi-directional case, there were significant differences in the deposition pattern of each nasal passage: the nasal passage having exiting flow displayed significantly more

dispersed distributions. Finally, they noted that increasing inhalation flow rate increased the olfactory dose while decreasing the total nasal dose, which they attributed to the more prominent roles of sedimentation and interception in particle deposition at the particle sizes considered in the study (~3 μm).

Kelly et al. developed several nasal replicas using a rapid prototyping method called stereolithography, based on the same MRI scans originally described in Swift et al. (1992) in order to assess the differences that the replica manufacturing technique would impose on total deposition efficiency of monodisperse aerosols (1 to 10 μm) [39,40]. In general, they found substantial differences in deposition efficiencies between replicas based on the same MRI geometry but manufactured using different methods. Replicas manufactured using stereolithography showed lower deposition efficiency than previous data, and increasing the resolution of the stereolithography process tended to decrease deposition efficiency. The authors concluded that factors influenced by their choice of manufacturing method, such as surface roughness and the use of assembly plates (in which the replica is constructed out of thin plates rather than as one continuous object), would have a significant effect on the total deposition efficiency. However, with the increasing resolution possible with contemporary additive manufacturing methods, discrepancies between realistic nasal replicas made using different modern rapid prototyping methods are expected to be minimal.

Schroeter et al. later performed regional deposition experiments using a sectioned version of the Kelly geometry, separated into six distinct regions: the nasal vestibule and valve, the

anterior turbinates, the olfactory region, the posterior turbinates and the nasopharynx [41]. In general, deposition, particularly in the anterior valve and vestibule regions, tended to increase with particle size.

Hughes et al. describe the development of two sectioned replicas with the goal of creating a repeatable, reliable testing capability for nasal drug delivery [42]. To validate the replica, the authors performed *in vitro* regional deposition measurements using a commercially available nasal spray pump. A number of head tilt and administration angles were also tested to assess their effects on deposition. For this combination of replica and spray pump, most of the drug (approximately 60 to 80%, depending on the angles chosen) tended to deposit in the valve/vestibule region, with the remainder depositing in the anterior and posterior turbinates in equal proportion, and with no drug reaching the nasopharyngeal region. Turbinate deposition was maximized when the replica was tilted slightly backwards at an angle of 23° and the administration angle set at 60° from the horizontal. This replica was later used by Shah et al. to compare deposition patterns of different devices and formulations in vitro and in vivo [43]. It was also used later in Shah et al. (2013) to determine a set of administration parameters (administration angle, head tilt angle, etc.) that roughly reflected deposition patterns of aqueous nasal sprays observed in vivo using a half-factorial design of experiments [44]. For the resultant deposition pattern, approximately 60% of the dose deposited anterior to the nasal valve, and 20% of the dose reached the turbinates, with the remainder dripping out of the replica or depositing in the nasopharyngeal region.

Another standardized geometry has been proposed by Liu et al., who describe a process for creation of a standardized geometry by averaging the geometric characteristics of 30 healthy adult nasal airways [45]. This geometry, dubbed the Carleton-Civic geometry, was then manufactured using rapid prototyping techniques. Regional and total deposition were assessed by passing a monodisperse aerosol (1.74 to 9.14 μm) into the geometry at steady inspiratory flow rates. Total deposition tended to lie at the lower extreme of the available in vivo data for identical values of the impaction parameter (defined as the product of the volumetric flow rate and the square of the aerodynamic particle diameter). This was likely due to the averaging procedure, which averaged a set of replicas based on geometrical parameters, rather than averaging deposition data taken in individual replicas. Kiaee et al. suggest that the low deposition of the Carleton-Civic standardized geometry when compared with *in vivo* data might be due to the nonlinearity of regional deposition as a function of the geometric characteristics of the geometry [46]. Therefore, one would not expect a linear average of the geometric features of a set of replicas to produce the average regional deposition in that set. Regional deposition data revealed that most deposition in the nasal cavity occurred in the anterior area of the nasal cavity near the nasal valve.

1.4 Summary

Benchtop *in vitro* experiments using simplified and realistic nasal replicas are used to evaluate the delivery of both medical gases and nasal sprays. For medical gases, the dearth of studies done with realistic nasal replicas provides an opening for this thesis to investigate the effect of anatomical accuracy on gas delivery. In addition, the impact of intersubject variability of real patient airway geometries on variability in medical gas delivery can also

be assessed by using a wide selection of replicas, something which is impossible to do for simplified geometries. These topics will be the focus of Chapters 2 and 3. Although nasal replicas are more widespread in the study of medical sprays, the wide range of *in vitro* replicas in usage has indicated a need for the creation of a standardized geometry mimicking average regional deposition, of which efforts are already underway to develop and which is the subject of Chapters 4 and 5. Chapter 6 will summarize the results of the preceding chapters and look forward at potential future avenues of research which build from the work of this thesis.

Chapter 2: Comparison of Pulsed vs. Continuous Oxygen Delivery using Realistic Adult Nasal Airway Replicas

2.1 Introduction

Portable oxygen concentrators (POCs) are devices developed relatively recently in response to demand for a lightweight, portable source of supplemental oxygen [5]. While most frequently prescribed to patients needing long-term oxygen therapy (LTOT), POCs can play a role in any application requiring a source of supplemental oxygen. For example, POCs have been evaluated as a possible solution to supplemental oxygen requirements in military settings and high altitude environments [8–10]. A recent study showed that chronic obstructive pulmonary disease (COPD) patients requiring LTOT generally prefer a single source POC over a combined stationary and portable oxygen source both in the home and during activity, citing the practicality of the system as its main advantage [47].

POCs primarily deliver oxygen in one of two modes: steady flow (SF) and pulse flow (PF), with the most recent generation of lightweight devices (<5 lb) offering only PF mode [23,24]. While SF remains the more straightforward of the two options, continuous delivery throughout the breath leads to a significant fraction of delivered oxygen being lost to the ambient air, never reaching the patient's lungs [5]. In contrast, PF aims to improve efficiency by limiting oxygen delivery only to times when patient inspiration can be detected, and delivering oxygen as a bolus, or pulse, early in the breath so that the fraction of oxygen exhaled from the anatomical dead space is reduced.

Ideally, PF modes provide a volume of oxygen for inhalation equivalent to the volume of supplemental oxygen inhaled at a given SF rate. In light of this, oxygen delivery at varied PF settings for commercial POCs is frequently interpreted as nominally equal to that which would be achieved at equivalent SF rates; for example, a PF setting of 1.0 corresponds to an SF rate of 1.0 L/min, a PF setting of 2.0 to SF rate of 2.0 L/min, etc [48]. However, the total oxygen volume administered over a complete breathing cycle is typically less for PF than SF, owing to the efficiencies gained by synchronizing oxygen delivery with patient inspiration.

Since PF/SF equivalency is dependent upon a number of shifting variables, conclusively demonstrating such equivalency can be a difficult task [49]. Furthermore, as standards of equivalency may currently vary between manufacturers, different POC devices may deliver different volumes of oxygen at nominally the same PF setting [5]. While some clinical studies have suggested equivalence of PF and SF oxygen delivery, others have reported differences [7,47–49]. Recent studies have shown that in pairs of nominally equivalent PF/SF settings, PF fraction of inspired oxygen (FiO2) was consistently lower than SF FiO2 [6,7,27,50].

For evaluating administration of medical aerosols to the lungs, *in vitro* benchtop testing using realistic or idealized 3D-printed airway replicas has proven valuable in providing a fast, convenient, and noninvasive research and development tool compared to *in vivo* studies [12,21–23]. These realistic airway replicas, derived from medical imaging, are more representative of human upper airways compared with highly simplified geometries that

have been previously used for evaluating inhaled concentrations of medical gases [30,54]. Testing with multiple replicas can aid in accounting for variability in the airway geometry of different patients; that is, intersubject variability [12]. In addition, benchtop experiments permit precise control of simulated breathing patterns, eliminating a significant source of variance that may be present during in vivo human studies.

To our knowledge, no work has been done to date comparing the differences between SF and PF oxygen administration from POCs using realistic airway replicas. Accordingly, the primary aims of the present study are to develop a predictive in vitro model for inhaled oxygen delivery using a set of 15 realistic adult nasal airway replicas, and then to compare SF and PF for a widely used commercial POC. To this end, we developed a testing protocol that measures the real-time oxygen concentration at the outlet (trachea) of the airway replica, which can then be integrated with the instantaneous inspiratory flow rate to determine a volume-averaged FiO2 over the course of inspiration. Volume-averaged FiO2 can be used as a common basis for comparison between nominally equivalent settings of SF and PF. We further aimed to develop an algorithm to estimate PF FiO2 based on pulse characteristics, tidal volume, and upper airway volume. These estimated values can be compared with FiO2 values derived from oxygen concentration measurements.

2.2 Methods

2.2.1 Realistic airway replicas

Fifteen adult nasal airway replicas built in acrylic plastic using rapid prototyping were used in the present study. Each replica included air passages starting from the nares through the

entrance to the trachea. Five of the airway replicas were based on magnetic resonance (MR) images as previously reported, while the remaining ten replicas were based on a new set of anonymized high-resolution computed tomography (CT) scans acquired retrospectively from patients scanned for clinical purposes unrelated to the nasal passage, at the University of Alberta Hospital, with Health Research Ethics Board approval [55]. All CT scans were reviewed by an expert radiologist and the nasal passage considered normal. CT scans were segmented using Mimics software (Materialise, USA) and replicas were built using a 3D printer (Invision SR, 3D Systems, USA). Segmented 3D airways based on both the MR and CT images are presented in Figure 2.1. Geometric parameters for each of the fifteen replicas were obtained using MeshLab (Visual Computing Laboratory, Istituto di Scienza e Tecnologie dell'Informazione, Italy) and ParaView (Kitware, Clifton Park, NY, USA). These parameters are shown in Table 2.1.

Table 2.1. Airway replica volumes and surface areas for 15 adult nasal airway replicas.

Subject	Sex	Age (years)	Volume (cm^3)	Surface area (cm^2)
MRI2	F	---	44.6	287
MRI5	F	---	35.9	235
MRI6	M	---	50.1	313
MRI8	M	---	47.3	289
MRI9	M	---	45.3	250
CT1	M	60	60.0	343
CT2	F	50	73.1	315
CT3	M	57	59.2	320
CT4	M	54	71.9	349
CT5	M	60	50.1	280
CT6	F	72	59.1	321
CT7	M	62	56.3	308
CT8	M	63	61.9	326
CT9	M	27	48.1	276
CT10	F	56	53.2	265

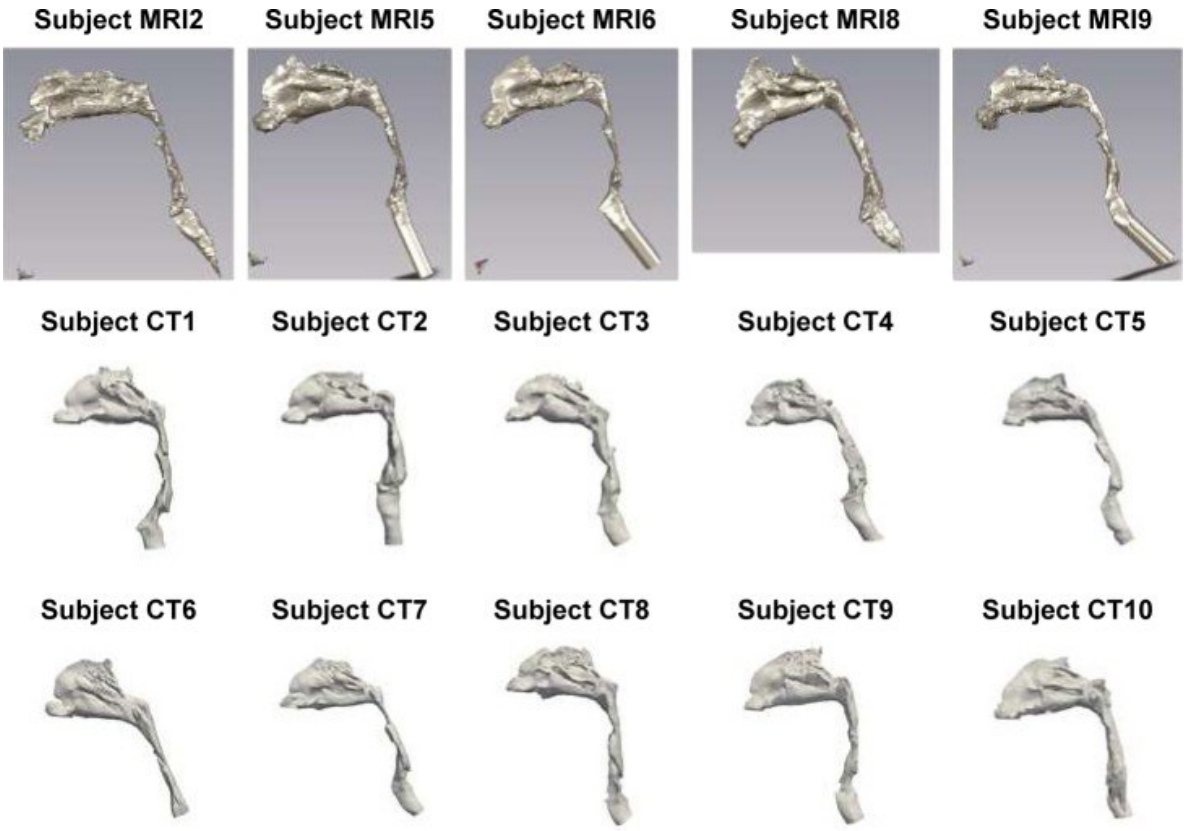

Figure 2.1. Solid 3D nose–throat airways of the 15 replicas tested in the present study. Note: The top row displays airways derived from MRI, while the bottom two rows display airways derived from CT images.

2.2.2 Representative breathing patterns

To simulate tidal breathing, airway replicas were connected to a lung simulator (ASL 5000 Breathing Simulator; IngMar Medical, Pittsburgh, PA), as shown schematically in Figure 2.2. Plastic tubing with 22 mm internal diameter connected the replica outlet to the lung simulator. The total internal volume of this tubing was 135 cm^3, representative of the conducting airway volume from the trachea to the gas exchange regions of the lungs for an average adult with a 3L functional residual capacity [56].

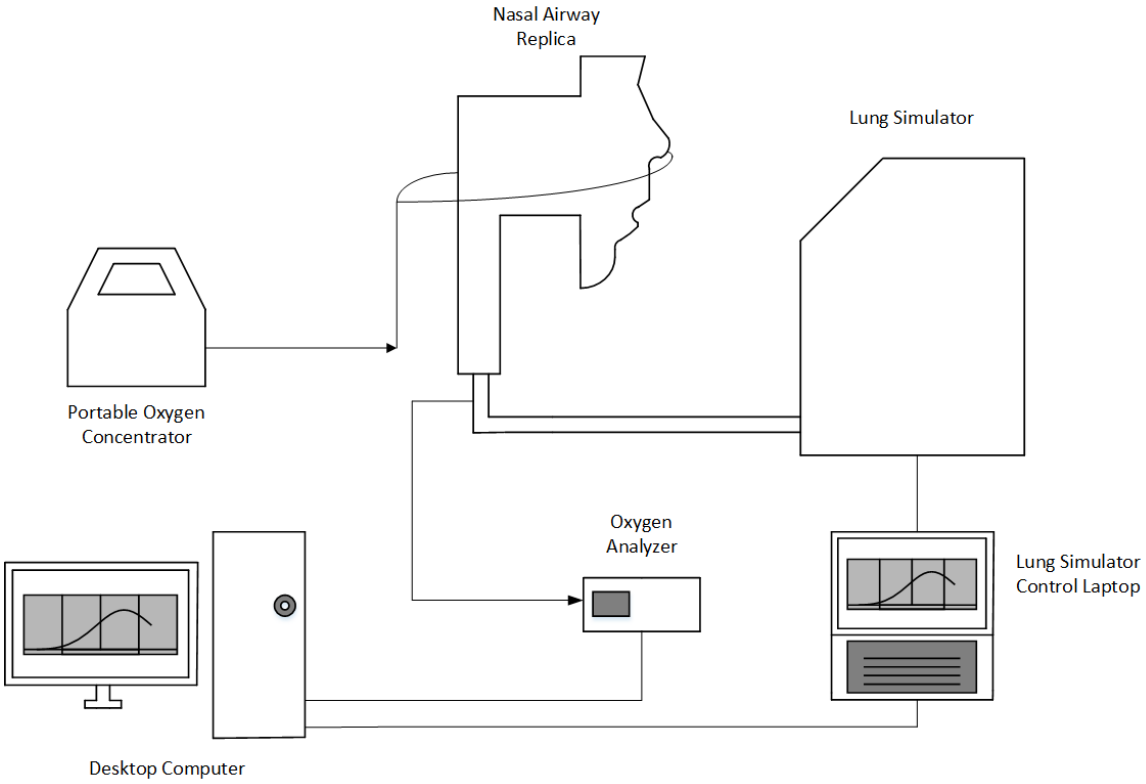

Figure 2.2. Schematic of experimental apparatus. Arrows indicate direction of oxygen flow.

To capture a range of activity levels in daily life, we used three different breathing patterns representative of a COPD patient on LTOT at rest, doing light exercise and while asleep. Inspiratory and expiratory phases of the breath were represented using sinusoidal flow patterns with one half sinusoid for inspiration and another half sinusoid for expiration. Sinusoidal breathing patterns have been used previously to approximate human breathing [57–61]. Inspiration and expiration flow rates were derived using tidal volume (V_T), inspiratory time (T_I), expiratory time (T_E) and breathing frequency (f). Values of each of these parameters for the three breathing patterns are shown in Table 2.2. The rest and exercise breathing parameters were chosen based on average values reported previously by

Chatila et al [62]. for 10 patients with COPD at baseline (rest) and while on low SF rate (2.5-6 L/min) oxygen while performing light exercise on a cycle ergometer. Parameters for the sleep breathing pattern were chosen based on average values measured by Hudgel et al. for 13 COPD patients while asleep [63].

Table 2.2. Breathing parameters of representative breathing profiles for COPD patients at rest, doing light exercise and while asleep.

	Rest	Exercise	Sleep
Tidal volume, VT (mL)	640	800	520
Inspiratory time, TI (s)	1.20	0.96	1.79
Expiratory time, TE (s)	2.33	1.77	2.93
Breathing frequency, f (breaths min^{-1})	17	22	13

2.2.3 Flow rate and oxygen concentration measurements

Experiments were carried out using a Philips SimplyGo POC (Philips Respironics, Murrysville, PA, USA) and a cylinder source of 100% oxygen (Praxair Canada). A test lung simulated the three different breathing patterns, each for approximately 50 breathing cycles. Oxygen delivery in each of the replicas via a nasal cannula (Hudson RCI adult nasal cannula; Teleflex Medical, Research Triangle Park, NC, USA) was first tested at SF rates from the cylinder source of 2.0 and 6.0 L/min, and then at nominal PF settings of 2.0 and 6.0. Once positioned, the nasal cannula was held in the same position over the course of the experiment. The SimplyGo features two different PF operating modes: Pulse Mode and Sleep Mode. Sleep Mode is similar to Pulse Mode, but features more sensitive breath detection, lower pulse amplitude and longer pulse duration aimed to improve comfort

during sleeping. The sleep breathing pattern was tested using both Pulse Mode and Sleep Mode in order to comprehensively evaluate potential device performance.

The volume of the chamber of the test lung was recorded during simulated breathing at a sampling frequency of 512 Hz using the ASL 5000 software. Oxygen concentrations were measured using a GA-200 CO2 and O2 Gas Analyzer (iWorx, Dover, NC, USA), and were corrected for delay and time constant, which was done by approximating the concentration as a first order system and following methods outlined in Langer et al [61]. We assumed that the step response of the gas analyzer could be well approximated by a first order exponential function. The time constant for this exponential function, which is defined as the time required for the response of the system to reach 63% of its final value as the result of a step increase, was measured to be 227 ms in preliminary experiments by rapidly switching supply to the gas analyzer via a three-way stopcock between two different gas mixtures of known concentration (in this case, air and 100% oxygen).

2.2.3 Calculation of SF and PF FiO2

The flow rate of oxygen passing through the trachea over time was calculated by multiplying inspiration flow rate, known at each time point, with measured real-time oxygen concentrations at the same time point. Inspiration start and end times were identified as times when flow rates crossed 0. These oxygen flow rates were then numerically integrated using the trapezoidal rule from the start to the end of inspiration to determine a volume of oxygen inhaled per breath. V_T was also calculated from inspiration flow rates using a similar procedure. The volume of inhaled oxygen was then divided by V_T

to obtain a volume-averaged value for FiO2 for that breath. FiO2 for each combination of replica and oxygen delivery condition was taken as the average of five consecutive breaths after a steady state in expiratory oxygen concentration was observed (at least 50 breaths). Variability between average FiO2 values obtained in experiments repeated on separate days of testing was found in preliminary testing to be of similar magnitude as variability between individual breaths.

2.2.4 Measurement of pulse characteristics

A 1130 Series O_2 Conserver Testing System (Hans Rudolph Inc., Shawnee, KS, USA) was used to obtain oxygen pulse volumes, durations and delays for both the 2.0 and 6.0 settings of the POC using the breathing frequency of each breathing patterns shown in Table 2.3. The SimplyGo was connected to the testing system using a standard 2.1 mm single lumen cannula. Data was recorded as the average of ten successive pulses for each breathing pattern/setting combination. Variance around reported averages was very small. The oxygen concentration of the pulse itself was measured to be 94% across all breathing pattern/setting combinations.

Table 2.3. SimplyGo oxygen pulse characteristics at pulse flow (PF) setting numbers of 2.0 and 6.0 using various breathing frequencies.

Breath Frequency	f = 13			*f = 17*			*f = 22*		
Pulse setting	Pulse Volume (ml)	Pulse Delay (ms)	Pulse Duration (ms)	Pulse Volume (ml)	Pulse Delay (ms)	Pulse Duration (ms)	Pulse Volume (ml)	Pulse Delay (ms)	Pulse Duration (ms)
Pulse Mode 2.0	23.8	110	291	23.8	114	290	22.7	111	320
Pulse Mode 6.0	68.7	110	479	68.8	113	480	66.8	109	613
Sleep Mode 2.0	28.9	109	582	22.2	110	449	38.2	109	764
Sleep Mode 6.0	85.7	108	613	66.5	103	479	112.5	104	793

2.2.4 Prediction of PF FiO2

The model used in this study to estimate PF F_iO_2 depends on the following parameters: the tidal volume $V_{T,}$ the ambient oxygen fraction $X_{O2,\ ambient}$, the volume of the airway replica $V_{replica}$, the total volume of the "lower conducting airways" V_{LA} (represented by the tubing connecting the airway replica to the lung simulator), the oxygen fraction of the pulse $X_{O2,\ pulse}$, and the volume of the pulse V_{pulse}.

Breathing was modeled with the assumption that exhaled gas in the anatomical dead space, consisting of upper and lower conducting airways at end-expiration, is immediately re-inhaled, and that none of the pulse remains in the anatomical dead space of the airways at the start of expiration. That is, pulse timing is assumed to be ideal, in that all oxygen delivered in the pulse reaches peripheral regions of the lungs (in the present experiments

represented by the lung simulator). Following re-inhalation of gas from the anatomical dead space, the remainder of the breath consists of the oxygen pulse and entrained ambient air. Over multiple breathing cycles, the gas mixture contained within the cylinder of the lung simulator will approach some steady state concentration, $X_{O2,\,c}$.

To derive the equation for $X_{O2,\,c}$, it was noted that in this steady state the volume of oxygen entering the lung simulator, $V_{O2,\,I}$, must be equal to the volume of oxygen that exits, $V_{O2,\,E}$. Therefore:

$$V_{O2,\ I} - V_{O2,\ E} = 0 \quad (1)$$

Based on the assumptions made above, this equation can be rewritten as:

$$V_{AW}X_{O2,c} + V_{pulse}X_{O2,pulse} + \left(V_T - V_{AW} - V_{pulse}\right)X_{O2,ambient} - V_T X_{O2,c} = 0 \quad (2)$$

where V_{AW}, the total volume of the airways (including the replica), is given by:

$$V_{AW} = V_{LA} + V_{replica} \quad (3)$$

Rearranging, one can solve for $X_{O2,\,c}$:

$$X_{O2,\ c} = X_{O2,ambient} + \frac{V_{pulse}}{V_T - V_{AW}}\left(X_{O2,pulse} - X_{O2,ambient}\right) \quad (4)$$

To find the FiO2 as measured and reported in the present experiments, one needs to take into account the volume of oxygen passing the trachea, rather than that reaching the lung simulator. Therefore, recently exhaled oxygen remaining in V_{LA} prior to the start of inspiration does not need to be accounted for. FiO2 can then be estimated by calculating the total volume of oxygen passing the trachea and dividing by V_T:

$$F_{IO2} = \frac{V_{pulse}X_{O2,pulse} + V_{replica}X_{O2,c} + (V_T - V_{replica} - V_{pulse})X_{O2,ambient}}{V_T} \quad (5)$$

FiO2 was calculated in this manner using each of the 15 different replica volumes and then averaged to give a single value. Averaged predicted values of FiO2, based on measured pulse characteristics, were then compared to average values measured using the realistic replicas and lung simulator.

2.2.5 Pressure drop measurements

In most POCs, breaths are detected using an internal pressure sensor that measures a reduction in pressure monitored at the oxygen supply tubing (the triggering pressure) corresponding to the start of inhalation. Pressure drops across each airway replica were measured at the cannula based on methods outlined in Moore et al [64]. An adult nasal cannula was inserted into the nostrils of each replica. The cannula was connected to a differential manometer (HHP-103, OMEGA Engineering, Norwalk, CT, USA) measuring the difference between cannula and atmospheric pressure. A vacuum was connected to each replica and a valve used to control inhalation flow rate, which was monitored using a mass flowmeter (TSI Mass Flowmeter 4043, TSI, Shoreview, MN, USA). Pressure drops were measured at flow rates of 10, 20, 30 and 40 L/min.

2.3 Results

2.3.1 Oxygen concentration and flow rate waveforms

Figure 2.3 shows oxygen concentrations and inspiration flow rates at the trachea for selected replicas plotted against time. As a matter of convention, positive flow rates indicate inspiration and negative flow rates indicate exhalation. Oxygen concentration

waveforms could be broadly classified as falling into one of three groups: waveforms indicating SF oxygen delivery, Figure 2.3a; waveforms indicating complete pulse delivery (the entire pulse reaches the internal cylinder of the lung simulator), Figure 3b; and waveforms indicating incomplete pulse delivery (a portion of the pulse remains in the anatomical dead space and is exhaled), Figure 2.3c.

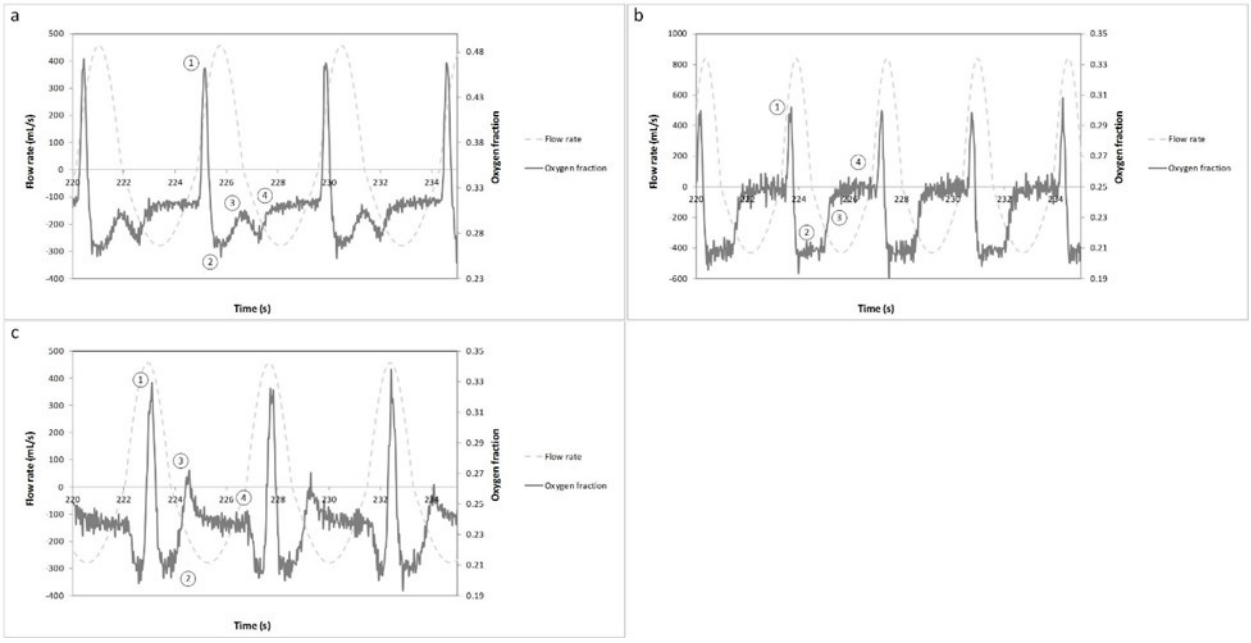

Figure 2.3. Example oxygen mole fraction and flow rate waveforms indicating (a) steady flow (SF) oxygen delivery, (b) complete pulse delivery and (c) incomplete pulse delivery. Waveforms in (a) and (c) were taken from experiment using Subject CT7; waveforms in (b) were from experiment using Subject CT9. Positive flow rates indicate inspiration; negative flow rates indicate expiration. Numbers indicate points of interest in the oxygen waveform (see Results section).

Continuous oxygen delivery waveforms (Figure 2.3a) were characterized by the presence of two peaks over the course of inspiration, one large, sharp peak occurring shortly after the

beginning of inspiration, and another smaller peak at the end. The variation in oxygen concentration over the course of inspiration for SF can be explained as follows:

1. The first, taller peak indicates pooling in the anatomic reservoir at the end of expiration. Since oxygen flow continues throughout the entire breath in SF, oxygen will accumulate in the upper airways as exhalation ends and the expiratory flow rate approaches zero. This pooled oxygen is then inhaled at the start of the next inspiration, which is reflected in the first sharp peak in oxygen concentration.
2. Once pooled oxygen is inhaled, the inspiration flow rate then increases toward a maximum, and therefore the fraction of inhaled gas represented by supplementary oxygen will decrease, which is reflected in a steep decrease in oxygen concentration. Conversely, as the inspiration flow rate passes its maximum and begins to decrease again, the supplementary oxygen fraction in the inhaled gas will increase.
3. As exhalation begins, gas remaining in the dead space (in this case, the tubing connecting the replica to the lung simulator) is immediately exhaled. Due to imperfect mixing in the airways, the dead space gas is exhaled on a first-in, last-out basis and will tend to lower the oxygen concentration. In other words, any comparatively low-oxygen gas (inhaled when the inspiration flow rate was high) remaining in the tubing will be further from the trachea than high-oxygen gas (inhaled when the inspiration flow rate was low).
4. Finally, as exhalation proceeds, the oxygen concentration approaches the constant oxygen concentration found in the internal chamber of the lung simulator.

On the other hand, oxygen concentration waveforms indicating complete pulse delivery (Figure 2.3b) can be identified by the presence of a single peak occurring near, but not coinciding with, the beginning of inspiration. Unlike the SF case, no pooling exists since oxygen delivery does not occur if no inspiratory effort is detected. The variation in oxygen concentration over the course of inspiration for complete pulse delivery can be explained as follows:

1. Here, the single peak at the start of inspiration indicates the passage of the pulse from the POC and through the trachea. The sharp initial decrease in oxygen concentration shortly following the start of inspiration is due to the delay between the start of the inspiratory effort and its detection by the POC, along with the transit time of the pulse through the upper airways.
2. Once the POC emits the pulse, no further supplementary oxygen is delivered. Oxygen concentration drops quickly to that of ambient air (approximately 21%) and remains there, indicating that the entire pulse likely reached the ASL chamber.
3. Expiration begins, and the gas (mostly ambient air) remaining in the dead space (the tubing connecting the replica to the ASL) is flushed out
4. Oxygen concentration then rises to that of the mixed gas inside the ASL chamber.

Incomplete delivery waveforms for PF (Figure 2.3c) proceed similarly to the complete case during the beginning of inspiration. However, in this case a second peak exists near the beginning of exhalation. For incomplete delivery, a portion of the pulse remains in the dead space tubing connecting the replica to the lung simulator, which is exhaled immediately, creating the second peak.

The number of replicas indicating incomplete pulse delivery as a fraction of the total is shown in Table 2.4.

Table 2.4. Number of breathing replicas indicating incomplete pulse delivery out of the total number of replicas used to calculate volume-averaged fraction of inspired oxygen (FiO2) at each setting/breathing pattern combination.

	Rest	Exercise	Sleep
Pulse Mode 2.0	0/15	0/15	2/12
Pulse Mode 6.0	1/15	2/15	3/11
Sleep Mode 2.0	n/a	n/a	5/14
Sleep Mode 6.0	n/a	n/a	5/14

2.3.2 SF and PF FiO2

Figure 2.4 and Figure 2.5 show comparisons of FiO2 between nominally equivalent PF settings (both Pulse and Sleep Mode for the sleep breathing pattern) and SF flow rates. For the sleep breathing pattern, three of the replicas failed to trigger the POC (i.e. no breathing was detected) at Pulse Mode setting 2.0, and four replicas failed to trigger the device at Pulse Mode setting 6.0. At Sleep Mode settings of 2.0 and 6.0, only one replica failed to trigger the device. FiO2 values measured for replicas and breathing patterns which failed to trigger the POC were excluded in calculation of the average values reported in Figures 2.3a and 2.3b.

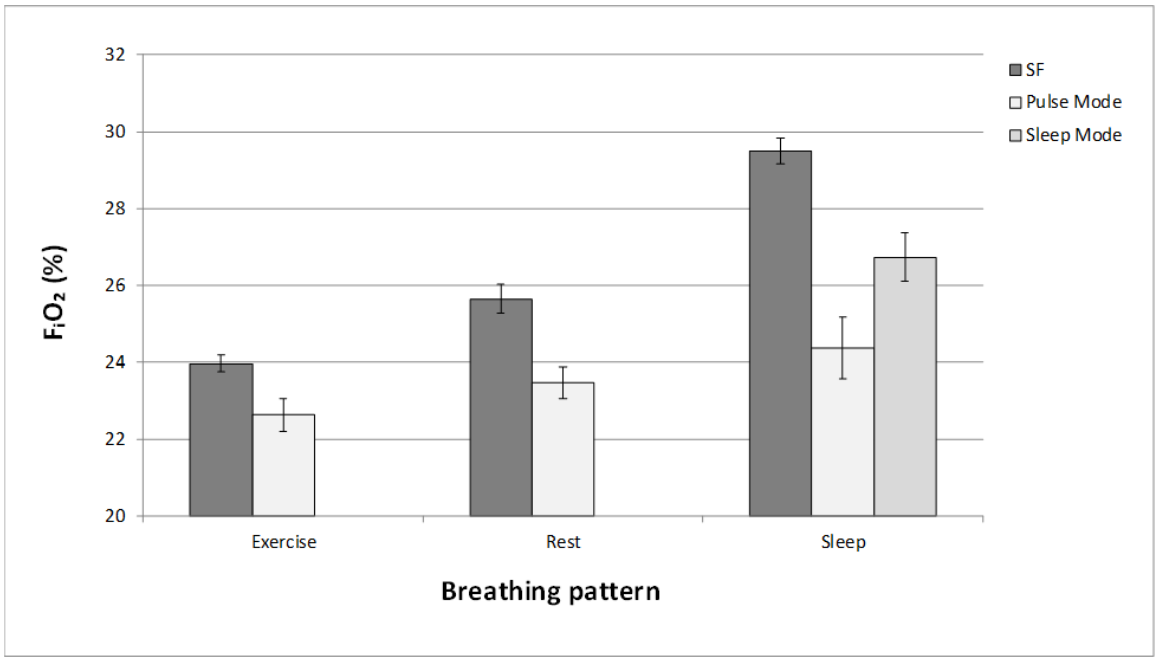

Figure 2.4. Comparison of volume-averaged FiO2 at SF 2.0 L/min and PF setting number 2.0, averaged over n different airway replicas, measured using 5 successive breaths per replica. For exercise and rest breathing patterns, n = 15. For the sleep breathing pattern combined with Pulse Mode, n = 12; with Sleep Mode, n = 14. Error bars indicate one standard deviation.

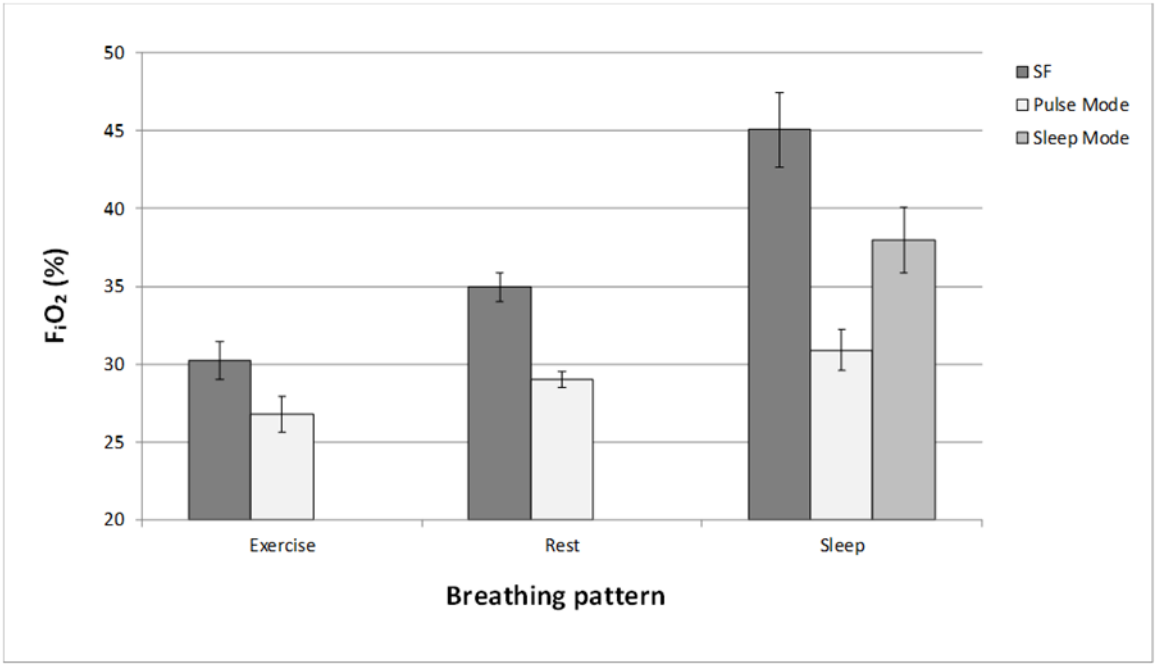

Figure 2.5. Comparison of volume-averaged FiO2 at SF 6.0 L/min and PF setting number 6.0, averaged over n different airway replicas, measured using 5 successive breaths per replica. For exercise and rest breathing patterns, n = 15. For the sleep breathing pattern combined with Pulse Mode, n = 11; with Sleep Mode, n = 14. Error bars indicate one standard deviation.

Mean PF FiO2 ranged from 68% to 94% of mean values obtained for nominally equivalent SF rates, generally decreasing with minute ventilation. Despite differences in airway volume and internal surface area, variability between replicas remained small compared to the mean (standard deviation < 5% relative to the mean).

2.3.3 Pressure drop measurements

Figure 2.6 shows the variation of pressure drop across the geometry measured from the cannula for each of the fifteen replicas with a steady inhalation flow rate. Differences

between replicas increased sharply with increasing flow rate. On the whole, most MRI replicas tended towards the low end of pressure drops.

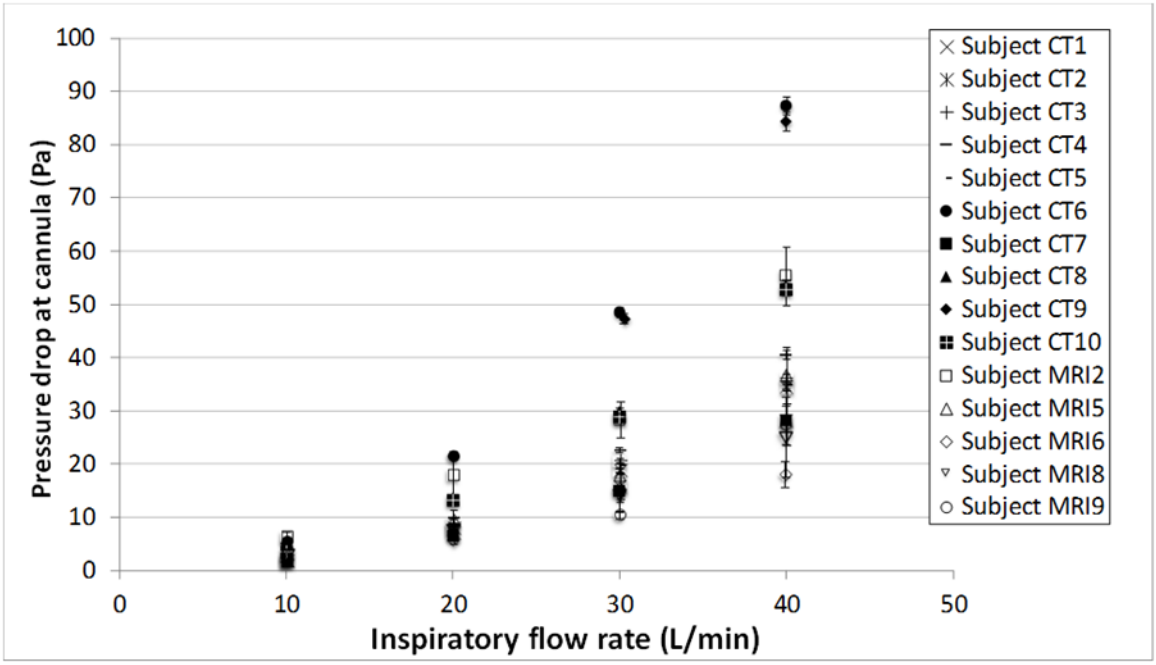

Figure 2.6. Pressure drop measured at the cannula as a function of inspiratory flow rate, averaged over 3 measurements. Error bars represent one standard deviation.

2.3.4 Predicting PF FiO2

PF FiO2 values estimated using Equation (5) and PF FiO2 values derived from airway replica experiments are plotted in Figure 2.7. Overall, Equation (5) consistently over-predicted average FiO2, but by a small margin. This margin increased as the setting number increased from 2.0 to 6.0 for both Pulse Mode and Sleep Mode, but no definite trend was observed as the breathing pattern was varied.

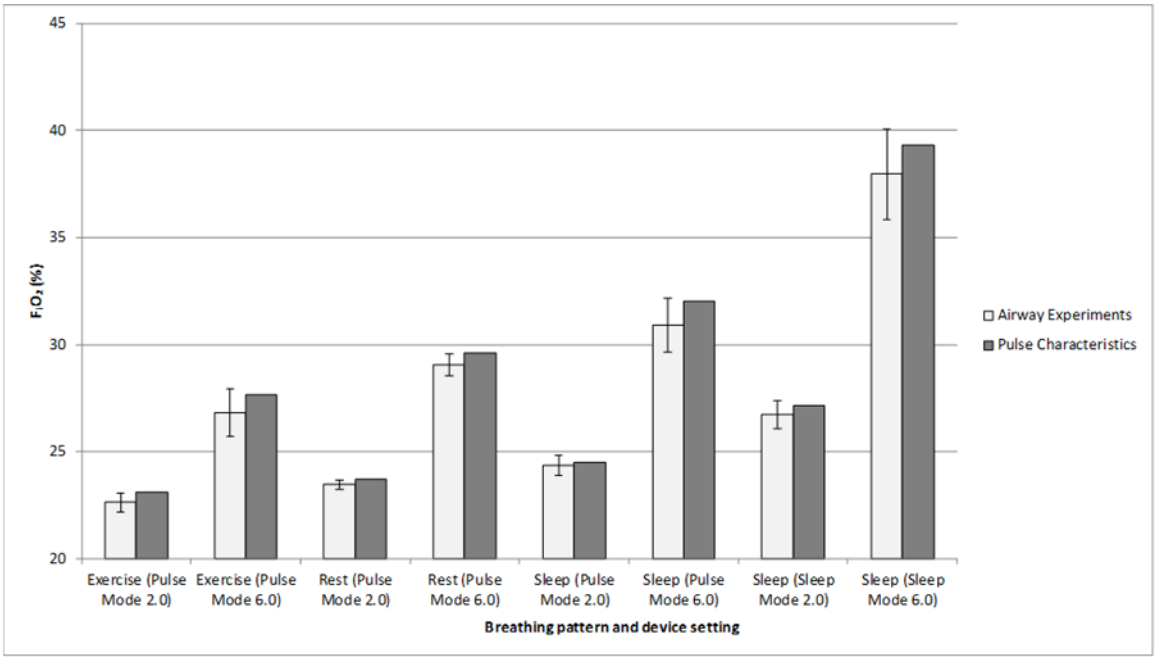

Figure 2.7. Comparison of volume-averaged FiO2 estimated from airway experiments and FiO2 predicted using pulse characteristics. Airway experiment FiO2 values were averaged over n airway replicas, measured using 5 successive breaths per replica. For all experiments with exercise and rest breathing patterns, n = 15. For the sleep breathing pattern combined with Pulse Mode setting number 2.0, n = 12; with Pulse Mode setting number 6.0, n = 11; with Sleep Mode setting numbers 2.0 and 6.0, n = 14. Error bars indicate one standard deviation.

2.4 Discussion

We developed an *in vitro* model that enabled us to measure real-time FiO2 values at the trachea while maintaining precise control of both breathing rate and tidal volume. This model was used to compare oxygen delivery between SF and PF delivery modes of a commercial POC under realistic triggering conditions, and to determine if oxygen pulse characteristics could adequately predict PF oxygen delivery.

2.4.1 Comparison with the in vivo *case*

Since FiO2 varies over the course of a breath during delivery of supplemental oxygen, it is challenging to accurately measure the amount of oxygen inhaled per breath *in vivo*. O'Reilly Nugent et al[30] monitored oxygen concentration at the trachea *in vivo* (sampled through a catheter) during oxygen delivery via nasal cannula for twenty adult subjects throughout inspiration, and calculated time-averaged FiO2 values. For subjects breathing at a rate of 15 breaths per minute receiving supplemental SF oxygen at a rate of 2.0 L/min, time-averaged tracheal FiO_2 ranged from 25 to 32%. When applying a similar time-averaging procedure to oxygen concentration data at similar settings (SF 2.0 L/min, 13 and 17 breaths per minute) obtained during *in vitro* experiments in the present study, we obtained a FiO2 range of 26 to 31%, which is in good agreement with the *in vivo* data.

On the other hand, the volume-averaged FiO2 reported in the present study is consistently 1 to 3% O_2 (absolute) lower than our own calculated time-averaged values. The volume-averaged values are considered here to be more pertinent to supplemental oxygen delivery compared to procedures that simply average by time, as high instantaneous inhaled oxygen concentrations may coincide with relatively low inspiratory flow rate near the start of the breath (and thus simple time-averaging procedures overweight the contribution of these transient peaks in concentration).

These considerations touch on what FiO2 actually represents. Waldau et al note that "the efficacy of oxygen therapy can be evaluated by a number of methods that reflect different steps in the oxygenation process depending on the sampling site [65]." In other words,

FiO2 has been considered as the concentration of inspired oxygen anywhere from a position within the patient interface to the alveoli (estimated based on measurements in the exhalation gas) [65,66]. It has been noted that measurements in the upper airways can be compromised by incomplete mixing of oxygen with inhaled air such that "gas can be sampled at a more distal point, preferably the trachea, where gas mixing is more assured [67]." Regarding estimates based on exhaled gas, homogeneous gas distribution in the lung must be assumed; an assumption that certainly does not apply for all patients. Thus, the bench model employed here where flow and concentration measured in the trachea are measured and integrated over the whole breath allows for a very robust approach that can account for variations in breathing parameters and delivery devices. Further accounting for myriad factors affecting alveolar gas concentrations and oxygen uptake, including gas transport and mixing through the airspaces of the lung and the diffusion capacity of the lung, may be best left to computational modeling [49]. *In vitro* measurement of tracheal oxygen concentrations over the breath, as presented here e.g. in Figure 2.3, would serve as valuable input to such computational models. In clinical practice, noting both the variability in oxygen delivery to the trachea measured in the present study with existing delivery systems, plus the additional intersubject and intrasubject variability that surely exists in oxygen transport and diffusion capacity, evaluation of oxygenation on an individual and ongoing basis, e.g. using pulse oximetry, is advisable.

2.4.2 Breath detection in POCs

Chatburn and Williams found that trigger pressures in 5 commercial POCs ranged from 14 to 22 Pa [53]. Since inspiratory flow rates in the sleep breathing pattern reach a maximum

of approximately 27 L/min, Figure 2.6 implies that at or below that flow rate, a commercial POC would be unlikely to detect the initiation of a breath in several of the replicas (< 10 Pa).

While the exact mechanisms of and conditions for breath detection in this specific POC are unknown, given that, in general, negative pressure sensors are frequently used for breath detection in POCs, we hypothesize that a low pressure drop at the nasal cannula may contribute to problems in POC breath detection.

2.4.3 Comparison of SF and PF delivery

PF FiO_2 values are consistently lower than those at equivalent SF rates. This difference increased with decreasing minute ventilation (i.e. with the sleep breathing pattern having the greatest difference). The higher pulse volumes delivered by Sleep Mode relative to Pulse Mode translated into relatively higher (but still not equivalent to SF) FiO_2 values, despite a higher prevalence of incomplete pulse delivery when using Sleep Mode. Our data show that, for the SimplyGo POC, the nominal PF setting and the SF flow rate are not equivalent when assessed using FiO_2.

The increased prevalence of incomplete pulse delivery in the sleep breathing pattern very likely contributes to the minute ventilation-PF/SF trend described above. As part of the oxygen bolus remains in the upper airways at the start of exhalation, FiO_2 will be lower as a result.

At first glance, one might expect that the increased breathing frequency of the high minute ventilation exercise breathing pattern would lead to more frequent incomplete pulse

deliveries (on account of shortened breathing times). While we did observe some cases of incomplete pulse delivery in the exercise case due to the above effect, these instances still remained more infrequent than in the sleep case. This may be due to two factors: (1) the time taken for an oxygen pulse to arrive at the trachea in sleep breathing patterns is the longest of all three patterns and (2) measured pulse durations were significantly longer for the sleep breathing pattern than they were for the other two patterns. While measurement of pulse characteristics using the O2 Conserver Test System confirmed factor (2), rigorous demonstration of factor (1), the influence of pulse arrival time, would require the ability to distinguish between oxygen in the emitted pulse from oxygen entrained from ambient air. This was not possible given our experimental setup. To qualitatively demonstrate the effect of pulse arrival time, we can consult Figures 2.2b and 2.2c. Sudden drops in oxygen concentration near the start of inspiration occur due to the temporary absence of supplemental oxygen. When concentration increases again, the pulse has arrived at the trachea. Therefore, in pulse delivery oxygen waveforms, the time it takes for the oxygen concentration to arrive at a temporary minimum after the start of inspiration indicates roughly how long it takes the pulse to arrive at the trachea. In Figure 2.3c (sleep breathing pattern), these times tend to be much longer than those in Figure 2.3b (rest breathing pattern). If one considers changes in inspiration flow rates between these two breathing patterns, this is to be expected. Because the ramp-up of inspiration flow rate slows down as minute ventilation decreases, the negative pressure trigger threshold is reached later in the course of inspiration. Pulse arrival times will also vary due to differences in individual

airway geometries, thus only some of the airway replicas tested resulted in incomplete pulse delivery.

The commercial O2 Conserver Test System is able to measure a pulse delay, representative of the time required for a pulse to arrive at the machine measured from when the machine attempts to trigger the POC. These pulse delays were constant across all breathing frequencies tested (110 ms); however, the ramp-up of flow rate is absent in the O_2 Conserver Test System testing protocol, thus these pulse delays are not equivalent to the pulse arrival times discussed above. Use of realistic airway replicas, as in the present experiments, therefore provides a test platform through which interaction between simulated breathing patterns and nasal airway geometry can be explored, and may be more representative of *in vivo* oxygen delivery via nasal cannula. Even so, the ability of the limited set of 15 realistic nose-throat airway replicas used herein to adequately capture variability in airway geometry in the much larger population of COPD patients receiving supplemental oxygen is unknown. Accordingly, variation between replicas in volume-average FiO2 (Figures 2.4 and 2.5), in triggering pressure measured at the cannula (Figure 2.6), and in complete versus incomplete pulse delivery (Table 2.4), should be interpreted as illustrative, rather than representative, of variability occurring in the larger population.

Another difference between SF and PF delivery is in the pooling effect of the anatomic reservoir during SF delivery. Zhou and Chatburn examined the effect of elimination of the anatomic reservoir on FiO2 in SF oxygen delivery [30]. They found that FiO2 was reduced in breathing in which the pooling effect of the anatomic reservoir was removed. In those

breathing waveforms, expiratory flow was not allowed to slowly decay to zero, which shortened the period of time in which expiratory flow was sufficiently low to permit supplemental oxygen to pool in the nasal airway. In the present study, the time needed for expiratory flow to reach zero is shorter in the exercise breathing pattern than in the rest or sleep breathing patterns, on account of an increased tidal volume and breathing rate. Therefore, one would expect the magnitude of the pooling effect to increase as the tidal volume and breathing rate decrease. The effect of the anatomic reservoir would be greatest for the sleep breathing pattern and smallest for the exercise breathing pattern. In contrast, because of the absence of end-expiratory oxygen flow, the anatomic reservoir has no effect on oxygen delivery in PF. As such, one would expect the discrepancy between SF and PF FiO_2 to grow as tidal volume decreases and breathing slows down, as observed in Figures 2.3 and 2.4.

2.4.4 Predicting PF FiO_2 based on pulse characteristics

PF FiO_2 estimated using real-time oxygen concentrations and PF FiO_2 calculated by way of Equation (5) using pulse characteristics were generally in agreement. However, since absolute differences in FiO_2 of 1% may be clinically significant in long term therapy, we can conclude that while usage of pulse characteristics alone is sufficient to predict oxygen delivery for many conditions, testing using realistic airway replicas is still useful in some cases where calculation using pulse characteristics might significantly over-predict POC performance (e.g. sleeping patients at high setting numbers).

2.4.5 Study limitations

Although the present testing methodology can be seen as an improvement on past attempts to precisely quantify the amount of oxygen inspired during supplemental oxygen therapy, several limitations can be noted. First, the results presented above are specific to a single POC, and therefore do not reflect performance of POCs in general. Expanded testing, using the present methodology, may provide valuable information describing the relative oxygen delivery from different POCs operating at nominally equivalent pulse settings.

In addition, medical images upon which the airway replicas are based were acquired in awake subjects during tidal breathing. Therefore, they do not encompass any changes to upper airway geometry that may occur during sleep or at high minute ventilation during exercise.

Further, the lack of oxygen uptake in the test lung places a limit on our ability to accurately predict FiO_2 in a clinical, rather than benchtop, setting. Because breathing involves re-inhalation of gas from the conducting airways, the concentration of oxygen exhaled from gas-exchange regions of the lungs, and subsequent re-inhaled, is relevant in determining FiO_2. As there is no analogue present for alveolar oxygen uptake in the lung simulator used in this study, any amount of supplementary oxygen supplied will, over time, increases the inner chamber oxygen concentration (analogous to the alveolar oxygen concentration). In the *in vivo* case, oxygen is constantly being removed through the alveoli into the blood, thus decreasing the oxygen concentration of the exhaled gas. To demonstrate this effect, we

can consider what happens when Equation (1) is modified to include a non-zero term for oxygen uptake into the blood.

$$V_{AW}X_{O2,c} + V_{pulse}X_{O2,pulse} + \left(V_T - V_{AW} - V_{pulse}\right)X_{O2,ambient} - (V_T X_{O2,c} + V_{O2,uptake}) = 0 \qquad (6)$$

$V_{O2,uptake}$ represents a volume of oxygen that is drawn into the blood in a single breath. Rearranging Equation (6), we can obtain modified version of Equation (4).

$$X_{O2,c} = X_{O2,ambient} + \frac{V_{pulse}}{V_T - V_{AW}}\left(X_{O2,pulse} - X_{O2,ambient}\right) - \frac{V_{O2,uptake}}{V_T - V_{AW}} \qquad (7)$$

Since all values in the final term on the right hand side of Equation (7) are greater than zero, $X_{O2,c}$ calculated using Equation (7) will always be lower than $X_{O2,c}$ calculated using Equation (4).

Incomplete pulse delivery also has implications on oxygen delivery to the lungs beyond what is observed in its effect on FiO2 evaluated at the trachea. In cases of incomplete pulse delivery, less of the pulse is able to travel past the trachea and into the lungs. However, our reported FiO2 values do not account for a portion of the oxygen pulse that is immediately exhaled from the dead space of the tracheo-bronchial airways. When assessing oxygen delivery to the gas-exchange regions of the lungs, modeling the transport of oxygen from the trachea through a multi-generation airway tree may provide a more complete picture [49].

Additional future work may also involve comparisons of oxygen delivery in closed versus open mouth breathing, in children versus adults, or in diseased versus healthy lungs. The

effect of mouth-breathing versus nose-breathing, or open versus closed mouth position[31], is especially relevant during sleep and exercise.

2.5 Conclusions

This study examined a benchtop testing method for assessing POC performance using realistic airway models and real-time monitoring of inspired oxygen concentrations at the trachea. Testing using nasal airway replicas derived from medical imaging and simulated breathing patterns permitted oxygen delivery from a POC to be evaluated under realistic triggering conditions.

Based on measurement of volume-averaged tracheal FiO_2 for the POC studied, PF delivered consistently lower amounts of oxygen than SF at flow rates equivalent to nominal PF settings. Differences were largest when the higher PF setting was combined with breathing parameters typical of sleeping patients. We hypothesize that this difference is primarily due to two factors: (1) the increased effect of oxygen pooling for SF in the anatomic reservoir during slower, shallower breathing, and (2) a delay in the arrival of the pulse, which leads to retention in the upper airways and exhalation of part of the oxygen bolus.

Chapter 3: In Vitro-In Silico Comparison of Pulsed Oxygen Delivery from Portable Oxygen Concentrators versus Continuous Flow Oxygen Delivery

3.1 Introduction

Long term oxygen therapy has been shown to prolong life in patients with chronic obstructive pulmonary disease (COPD) and severe daytime hypoxemia [68,69]. Oxygen has historically been provided as a continuous, steady flow supplied to the patient interface, but more recently, intermittent delivery methods triggered by a patient's breathing have been developed as portable or cost saving alternatives [5–7].

Portable oxygen concentrators (POCs) are the latest class of devices in the intermittent delivery paradigm [5,67]. As these devices concentrate existing atmospheric oxygen, they do not require a stationary oxygen source and provide a portable option for supplemental oxygen therapy. Although some POCs can deliver oxygen continuously at limited flows, many recent-generation devices deliver oxygen exclusively using pulse flow (PF), in which a short-duration flow, or pulse, of oxygen is provided only when patient inspiration is detected [48]. A recent study showed that chronic obstructive pulmonary disease (COPD) patients requiring long term oxygen therapy generally prefer a single source POC over a combined stationary and portable oxygen source, citing the practicality of the system as its main advantage [47]. However, the same study showed that insufficient oxygenation (SpO2 < 90%) was more frequent among single source POC users.

The challenge of establishing equivalence between continuous flow oxygen (CFO) and nominal PF device settings on different devices is well known5,9 and provides motivation

for the development of physiologically representative in vitro testing methods [7,11]. Chen et al 10 recently outlined a methodology to compare PF oxygen delivery from a commercially available POC with CFO delivery from a stationary cylinder using a set of 15 realistic airway replicas [71]. Using these replicas together with a lung simulator in in vitro experiments allowed for precise control of simulated breathing parameters in anatomically representative models of the upper airways, and made it possible to account for potential inter-subject variability due to variance in airway geometries, as well as allowing modes of failure to be assessed when a POC failed to detect an inspiratory effort. By measuring the real-time oxygen concentration at the airway replica outlet (representative of the trachea) during inspiration, a volume-averaged FiO2 was obtained that represented the fraction of oxygen contained in a given inhaled tidal volume [71].In other words, these volume-averaged FiO2 values represent the ratio between the total volume of inhaled oxygen (including both supplemental oxygen and oxygen in the entrained air) and the inhaled tidal volume, and provide a common basis for comparison between PF and CFO [71].

Building on this recent work, the present study had two primary objectives. The first was to compare the performance of several POCs against each other and against CFO, using volume-averaged FiO2 at the trachea as a measure of oxygen delivery. The second objective was to characterize the transport of oxygen pulses from the trachea through the conducting airways via mathematical modelling. This enabled the assessment of the impact of CFO flows, PF settings and breathing parameters on transport of oxygen through the conducting airways to the gas-exchange region of the lung.

3.2 Methodology

3.2.2 Selection of a representative airway replica

In Chen et al. (2017), testing was limited to a single POC evaluated at two integer pulse settings, one high (6.0) and one low (2.0). It was found that intersubject variability between 15 airway geometries had only a small (less than 5% coefficient of variation) impact on volume-averaged FiO2 values [71]. Therefore, it was deemed reasonable to use only a single representative replica for comparative testing in the present work. A single replica was selected on the criterion that the volume-averaged FiO2 value obtained using this replica (for either CFO or PF) was closest to the average value obtained across the set of 15 replicas. Figure 3.1 compares volume-averaged FiO2 values obtained for the selected airway replica (Subject MRI2) with average and standard variation of values obtained across all replicas.

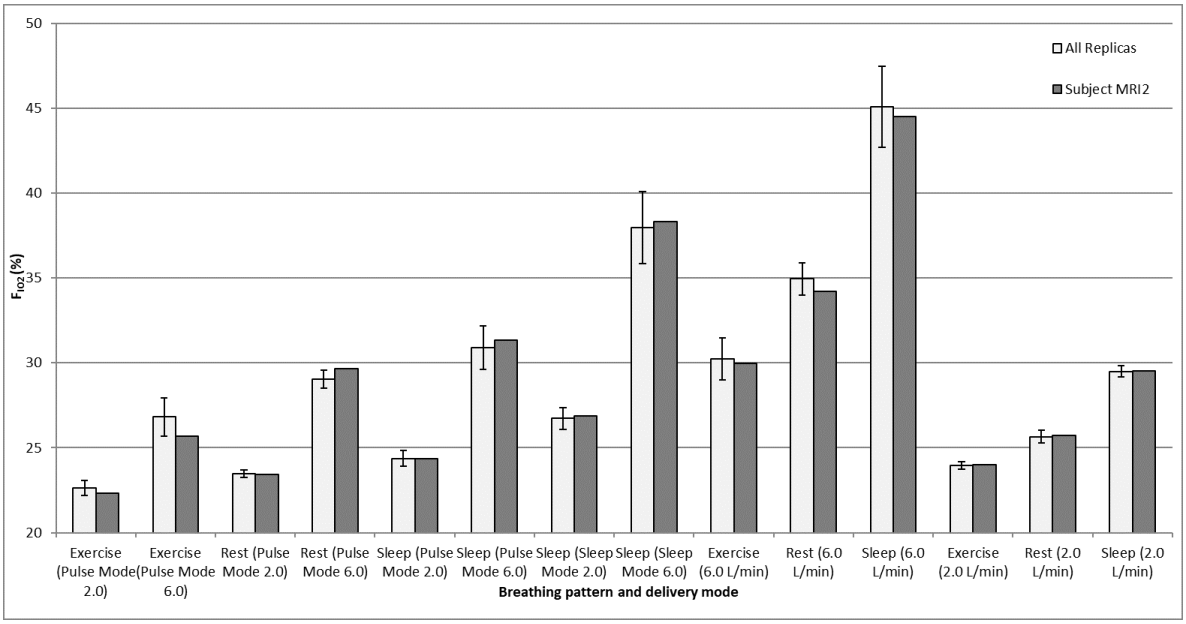

Figure 3.1. Comparison of volume-averaged FiO2 using Subject MRI2 with mean volume-averaged FiO2 across 15 airway replicas. Data for both pulse deliveries from a Philips SimplyGo portable oxygen concentrator and continuous flow oxygen from a stationary source of compressed oxygen are included. Error bars indicate one standard deviation.

The selected replica had a total interior volume of 44.6 mL and an interior surface area of 287 cm^2. These values were obtained using MeshLab (Visual Computing Laboratory, Istituto di Scienza e Tecnologie dell'Informazione, Italy) and ParaView (Kitware, Clifton Park, NY, USA).

3.2.3 Airway experiments

Experiments were performed using the experimental apparatus described in Chen et al [71]. The test set of POCs consisted of a Philips SimplyGo (Philips Respironics, Murrysville, PA, USA), a Philips SimplyGo Mini, an Inogen One G3 (Inogen, Goleta, CA, USA) and an Inogen One G4. Figure 3.2 shows a photograph of the tested POCs, the weight of each device and a visual comparison of device size. Specifications for each device are shown in Table 3.1. To account for the variety of use conditions a COPD patient may experience in their everyday life, and to explore the effect of varying breathing frequency and tidal volume on POC performance and FiO2, three different breathing patterns were chosen: representative of a COPD patient at rest, while asleep and during light exercise. The inspiration and expiration flow waveforms were each modeled using a half-sinusoid and actuated using a lung simulator (ASL 5000 Breathing Simulator; IngMar Medical, Pittsburgh, PA). Figure 3.3 shows a schematic of the experimental apparatus. Breathing parameters for each of these patterns (at rest, while asleep and during light exercise) are

provided in Table 3.2. The rest and exercise breathing parameters were chosen based on average values reported previously by Chatila et al for 10 patients with COPD at baseline (rest) and while on CFO (2.5-6 L/min) while performing light exercise on a cycle ergometer [62]. Parameters for the sleep breathing pattern were chosen based on average values measured by Hudgel et al for 13 COPD patients while asleep [63].

Table 3.1. Specifications for portable oxygen concentrators used in this study.

Device	Vendor	Weight (lbs)	Settings (arbitrary units)
SimplyGo	Philips	10.0	Pulse: 1 – 6 Continuous: 0.5 – 2 L/min
SimplyGo Mini	Philips	5.0	Pulse: 1 – 5
One G3	Inogen	4.8	Pulse: 1 – 5
One G4	Inogen	2.8	Pulse: 1 – 3

Table 3.2. Breathing parameters of representative breathing profiles for COPD patients at rest, doing light exercise and while asleep.

	Rest	Exercise	Sleep
Tidal volume, V_T (mL)	640	800	520
Inspiratory time, T_I (s)	1.20	0.96	1.79
Expiratory time, T_E (s)	2.33	1.77	2.93
Breathing frequency, f (breaths min^{-1})	17	22	13

Figure 3.2. Photograph of commercial portable oxygen concentrators tested in this study manufactured by Phillips Respironics and Inogen.

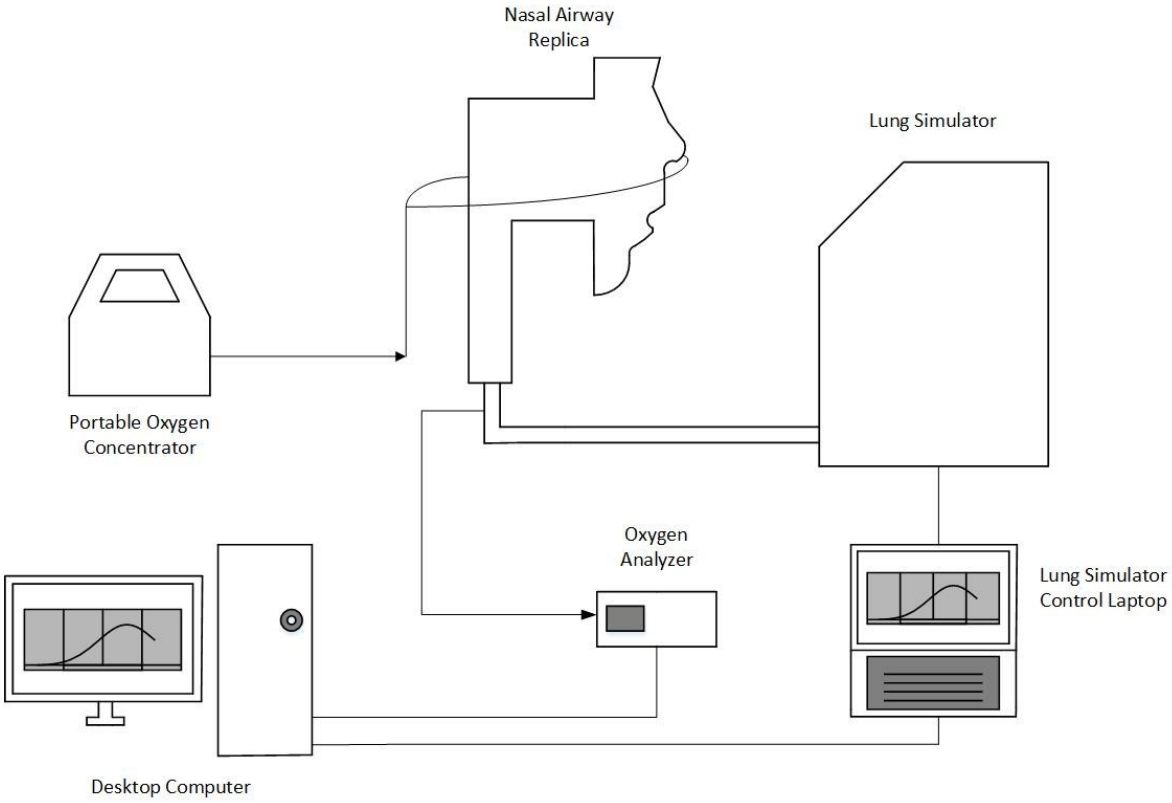

Figure 3.3. Schematic of apparatus used in experiments involving airway replicas. Arrows indicate direction of oxygen flow.

3.2.4 Calculation of volume-averaged tracheal FiO2

Figure 3.4 shows example flow and oxygen fraction waveforms. The flow of oxygen passing through the trachea over time was calculated by multiplying inspiration flow with measured oxygen concentrations at the same point in time. The beginning and end of inspiration were identified as times when oxygen flow crossed 0 mL/s. These oxygen flows were then numerically integrated via the trapezoidal rule from the start to the end of inspiration to determine a volume of oxygen inspired for that breath. Finally, volume-averaged FiO2 was obtained by dividing the inspired volume of oxygen by V_T. FiO2 for

each combination of device, device setting and breathing pattern was taken as the average of five consecutive breaths after a steady state in the end-expiratory oxygen concentration was observed. Variability between FiO2 values obtained in experiments repeated on separate days was found in preliminary testing to be of similar magnitude as variability between individual breaths.

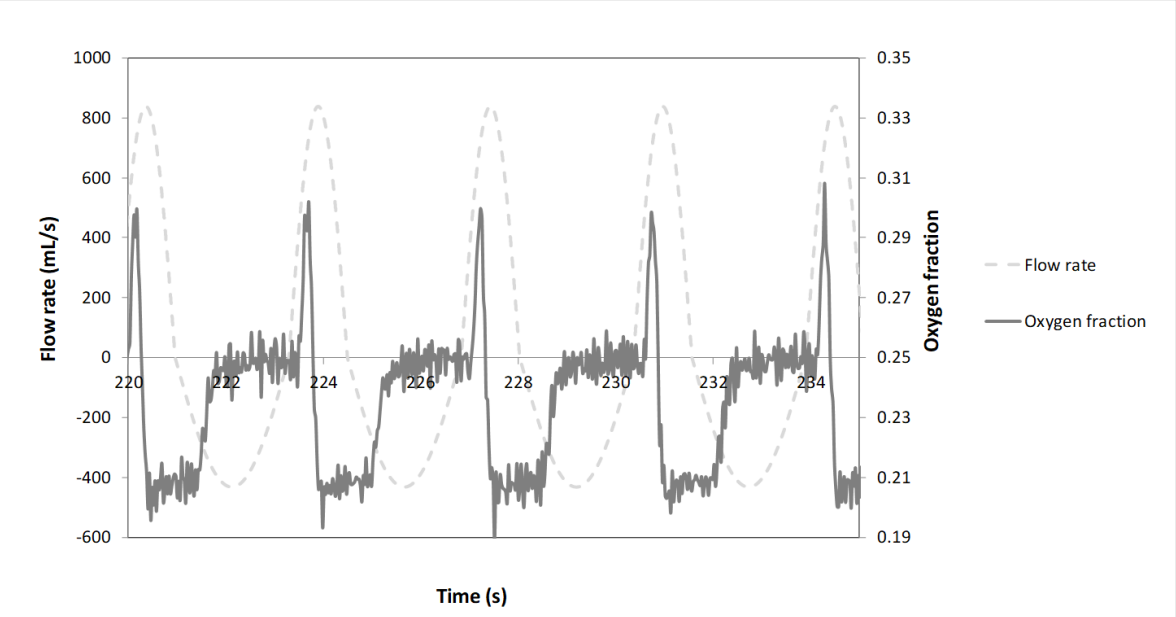

Figure 3.4. Sample flow and oxygen fraction waveforms generated by the experimental apparatus for pulsed delivery of oxygen.

One-way analysis of variance was performed to compare differences in volume-averaged tracheal FiO2 by analyzing the simple main effects of device setting/CFO flow and mode of delivery (four POCs and CFO). Multiple post-hoc comparisons were then done using the Tukey test, with $P < 0.05$ considered significant.

3.2.5 Measurement of pulse characteristics

An O_2 Conserver Testing System (1130 series; Hans Rudolph Inc., Shawnee, KS, USA) was used to obtain oxygen pulse volumes, durations and delays for each setting and each POC. POCs were connected to the testing system using standard oxygen tubing. Data was recorded as the average of twenty successive pulses for each breathing pattern/setting combination.

Anecdotally, it was noted that both the Inogen devices would occasionally skip, or fail to trigger during an inspiratory effort. This may be consistent with the manufacturer's description in the manual that the device may "ignore one of the breaths, giving the appearance of a missed breath," as Inogen devices monitor and occasionally re-evaluate their delivery regime based on the user's breathing pattern. Average pulse characteristics were calculated only from breaths where the device was triggered.

3.2.6 Prediction of PF volume-averaged FiO2

Chen et al. previously published an algebraic model predicting *in vitro* volume-averaged FiO2 in realistic airway replicas based on pulse characteristics [71]. The model uses airway replica internal volume, measured pulse volumes, ambient oxygen concentration, and pulse oxygen concentration to first calculate an internal oxygen concentration in the chamber of the test lung, or equivalently, the amount of oxygen passing the entrance to the chamber of the test lung:

$$X_{O2,c} = X_{O2,ambient} + V_{pulse}(X_{O2,pulse} - X_{O2,ambient})/(V_T - V_{AW}) \quad (1)$$

where $X_{O2,\,C}$ is the test lung chamber oxygen fraction, $X_{O2,\,ambient}$ is the fraction of oxygen in ambient air, V_{pulse} is the volume of the oxygen pulse, V_T is the tidal volume, V_{AW} is the total volume of the airways (both upper and lower respiratory tracts) and $X_{O2,\,pulse}$ is the oxygen fraction (0.94 for the Philips devices, 0.95 for the Inogen devices) of the pulse.

In vitro volume-averaged FiO2 is then predicted using the following equation:

$$FiO2 = (V_{pulse}\, X_{O2,pulse} + V_{replica} X_{O2,c} + (V_T - V_{replica} - V_{pulse})\, X_{O2,ambient})/V_T \quad (2)$$

3.2.7 Mathematical modelling of oxygen transport through the conducting airways

Oxygen flowing past the trachea enters the conducting airways and may eventually be transported to alveolated regions of the lung where gas-exchange occurs. To describe the transport of the oxygen pulse through the conducting airways to the acini, a modified version of a mathematical model previously described by Martin et al. for assessing nitric oxide (NO) transport and uptake was utilized [72]. The model, written in MATLAB (Mathworks, Natick, MA, USA), assumes a simplified single-path, single-alveolar compartment lung structure with no oxygen exchange occurring in the conducting airways.

Using oxygen concentration waveforms measured at the trachea over time from the *in vitro* measurements described above as a boundary condition, the present model simulated the transport of oxygen to the acini by a combination of bulk convection and axial dispersion through the conducting, tracheobronchial airways, which were modelled as a series of branching tubes whose dimensions become smaller with each branching generation. The mathematical model assumed these tubes to be rigid, cylindrical and bifurcating between

each airway generation. Baseline dimensions were taken from an adult airway model provided by Finlay et al., that is based on airway data from Phillips et al for an adult with a functional residual capacity (FRC) of 3000 mL (Table 3.3) [56,73]. Additional details pertaining to the mathematical model are described in Appendix A.

Generation number	Diameter (cm)	Length (cm)
0	1.96	13.53
1	1.53	3.92
2	1.22	3.11
3	0.97	2.48
4	0.77	1.93
5	0.62	1.23
6	0.49	0.98
7	0.39	0.90
8	0.32	0.81
9	0.24	0.71
10	0.17	0.61
11	0.13	0.49
12	0.10	0.39
13	0.08	0.30
14	0.07	0.24

Table 3.3. Cylindrical airway dimensions of tracheobronchial airways at each generation in lung model.

Inputs to the model consisted of:

1) Comma-separated value (.csv) versions of individual oxygen concentration waveforms over the course of inhalation (one per breathing pattern/device setting combination), which were extracted manually from raw oxygen concentration data.

2) Simulation breathing parameters, including tidal volume, breathing frequency and i:e ratio (ratio of inhalation to exhalation time). Values of I:E were 0.515 for the exercise breathing pattern, 0.538 for the rest breathing pattern and 0.613 for the sleep breathing pattern. These were used to generate the same idealized breathing patterns as those used in the *in vitro* experiments.
3) Pre-inhalation oxygen concentration in the conducting airways. As the present analysis considered only the transport of oxygen through conducting airways during a single inhalation, and not uptake of oxygen to the blood, the oxygen concentration throughout the conducting airways was set to zero at the beginning of each simulation. Under this condition, only the transport of oxygen freshly-inhaled through the upper airway was considered.

Outputs of the model included time-varying oxygen concentrations at individual airway generations distal to the trachea, total volume of oxygen delivered to the acini and the ratio between the oxygen volume delivered to the acini and that delivered to the trachea, which represents acinar delivery efficiency. Because the initial concentration of oxygen in the conducting airways was set to zero at the start of inhalation, the acinar delivery efficiency can be viewed as the fraction of oxygen passing the trachea that also passes into the acini during an inhalation.

Based on preliminary simulations, the coefficient of variation in delivered oxygen volume between simulations performed for different individual breaths ranged from approximately

0.1% to 4% of the mean. It was therefore sufficient to use only a single breath from each breathing pattern/device/pulse setting combination in the model calculations.

3.3 Results

3.3.1 Comparisons of POC performance

Figure 3.5 shows the comparisons of volume-averaged FiO2, pulse volume, and pulse duration for CFO from a compressed oxygen source versus PF from each of the POCs. Figure 3.6 illustrates the differences between each device by showing pulse flow profiles over time at pulse setting 2 for each of the POCs.

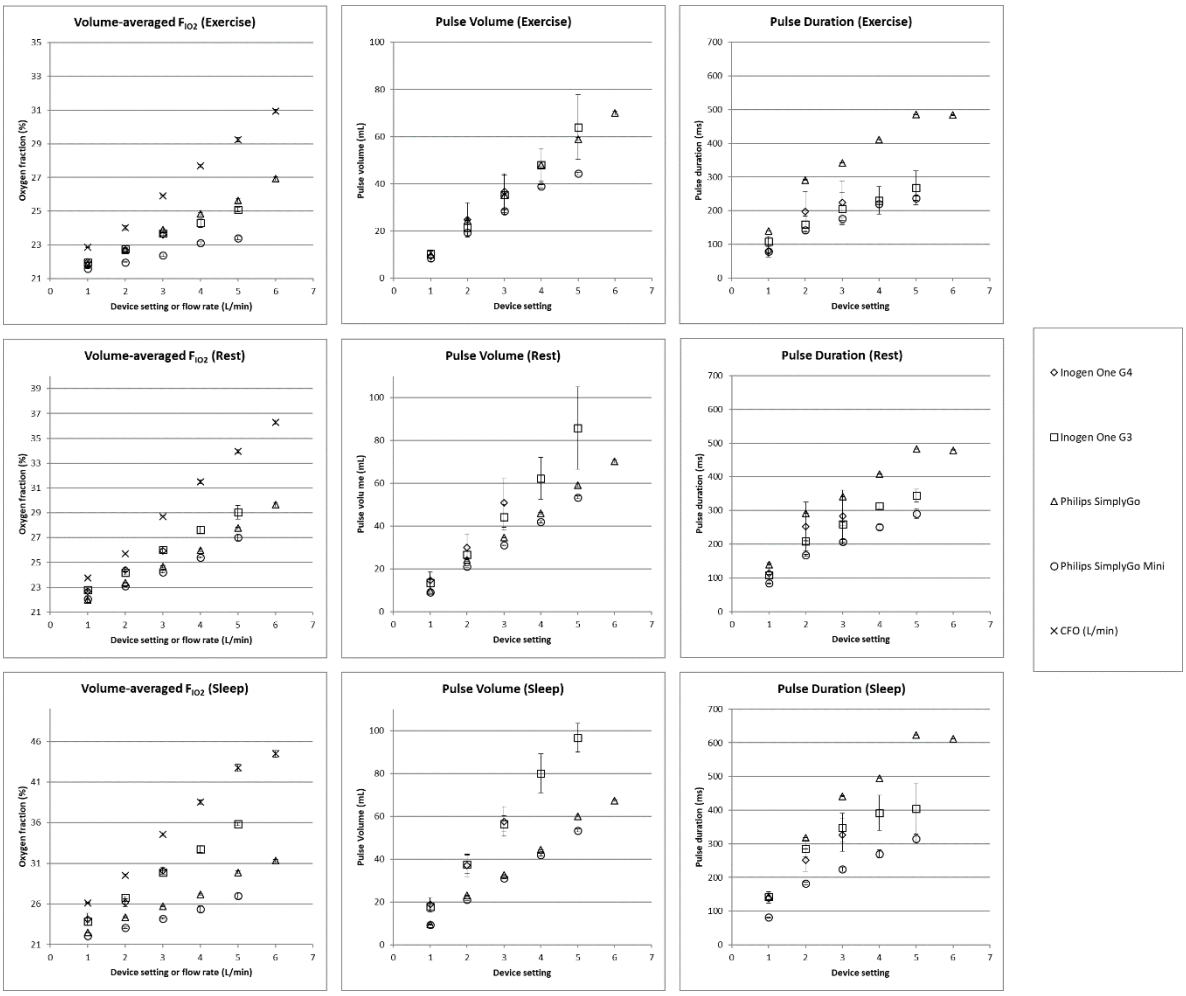

Figure 3.5. Volume-averaged FiO2 and pulse characteristics for each of the tested portable oxygen concentrators and continuous flow oxygen across three breathing patterns. FiO2 values were averaged over 5 consecutive breaths. Other pulse characteristics averaged over 20 consecutive breaths. Error bars indicate one standard deviation.

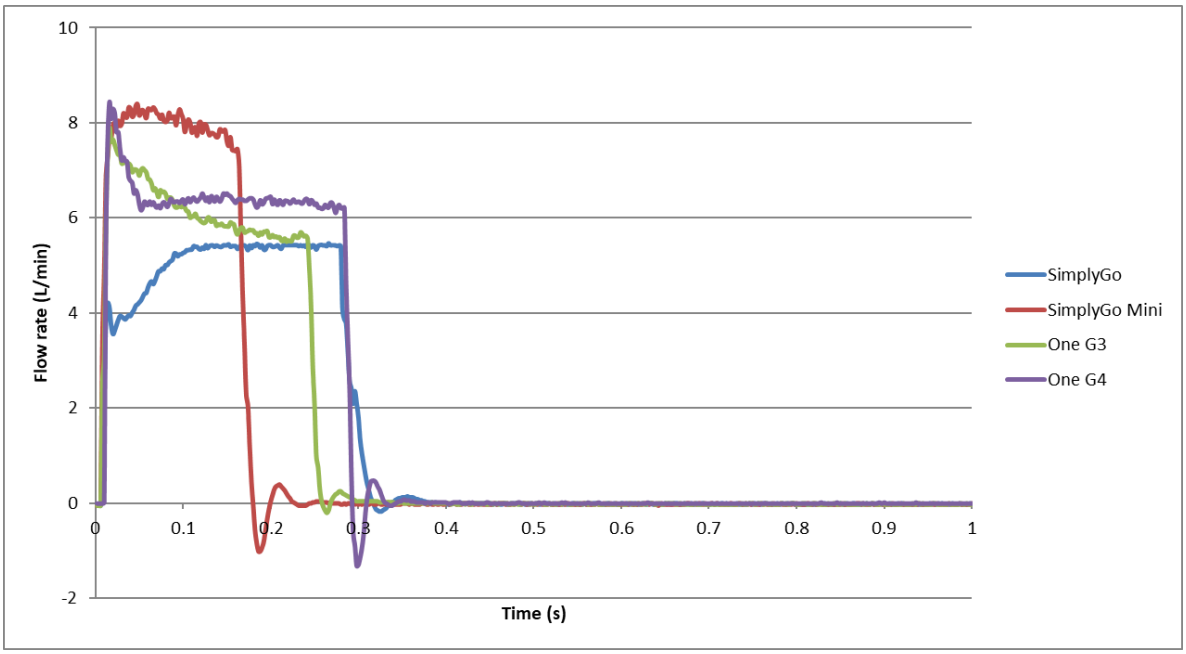

Figure 3.6. Pulse flow curves generated by the O2 Conserver Testing System for each POC at setting 2 for each device and breathing frequency of 17 breaths per minute.

Statistical analysis showed that, when the mode of delivery was held constant, there were statistically significant differences between all device settings/CFO flows for each mode of delivery and breathing pattern. With device setting/CFO flow held constant, several homogeneous subgroups (groups of delivery modes with statistically similar performance) emerged under post-hoc analysis, which are listed in Table 3.4.

	Device setting (no units) or CFO flow (L/min)					
Breathing Pattern	1.0	2.0	3.0	4.0	5.0	6.0
Exercise	CFO	CFO	CFO	CFO	CFO	CFO
	SimplyGo One G3 One G4	SimplyGo One G3 One G4	SimplyGo	SimplyGo	SimplyGo	SimplyGo
			One G3 One G4	One G3	One G3	
	SimplyGo Mini	SimplyGo Mini	SimplyGo Mini	SimplyGo Mini	SimplyGo Mini	
Rest	CFO	CFO	CFO	CFO	CFO	CFO
	One G3 One G4	One G4	One G3 One G4	One G3	One G3	SimplyGo
		One G3		SimplyGo	SimplyGo	
	SimplyGo SimplyGo Mini	SimplyGo	SimplyGo			
		SimplyGo Mini	SimplyGo Mini	SimplyGo Mini	SimplyGo Mini	
Sleep	CFO	CFO	CFO	CFO	CFO	CFO
	One G3 One G4	One G4	One G3 One G4	One G3	One G3	SimplyGo
		One G3			SimplyGo	
	SimplyGo SimplyGo Mini	SimplyGo SimplyGo Mini	SimplyGo SimplyGo Mini	SimplyGo SimplyGo Mini	SimplyGo Mini	

Table 3.4. Subgroups with statistically similar volume-averaged tracheal FiO2 ($P > 0.05$) segregated by device setting/CFO flow and breathing pattern. For each breathing pattern, subgroups are separated with a line and have significant differences ($P < 0.05$) in volume-averaged FIO2 with other subgroups. Additionally, for each breathing pattern subgroups are arranged by magnitude of FiO2, in descending order, top to bottom. The One G4 does not feature device settings above 3.0, and only the SimplyGo features pulse settings up to 6.0.

Due to the high repeatability of the *in vitro* test methods employed, in some cases very small differences in FiO2 were statistically significant. Therefore, in addition to statistical significance, a threshold for a practical or anticipated clinically significant difference in FiO2 was defined to be > 2% (absolute percentage oxygen) following Zhou and Chatburn

[30]. Using this more demanding threshold, CFO still delivered a significantly higher FiO2 than PF in at least one of the devices at all nominally equivalent device settings of 2 and greater. The magnitude of this difference decreased as breathing minute volume (which is here an increase in both tidal volume and breathing frequency) increased.

For the two Philips devices, the SimplyGo consistently delivered more oxygen than the SimplyGo Mini, although FiO2 values were within 2% (absolute) for the majority of breathing pattern/setting number combinations, with the exception of setting 5 in the sleep and exercise breathing patterns. For the Inogen devices, no anticipated clinically significant FiO2 difference was observed between devices when operating at the same device setting for any of the three breathing patterns. While the Inogen devices delivered similar FiO2 as the SimplyGo for the exercise breathing pattern, FiO2 was greater for the Inogen devices than for the SimplyGo devices for the rest and sleep breathing patterns.

3.3.2 Prediction of volume-averaged tracheal FiO2 using measured pulse characteristics

At a given nominal device setting, different POCs provided different oxygen volumes per breath (Figure 3.5). For a given POC, pulse volume increased approximately linearly with device setting number across each breathing pattern. In general, increasing pulse volumes were correlated with increasing values of volume-averaged FiO2.

The longest pulse durations were observed in the SimplyGo while the shortest were observed in the SimplyGo Mini (Figure 3.5). At the breathing frequencies considered (13 to 22 bpm), pulse durations correlated positively with setting number, but correlated negatively with breathing frequency. Figure 3.7 shows a comparison of volume-averaged

tracheal FiO2 derived from airway experiments with those calculated from pulse characteristics using Equation (2). For the sleep breathing pattern, there were no anticipated clinically significant differences between the two sets of FiO2 predictions (i.e. absolute difference of <2%) for any of the device settings in any of the devices. For the rest and exercise cases, only setting 5 of the One G3 resulted in a significant difference between the airway experiment FiO2 and pulse characteristics-derived FiO2. More generally, increasing the minute volume resulted in a higher absolute difference between the two FiO2 sets, although most of these differences did not meet the threshold for anticipated clinical significance.

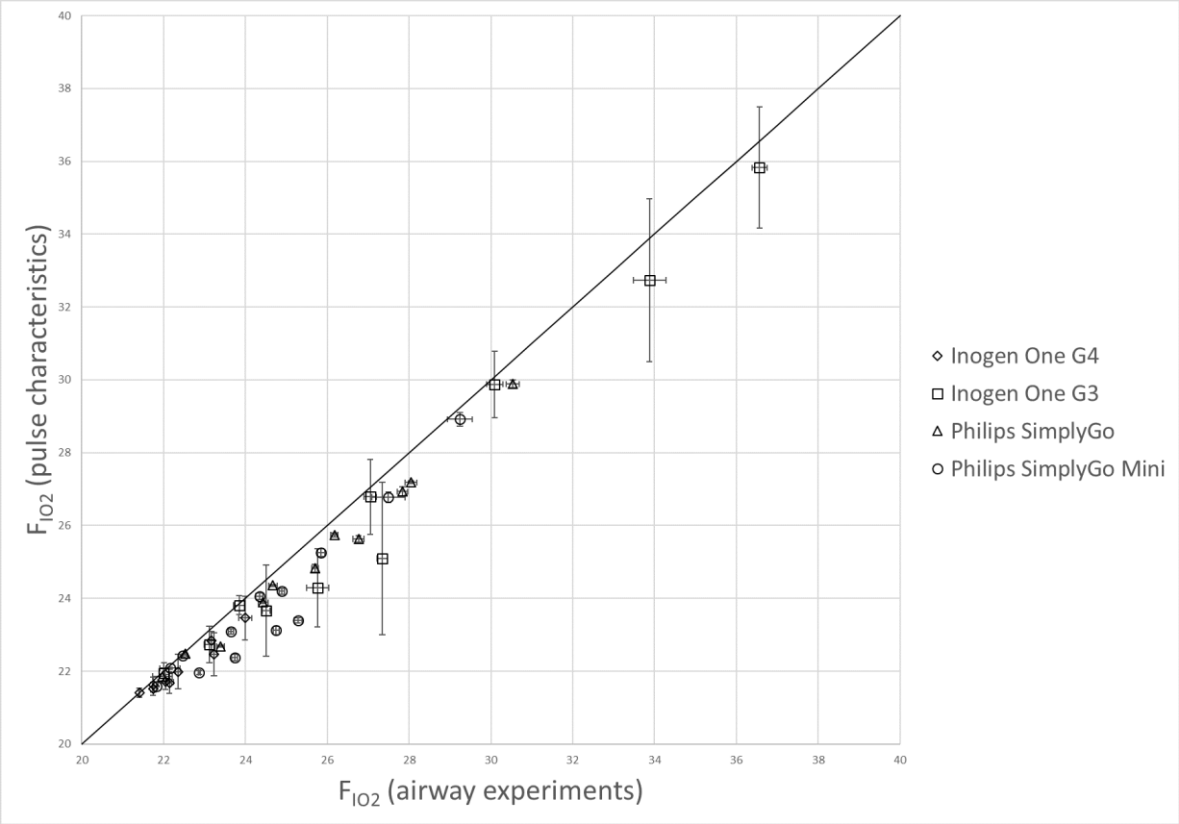

Figure 3.7. Comparisons of volume-averaged FiO2 measured in airway experiments with volume-averaged FiO2 predicted using pulse characteristics. Vertical error bars indicate one standard deviation of FiO2 determined from airway experiments over five consecutive breaths. Horizontal error bars indicate one standard deviation of FiO2 determined using pulse characteristics over twenty consecutive breaths. Identity line shown for comparison.

3.3.3 Mathematical modelling

Figure 3.8 shows a sample output of the mathematical model for oxygen transport in the lower airways. The "Trachea" curve is an oxygen waveform as measured in the *in vitro* airway replica experiments. Each subsequent curve shows the oxygen fraction waveform varying in time as it is transported through the airways, up to the terminal bronchioles (generation 14) that mark the boundary with the acini. Figure 3.9 summarizes simulation

results, showing the volume of oxygen delivered to the trachea, the volume of oxygen transported to the acini, and the ratio of acinar to tracheal volume of oxygen delivered (i.e. the acinar oxygen delivery efficiency).

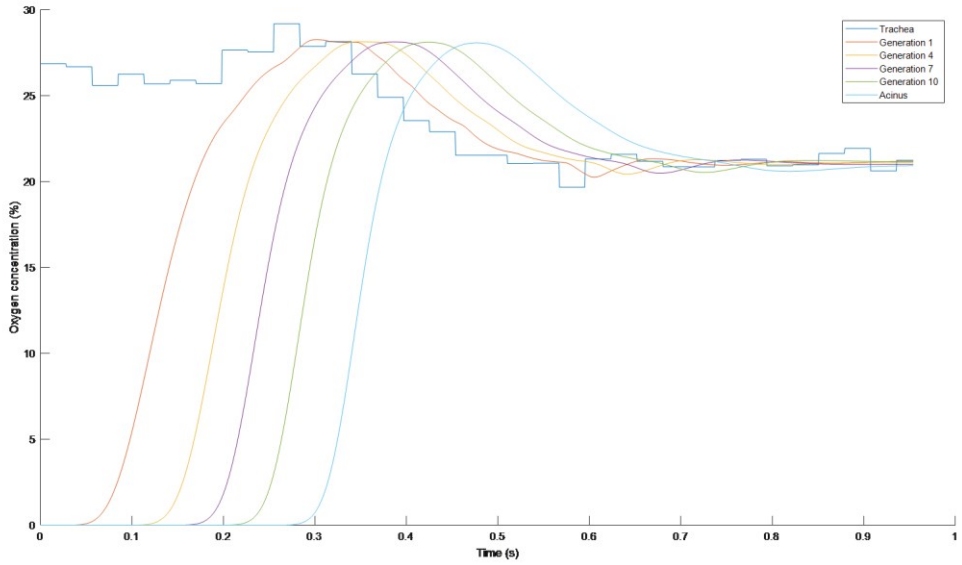

Figure 3.8. Sample output of MATLAB simulation (SimplyGo Mini, exercise breathing pattern, device setting 5). The Trachea line represents oxygen concentration passing the trachea over time determined by the in vitro experiments. Oxygen passing generation 14 enters the gas exchange regions of the lung.

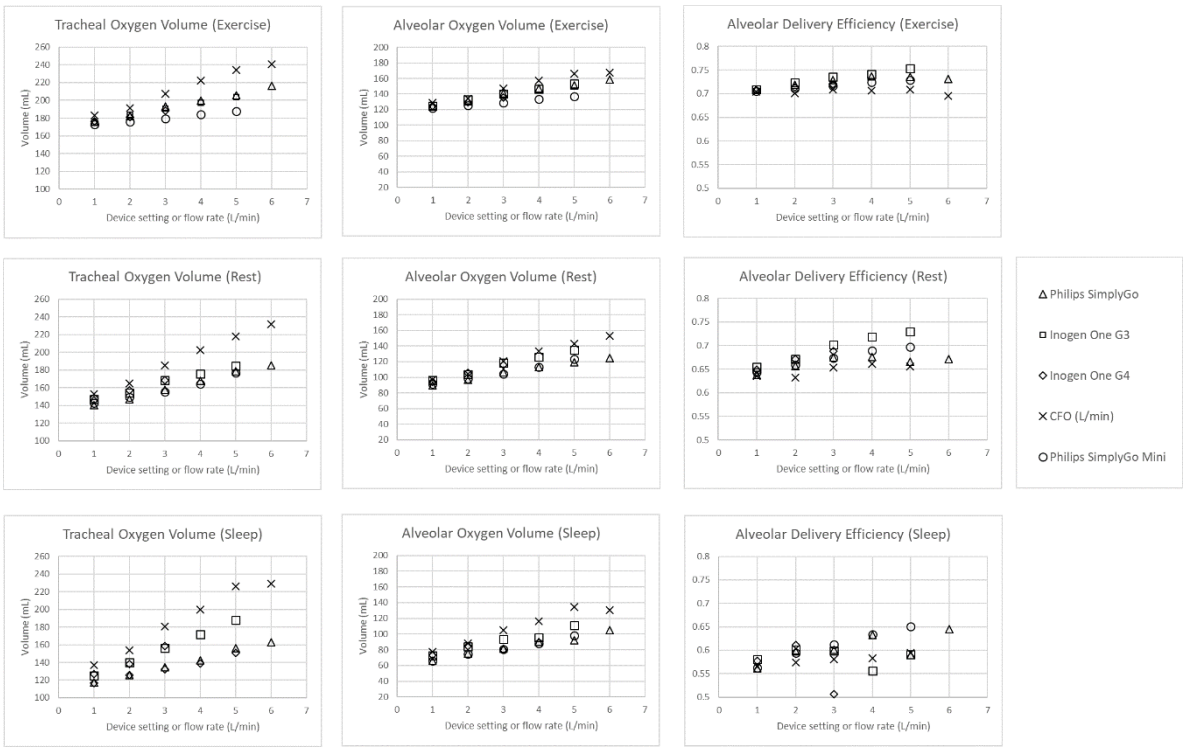

Figure 3.9. Volumes of oxygen passing through the trachea, passing into the alveolar region, and the ratio of these two numbers (i.e. a measure of the fraction of the oxygen passing the trachea that reaches the alveolar region) for all tested portable oxygen concentrators and continuous flow oxygen.

Generally, acinar oxygen delivery efficiencies were positively correlated with increasing breathing minute volume. While all of the devices showed an increase in efficiency with increasing device setting in the exercise and rest cases, for the sleep case the SimplyGo Mini was the only device in which this trend persisted.

Efficiencies for PF were generally higher than those for CFO. However, absolute oxygen delivery to the gas exchange region remained lower for PF than for CFO, at nominally equivalent settings and flows (Figure 3.9). Differences in oxygen delivery between CFO and

PF were smaller at the acinar region than at the trachea. On average, lower minute volumes resulted in higher differences in delivered oxygen volume.

3.4 Discussion

In this study we compared the performance of PF oxygen delivery from POCs to CFO delivery from a stationary, cylinder source. Overall, the results corroborate conclusions from previous studies in that there is no general equivalence in oxygen delivery between CFO in L/min and any of the nominally equivalent PF settings for the POCs we tested [29,30,53]. At most numerical pulse settings, volume-averaged tracheal FiO2 was significantly lower, in both a statistical and an anticipated clinical sense, for pulsed delivery than for a nominally equivalent CFO flow (Figure 3.5). Statistically, differences in FiO2 between the four POCs studied occurred more frequently at higher device settings (Table 3.4), indicating that differences in performance between devices become more pronounced as oxygen delivery increases. This is corroborated by the fact that anticipated clinically significant differences in FiO2 also tended to occur more frequently at higher device settings/CFO flows.

Large differences in pulse volumes between POCs at the same numerical device setting tended to result in large differences in volume-averaged FiO2. It was observed that the Inogen devices modulate pulse volumes based on breathing frequency to maintain relatively similar volumes of oxygen delivered per minute, while the SimplyGo and SimplyGo Mini maintained relatively constant pulse volumes for the range of frequencies considered in this study. This resulted in differences in volume-averaged FiO2 between,

e.g., the Inogen One G3 and the SimplyGo. The magnitudes of the differences in volume-averaged F_{IO2} between the One G3 and the SimplyGo are primarily the result of two factors: (1) slower breathing causing the One G3 to increase its per-breath output and (2) shallow breathing causing supplemental oxygen to represent a higher fraction of the total inhaled oxygen. As slow breathing is also associated with shallow breathing in this study, these two effects act synergistically to generate large FiO2 differences for the sleep breathing pattern (Figure 3.5). Conversely, for deep, fast breathing (exercise), the FiO2 difference is essentially nonexistent. Variation in measured tracheal FiO2 between POCs at a given setting could largely be predicted from pulse characteristics (Figure 3.7). Under the present test conditions, and for the POCs tested, pulse timing had a relatively minor influence on oxygen delivery as compared with pulse volume; in other words, the POCs tended to function as intended and deliver pulses early in the inspiratory phase of the breath. Although previous experiments in the literature measuring FiO2 and comparing between PF and CFO modes of delivery exist[19, 20], the choice in the present work to measure oxygen over time at the trachea of a realistic airway model (instead, e.g., of oxygen concentration inside the test lung) is a key methodological difference from past studies [30,53]. In previous studies, the conducting airways were represented using a length of tubing of constant diameter [29,30,53]. In reality, the tracheobronchial tree consists of a series of branching airways with highly variable diameter depending on depth in the lung [56,72]. Therefore, in the present work a more complex, though still idealized, multi-generational mathematical model of the conducting airways was adopted to assess transport from the distal end of the trachea into the acini of the lung.

In the present mathematical model, the initial oxygen concentration in the conducting airways must be independently specified. The choice of a concentration of zero was made in order to model, in absolute terms, the amount of freshly delivered oxygen passing the trachea that was transported in a single inhalation to the acini. The present combination of *in vitro* and *in silico*, or mathematical, modeling approaches inherently includes the influence of pulse timing on efficiency of delivery to the acini because POCs are tested under realistic triggering conditions.

Efficiency of delivery tended to be positively correlated with minute volume (Figure 3.9). That is, efficiencies of the exercise breathing pattern were higher than those of the rest breathing pattern, which were in turn higher than those of the sleep breathing pattern. The arrival of fresh oxygen can be identified in Figure 3.8 as the time at which oxygen concentration increases from zero. Because the model accounts for both convection and diffusion, a greater inhalation velocity transports gas and therefore oxygen more quickly, leading to an earlier arrival time at each generation of the airway and a higher delivery efficiency as a result.

Predicted efficiency of pulse delivery to the acini (Figure 3.9) still varied to some extent between POCs and POC settings for the same breathing pattern. This variability results from differences observed in the *in vitro* experiments in the timing with which pulses arrived at, and swept past, the trachea, and from differences in the volume of the oxygen pulse delivered.

Overall, PF was predicted to offer advantages in efficiency of delivery, in that the fraction of oxygen delivered to the trachea which reaches gas exchange lung regions was predicted in

general to be greater for PF than for CFO (Figure 3.9). This is due to the oxygen that remains in the anatomical dead space at the end of inhalation in CFO, and never reaches the gas exchange regions. But efficiency does not necessarily imply efficacy; volumes of oxygen delivered to the acini using CFO were still in most cases higher than those using PF. As noted by McCoy, oxygen delivery must first and foremost meet the therapeutic needs of the patient [5]. Differences in oxygen delivery reported herein between CFO and PF settings therefore highlight the need to titrate delivery settings to achieve a target oxygen saturation using the same delivery device as used at home [5]. Results of *in vitro* experiments and *in silico* analysis, such as those presented here, may inform this process by anticipating differences in oxygen delivery between devices and modes of administration and thereby aiding health practitioners in selecting optimal devices for their patients.

3.5 Conclusions

In this study, *in vitro* experiments using a realistic upper airway replica were performed to compare CFO oxygen delivery with PF from four commercial POCs. Volume-averaged FiO2 measured at the trachea was evaluated for three simulated breathing patterns, representative of COPD patients at rest, during light exercise, and while asleep. FiO2 was not equivalent between PF and CFO flow, and differences in oxygen delivery were largest when high PF setting numbers were combined with low minute volume of respiration. Anticipated clinically significant differences (>2% absolute difference in FiO2) were observed at all nominally equivalent pulse flow settings higher than 2. Significant differences in oxygen delivery were also measured between different POCs operated at

identical numerical PF settings, with the clinically significant differences occurring at the highest setting numbers (3 or 5, depending on device).

By coupling *in vitro* measurements with a mathematical model of oxygen transport through the conducting airways, it was predicted that PF is generally more efficient than CFO at delivering oxygen from the trachea to the acini. However, acinar oxygen delivery remained lower for PF than for CFO, at nominally equivalent setting numbers and flow. Significant differences in oxygen delivery persisted to the acini between POCs operating at identical PF settings.

Chapter 4: In Vitro Assessment of an Idealized Nose for Nasal Spray Testing: Comparison with Regional Deposition in Realistic Nasal Replicas

4.1 Introduction

In vitro assessments with realistic nasal replica based on airway geometries obtained from magnetic resonance imaging (MRI) or computerized tomography (CT) scans are an attractive intermediate step for researchers and drug developers on the path from assessment of spray properties to more expensive and time consuming *in vivo* experiments in humans. The effect of parameters such as actuation force, administration angle and spray cone angle can be systematically investigated with *in vitro* experiments that preserve anatomical realism while limiting costs as compared with *in vivo* studies. While it is expected that *in vivo* studies will remain a part of device development in the future, higher resolution nasal replicas enabled by advances in rapid prototyping and other 3D printing technologies, as well as innovative methods of, have become increasingly useful in device development as a way to more quickly iterate through and define appropriate parameter spaces during device development and clinical trials [16,34,35].

Sectioned nasal replicas, built using traditional manufacturing techniques or via rapid prototyping, have proven particularly useful in assessing regional deposition of nasal sprays. Following device actuation, such replicas can be disassembled into their constituent parts based on anatomical regions of interest for assaying of deposited drug within each region. For the limited number of sectioned replicas that have been built, airway geometries have usually been segmented from medical images taken for a single, individual subject. However, intersubject variability in nasal geometry, and associated intersubject

variability in droplet deposition, is known to be large. At a given impaction parameter (the product of the square of particle aerodynamic diameter and inspiratory flow rate), regional deposition of particles depositing in the nasal airways varies dramatically, owing to differences in nasal airway geometry between subjects. Accordingly, it is unlikely that any single sectioned airway replica based on a geometry derived from one individual subject is appropriate for evaluating expected nasal spray deposition patterns in a larger patient population. Instead, a validated standardized geometry mimicking average regional deposition in a set of realistic geometries would be useful to drug developers when exploring suitable parameters for use during device and formulation development, and to guide pharmaceutical trials. To this end, researchers have previously developed a standardized human nasal cavity (the Carleton-Civic standardized geometry) based on geometric averaging of a set of nasal CT [45]. Total micrometer-sized aerosol deposition in the standardized geometry was later shown to lie at the lower extreme of *in vivo* data [74]. Kiaee et al. suggest that the low deposition of the Carleton-Civic standardized geometry when compared with *in vivo* data might be due to the nonlinearity of regional deposition as a function of the geometric characteristics of the geometry [46]. Therefore, one would not expect a linear average of the geometric features of a set of replicas to produce the average regional deposition in that set. Instead, Kiaee et al. proposed a new geometry based on extensive CFD simulations in a set of realistic nasal geometries [46,75]. CFD is well established in exploring the deposition behaviour in computational meshes based on realistic nasal airways, and allows researchers to simulate total and regional deposition for a large parameter space (particle size, velocity, orientation) relatively quickly

when compared to *in vitro* or *in vivo* experiments. The idealized geometry proposed by Kiaee et al. was able to mimic the average regional deposition pattern of the wider set of realistic nasal airways while retaining relative geometric simplicity, thus making it a promising candidate for manufacture and *in vitro* validation [46].

The objective of the present study is to build a physical realization of a proposed candidate geometry described by Kiaee et al., and to determine if the *in vitro* regional deposition pattern of nasal spray droplets in the idealized geometry is able to mimic the average deposition pattern found in a set of realistic nasal replicas.

4.2. Methodology

4.2.1 CT scan segmentation and smoothing

An initial set of anonymized CT scans of 12 individuals, including both males and females, and containing the nasal airways were obtained as described by Kiaee et al. [46]. These 12 CT scans were obtained retrospectively from patients scanned for clinical purposes at the University of Alberta Hospital with approval from the Health Research Ethics Board. The average age of the scanned subjects was 60 years of age. The nasal airways of the patients were assessed as normal at time of scanning, and the CT scans of the nasal airway were later assessed as normal by a radiologist. Imaging was performed on a Siemens Somatom Flash or Definition scanner with a reconstructed slice thickness of 1 mm and in-plane resolution of 0.035 to 0.039 mm.

The DICOM files from the CT images were processed by using ScanIP (Simpleware, UK), which involved removal of the sinuses and segmentation to define the nasal airways

proximal to the upper trachea, and included the laryngeal region. This segmentation process was performed manually and no global sectioning functions were applied to the geometry. In the course of this process, two of the CT scans were deemed unusable because of unfixable geometric anomalies, reducing the total set of geometries to 10. The resulting airway surfaces were smoothed locally using Meshmixer (Autodesk, USA), followed by iterative global smoothing with 3-maticSTL (Materialize, UK). Smoothing was stopped when the change in the surface area to volume ratio between successive smoothing iterations became less than 0.01.

The smoothed surfaces were then sectioned into anatomical regions of interest based on the existing literature [42,44]. These regions were the nasal vestibule, nasal valve, the anterior turbinates, the posterior turbinates, the olfactory region and the nasopharynx. The exact boundaries between each region were created manually based on anatomical features shared by all geometries and were verified by a radiologist.

4.2.2 Creation of the realistic nasal replicas

The resulting sectioned geometries were imported into 3-maticSTL for further manipulation. To build the replicas, it was necessary to first subtract the sectioned geometry from a solid in order to produce a “negative” cavity appropriate for deposition experiments. First, a primitive solid box was created from which some excess material was removed, keeping in mind the practical necessity of adding connections between each section. Then, the box was cut along the previously defined boundaries of the anatomical regions of interest. Pins and holes for screws were then added for easy alignment and

assembly following manufacture. Finally, each section of the nasal geometry was subtracted from the sectioned block to create the cavity representing the real airway. These finished parts were then built using rapid prototyping in plastic (Objet VeroGray RGD850; Stratsys, Ltd., Eden Prairie, Minnesota, USA) using a PolyJet 3D printer (Objet Eden 350V High Resolution 3D Printer; Stratsys, Ltd., Eden Prairie, Minnesota, USA).

4.2.3 Creation of the idealized geometry using CFD

The candidate idealized geometry selected for manufacture has been previously described and a full of account of the development process can be found in Kiaee et al. (2019) [46,76]. Briefly, an initial idealized geometry was first developed using non-uniform rational B-splines (NURBS). This geometry was then improved iteratively based on CFD simulations and comparisons with seven realistic geometries created from the aforementioned CT scans.

Geometric flaws in the sectioned geometries (e.g., excessively high aspect ratio, missing triangles, excessive node density, and self-intersections) were further repaired by using Netfabb (Autodesk, San Rafael, California, USA) and MeshLab (Visual Computing Laboratory, Italy).

The final candidate idealized geometry, dubbed the monolithic idealized geometry by Kiaee et al., was able to mimic the average *in silico* regional deposition in the set of the realistic geometries well, particularly at the larger particle sizes [46,76]. It should be noted that in that comparison, the anterior and posterior turbinates were combined to form a combined turbinates region.

4.2.4 Manufacture of the idealized replica

The monolithic idealized geometry of Kiaee et al. was first imported into Netfabb [46]. To produce a thin shell around the airway cavity, the solid version of the idealized geometry was then extruded in three dimensions approximately 4 mm outwards and then remeshed to smooth the external surface. Then, the original solid idealized geometry was subtracted from the extruded version, resulting in the idealized nasal geometry. The geometry was then sectioned along the given boundaries, and pins and holes were added for alignment afterwards. In addition, a short cylindrical element (length: 9 mm, internal diameter: 17 mm, outer diameter: 24 mm) was added to the exit of the nasopharynx to facilitate the attachment of a filter. Figure 4.1 shows the completed geometry prior to manufacture. The parts of the resulting idealized replica were manufactured, as with the realistic replicas, in VeroGrey plastic using a PolyJjet 3D printer.

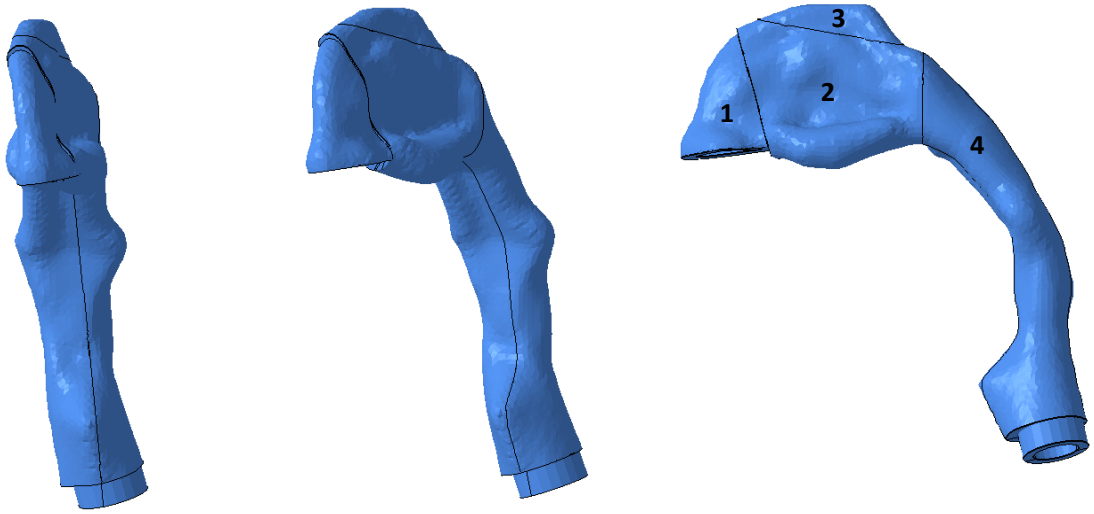

Figure 4.1. Three computer rendered perspective views of the idealized replica. Anatomical regions of interest are labeled as follows: 1) nasal entrance, 2) turbinates, 3) olfactory region, 4) nasopharynx.

4.2.5 Deposition experiments

4.2.5.1 Cromolyn sodium nasal spray pump

Cromolyn sodium (CS) nasal spray pumps (NasalCrom, Fisons Pharmaceuticals, Ipswich, UK) were obtained to allow comparison with previous *in vivo* gamma scintigraphy work [77]. Each milliliter of CS formulation solution contains 40 mg cromolyn sodium in water with trace amounts of benzalkonium chloride to preserve and edetate disodium to stabilize the solution. Each spray pump contains 13 mL of formulation, with a label claim of 100 doses per spray pump (5.2 mg of cromolyn sodium per actuation). The same device and formulation were used in the aforementioned *in vivo* study [77].

4.2.5.2. Actuation parameters

The cromolyn sodium spray pump was actuated by a Nasal Spray Products Universal Actuator (InnovaSystems Inc., Mooretown, New Jersey, USA). Force of actuation, force rise time, force hold time and force fall time were based on mean values measured in adults previously reported in Doughty et al. (Doughty et al., 2010) and are shown in Table 4.1 [78]. Angles of administration (defined as the angle the spray pump nozzle makes with the lab bench surface, measured from the horizontal) were chosen in accord with the existing *in vitro* literature and to mimic patient use. Based on a review of the literature, two angles, 60° and 45°, were ultimately chosen based on their high frequency of occurrence in a large number of *in vitro* nasal replica studies [32,35,42,79,80].

Actuation force (N)	5.82
Rise time (ms)	270
Release velocity (mm/s)	34.87
Expected stroke length (mm)	5.62

Table 4.1. Actuation parameters for automated repeatable mechanic actuation of the nasal spray pump. Obtained from Doughty et al. (2011) [78]. Actuation force is the maximum force during the actuation, rise time is the time required to reach the maximum force while actuating the pump, release velocity is the velocity in releasing the pump and expected stroke length is the maximum displacement of the pump during actuation. Each parameter is a mean value averaged across 20 healthy adults.

4.2.5.3 Experimental procedure

A schematic of the experimental apparatus is shown in Figure 4.2. The orientation of each nasal replica was set such that the plane of the entrance to the nostril was parallel to the bench surface, and the sagittal plane of the replica was aligned parallel with the direction of the nozzle of the spray pump. A filter was attached to the outlet of the replica to collect any droplets penetrating the replica. To simulate quiet breathing through a single nostril, a vacuum pump was used to generate an initial inspiratory flow, which was then manually adjusted to a volumetric flow rate of 7.50 ± 0.01 L/min using a gate valve while monitoring a flow meter (Model 4143, TSI, Shoreview, Minnesota, USA), The contralateral nostril was plugged, the spray pump was then set to the appropriate administration angle and placed relative to the opening of the open nostril such that the tip of the nozzle just penetrated the opening to the nostril. For about half of the geometries, the nozzle diameter was too wide to achieve the necessary penetration. As this does not reflect proper usage of the spray pump *in vivo* and is therefore likely to cause large deviations in device performance, these geometries were excluded from consideration in the final analysis, leaving five geometries for which experimental data was obtained here (4 replicas with both nostrils, and one with a single nostril).

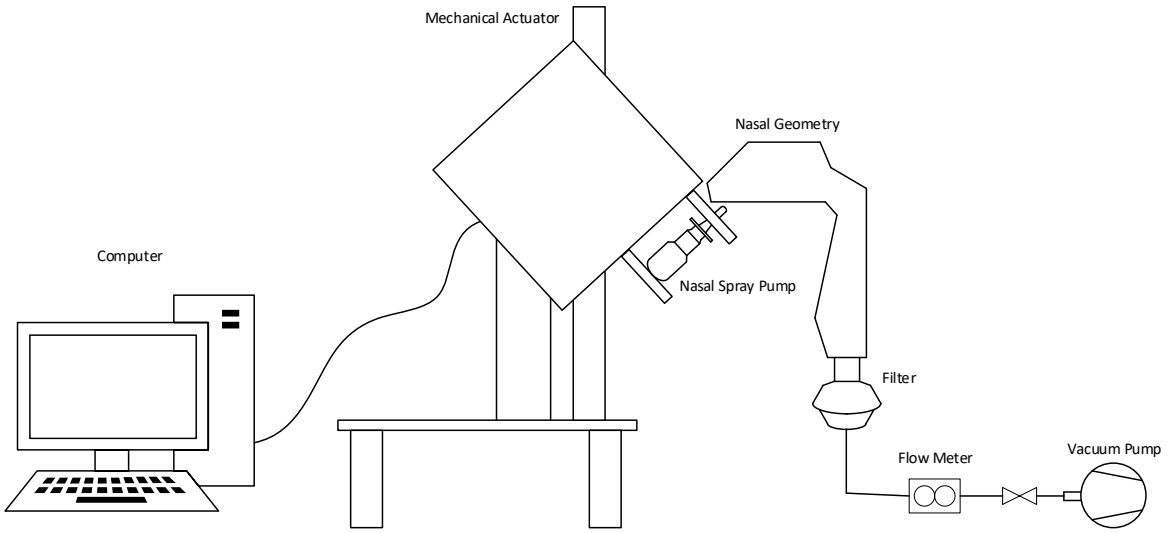

Figure 4.2. Schematic of experimental setup.

The nasal spray pump was primed by actuating twice into a plastic bag prior to actuation into the replica. After double-checking for proper alignment of the spray nozzle with the nostril, a single shot was then sprayed into the open nostril. The vacuum pump was then immediately turned off and any CS solution that had dripped out of the open nostril or had deposited on the external surfaces of the replica was wiped and collected using a small piece of cotton gauze. The replica was disassembled immediately and carefully to avoid transfer of deposited CS solution between different replica parts. These parts, in addition to the attached filter and the cotton gauze, were then washed with distilled water, and the mass deposited in each part, in the filter and collected by the wipe were determined using an ultraviolet (UV) spectrophotometer (Cary 8454 UV - VIS System, Agilent Technologies, Santa Clara, California, USA). The absorbances of the CS solutions were measured at a wavelength of 327 nm. Total mass recovery in all cases consistently exceeded than 85%.

Three repeats were performed (n =3) to assess repeatability in each angle/geometry condition.

4.2.5.4 In vitro data analysis

To describe *in vitro* deposition, data is presented as the relative fraction depositing on the nasal surfaces, excluding the fraction collected from dripping or the external surfaces. In other words, the deposition fraction in a specific region was calculated by dividing the mass of CS deposited on each region by the difference between total mass of CS recovered and the mass of CS collected from dripping or wiped from the external geometry surface. This was done in order for later comparison with the available *in vivo* gamma scintigraphy data, which also presents relative fractions of CS depositing in the nasal cavity only, excluding any CS that may have potentially dripped from the noise. To compare with the idealized geometry, the mean of the three repeats for each geometry were averaged together to obtain a grand mean across all realistic geometries.

4.3. Results

4.3.1 Variability across realistic geometries

Figures 4.3 and 4.4 show regional deposition in the realistic nasal replicas at both of the tested angles and provides a sense of the inter-subject variability in regional deposition. In general, run-to-run repeatability in deposition was moderate and varied considerably between replicas. For the 60° case, the majority of the deposition occurred in the valve and vestibule region, but with considerable inter-subject differences. For the 45° case, there was on average relatively more deposition in the anterior and posterior turbinates than at 60°.

Broadly speaking, it is clear that lowering the deposition angle towards the horizontal tends to cause a higher fraction of the drug dose to penetrate the nasal valve, consistent with previous *in vitro* studies assessing regional deposition in realistic nasal replicas [32,80]. At both angles, a negligible mass of CS deposited on the filter (which here represents the mass of CS penetrating into the lower airways) and no nasopharyngeal deposition was observed in any of the geometries. Olfactory deposition was also negligible at both orientations, with non-zero olfactory deposition only observed in a single replica, indicating that the present nasal spray is generally unsuited for targeted drug delivery to this region of the nasal cavity.

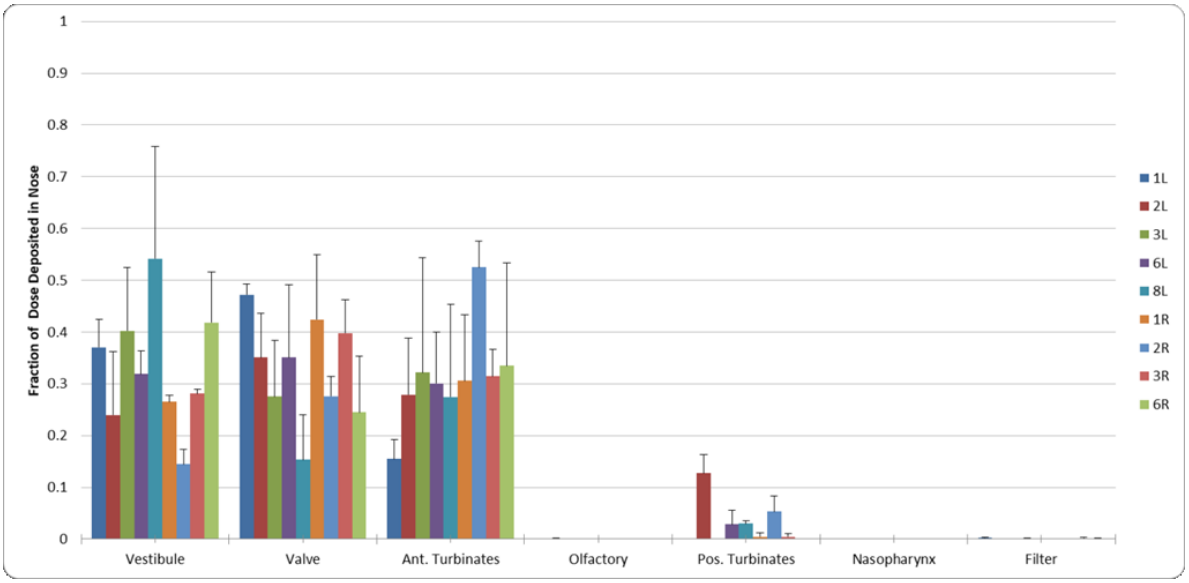

Figure 4.3. Regional deposition of cromolyn sodium in 5 realistic nasal replicas (number indicates the subject number; L for left nostril; R for right nostril) delivered in separate experiments into the right and left nostrils of each replica, administered at an angle of 60° from the horizontal, inhalation flow rate of 7.5 L/min. Three experimental repeats were done for each geometry; error bars indicate one standard deviation.

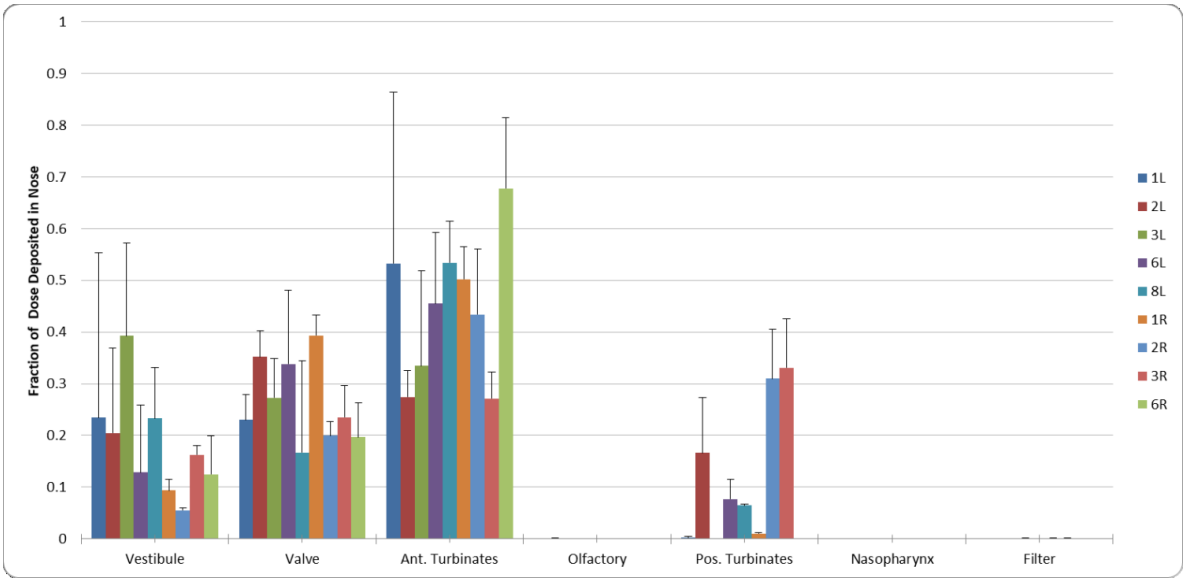

Figure 4.4. Regional deposition of cromolyn sodium in 5 realistic nasal replicas (number indicates the subject number; L for left nostril; R for right nostril) delivered in separate experiments into the right and left nostrils of each replica, administered at an angle of 45° from the horizontal, inhalation flow rate of 7.5 L/min. Three experimental repeats were done for each geometry; error bars indicate one standard deviation.

4.3.2 Comparing realistic and idealized

Because *in vivo* data typically only resolves the nasal region into a few subregions, here we combined the valve and vestibule deposition fractions into a common "entrance region" for comparison purposes. In addition, for the realistic geometries, the anterior and posterior turbinate sections were combined into a common turbinates section for comparison with the *in vivo* data and the deposition in the idealized replica. Figures 4.5 and 4.6 show the grand means of regional deposition across the five tested realistic nasal replicas compared with the regional deposition pattern observed from the idealized nasal replica at 60° and 45°, respectively. Overall, excellent agreement is seen in deposited drug deposition fractions

between each of the corresponding regions of the averaged realistic nasal replicas and the idealized nasal replica. In other words, the idealized replica accurately mimics the averaged deposition fractions of the realistic replica in all regions for both of the orientations considered.

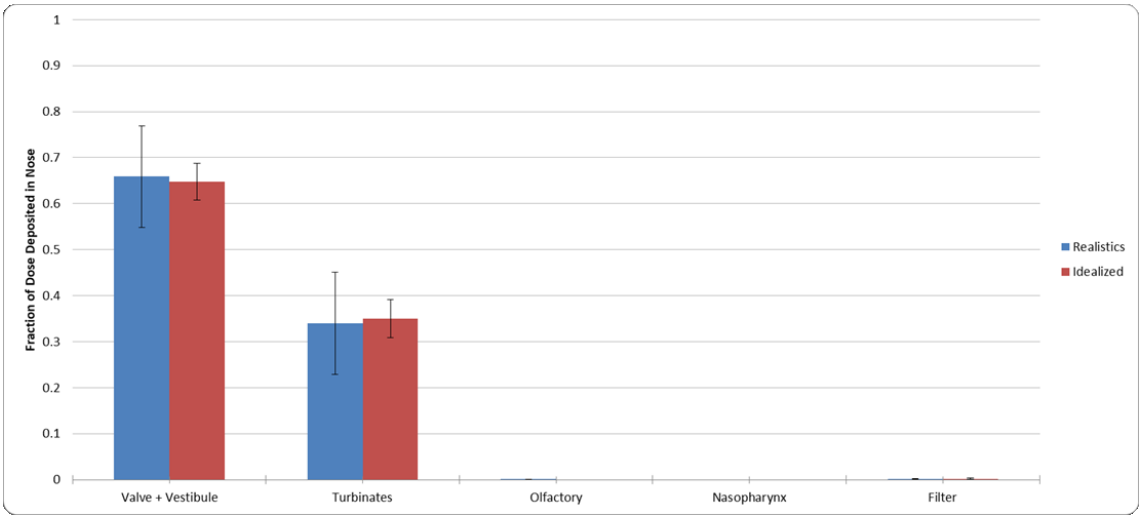

Figure 4.5. Comparison of regional deposition of cromolyn sodium in realistic vs. idealized nasal replicas (60°). Deposition in realistic replicas presented as average over all realistic nasal replicas. Error bars for the realistics indicate one standard deviation (measured across geometries). Error bars for the idealized also indicate one standard deviation (variation in three experimental repeats).

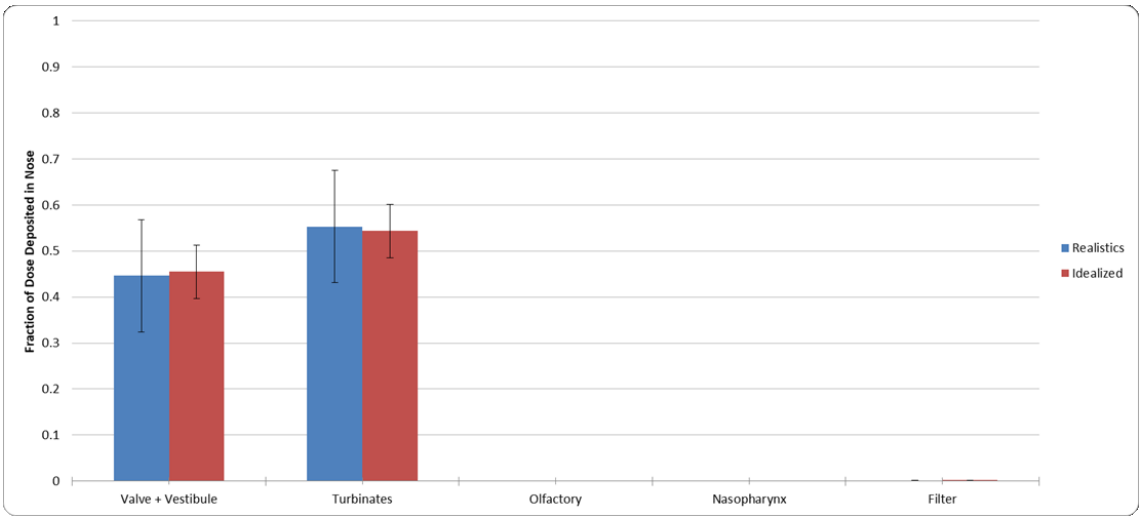

Figure 4.6. Comparison of regional deposition of cromolyn sodium in realistic vs. idealized nasal replicas (45°). Deposition in realistic replicas presented as average over all realistic nasal replicas. Error bars indicate one standard deviation (measured across geometries). Error bars for the idealized also indicate one standard deviation (variation in three experimental repeats).

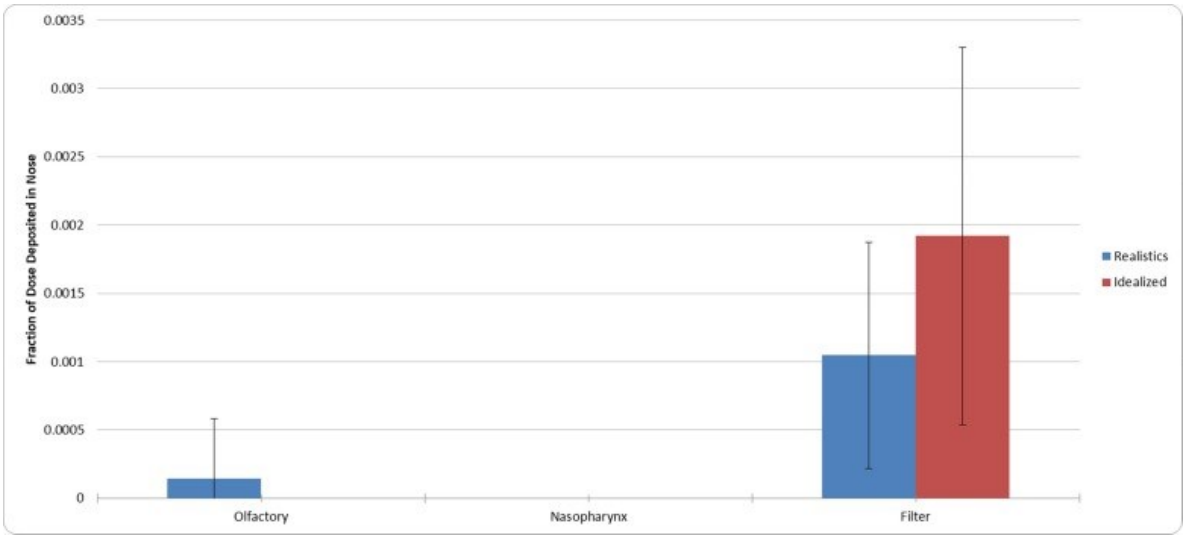

Figure 4.7. Comparison of regional deposition of cromolyn sodium in realistic vs. idealized nasal replicas (60°) with y-axis magnified to show olfactory and filter deposition. Values below our range of detectability are not shown.

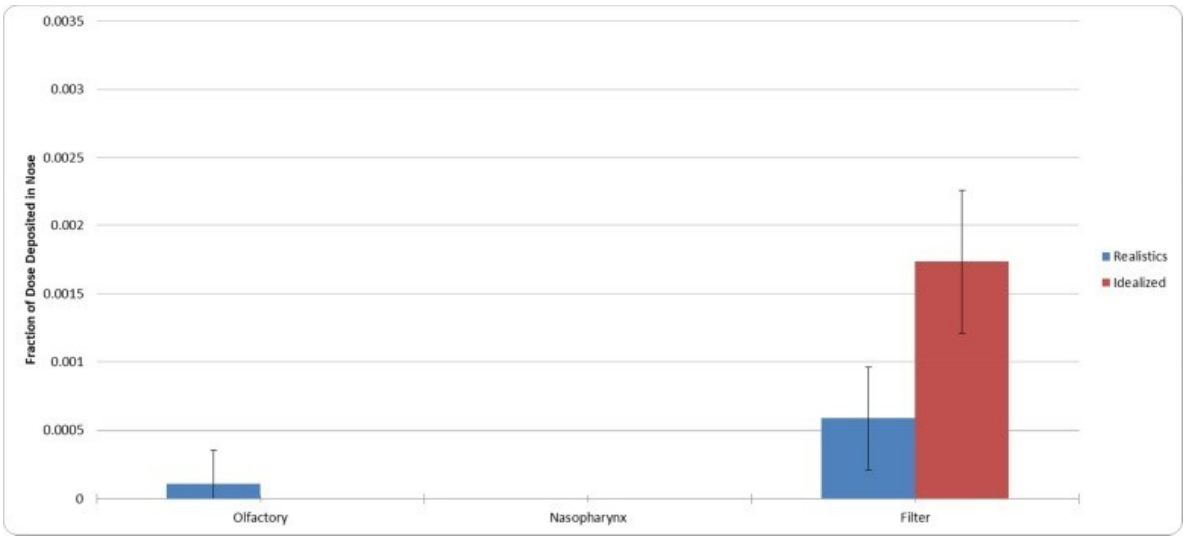

Figure 4.8. Comparison of regional deposition of cromolyn sodium in realistic vs. idealized nasal replicas (45°) with y-axis magnified to show olfactory and filter deposition. Values below our range of detectability are not shown.

4.4. Discussion

While Figure 4.5 and 4.6 show excellent agreement between the idealized replica and average deposition data from the *in vitro* realistic replicas, it is also useful to examine the ability of the idealized nasal replica to predict *in vivo* deposition. Al-Ghananeem et al. performed a gamma scintigraphy study of *in vivo* regional deposition and clearance in a group of 5 healthy male volunteers using two radiolabeled CS formulations (one brand and one generic), both of which are believed to be essentially the same as the CS formulation used in the present study [77]. *In vivo* anatomical regions of interest in the nasal cavity were defined by them as the anterior nasal cavity, the posterior nasal cavity and the nasopharynx. These regions correspond approximately to the entrance, turbinates and nasopharynx regions in the idealized nasal replica, respectively. In the *in vivo* studies, the averaged fraction of deposited CS across all subjects in the anterior region was

approximately 0.55 and 0.6 for the generic formulation and the brand formulation, respectively. Averaged fractions of deposited drug in the posterior region were approximately 0.45 for the generic formulation and 0.4 for the brand formulation, respectively. Anterior region and posterior region deposition displayed considerable variability across tested subjects. Deposition in the nasopharynx region was negligible *in vivo* in both formulations. This is in agreement with the *in vitro* deposition patterns observed in the present idealized nasal replica, with deposition fractions in the nasal cavity entrance ranging from 0.45 to 0.65, depending on orientation, and deposition in the turbinates ranging from 0.35 to 0.55. Given that the sectioning methodology between the present study and the *in vivo* study prevents exact comparison, and that the administration angle was not reported by Al-Ghananeem et al., the idealized replica presented in this paper appears to satisfactorily mimic averaged *in vivo* regional deposition for the nasal spray pump tested [77].

While these preliminary results are promising, a few caveats bear mentioning. One concern (shared with the *in vivo* study used for comparison) is that all regional deposition patterns were based exclusively on anatomically normal nasal cavities, which therefore precludes consideration of individuals with conditions that alter the shape of the nasal cavity. Previous studies using CFD simulations have demonstrated that regional deposition changes significantly in the presence of anatomical abnormalities or deformations in the nasal cavity [81,82]. Therefore, the applicability of the idealized nasal replica to this sub-population remains an open question. Another limitation of the present study is the use of only a single nasal spray pump for validation of the idealized replica. However, it is worth

noting that for nasal spray pumps, a survey of the droplet size distribution measurements of water-based droplets in the literature indicates that key distribution parameters such as Dv10, Dv50 and Dv90 do not vary dramatically between different formulations and spray pumps [83,84]. In addition, previous investigations that varied the droplet size distribution found conflicting evidence as to whether droplet size affected *in vitro* regional deposition patterns meaningfully in the 10 to 100 μm droplet diameter range [31,32]. Regardless, given the encouraging results presented in this paper, validation using a wider set of nasal spray pumps and other intranasal drug delivery devices would be a worthwhile topic for future study.

4.5 Conclusion

In this study, an idealized nasal replica was designed and subsequently manufactured in plastic based on a candidate idealized nasal airway geometry previously developed and tested using CFD simulations. The ability of the idealized replica to mimic average regional nasal deposition of nasal spray droplets in a population of subjects was assessed via benchtop *in vitro* experiments. The idealized replica was able to accurately reproduce the average *in vitro* regional deposition patterns at two separate spray orientations in a set of five realistic nasal airway replicas derived from CT scans. Furthermore, the idealized nasal replica agreed with data obtained by other authors using *in vivo* gamma scintigraphy, bearing in mind the spray orientation used *in vivo* is unknown, as are the exact definitions of *in vivo* borders between the anatomical regions of interest in the nasal cavity.

The idealized replica presented here might be of interest to drug developers seeking to expedite benchtop testing of nasal spray pumps and other intranasal drug devices during research and development.

Chapter 5: *In Vitro* Regional Deposition of Nasal Sprays in an Idealized Nasal Inlet: Comparison with *In Vivo* Gamma Scintigraphy

5.1. Introduction

Benchtop *in vitro* test methods are vital to researchers and drug developers seeking to understand or characterize the performance of medical aerosols and nasal sprays. For example, a US Food and Drug Administration Guidance Document contains standardized *in vitro* procedures for the measurement of properties for a range of medical aerosol products such as delivered dose uniformity, aerodynamic size distribution and fine particle fraction that facilitate easy comparisons between different products and give some idea of the possible behavior of the product *in vivo*. Knowledge of the spray characteristics of a test formulation can be particularly valuable in the early stages of product development, where parameter refinement based on early feedback from *in vitro* experiments can save time later in the development process when testing moves to an *in vivo* setting. Measured *in vitro* parameters are also intended to provide a convenient way to support assessment of bioavailability and bioequivalence of different nasal spray products, and should ideally be highly discriminating between products [6,21,22]. However, the strength of correlation between *in vitro* measurement parameters and relevant *in vivo* responses remains uncertain and is a topic of frequent debate.

In the related field of aerosol drug delivery to the lungs, researchers have described *in vitro* methods using idealized or selected realistic airway geometries that mimic average deposition measured in *in vivo* studies [23,85–92]. These geometries can function as a reference for *in vitro* experiments or *in silico* simulations, facilitating prediction of *in vivo*

performance at early stages of drug or device development, and allowing comparable results to be obtained between laboratories.

For nasal drug delivery, a representative geometry mimicking average *in vivo* regional spray deposition across a wide parameter space has not been definitively established, despite significant past research effort [36,44,93,94]. Recently, a new geometry was proposed based on extensive CFD simulations performed in a set of realistic nasal geometries [76]. In a subsequent publication, Chen et al. (2020) designed and executed an *in vitro* study to validate the performance of the idealized geometry, fabricated in plastic using stereolithography, against a set of realistic adult nasal airway replicas [95]. The plastic idealized geometry was able to mimic the regional deposition of nasal spray droplets averaged across a set of 9 nasal realistic geometries. However, due to the limitations of the plastic construction of the geometry, only water was suitable as a solvent for extracting deposited drug from geometry surfaces, and thus only one nasal spray product was tested. To test an expanded range of nasal drug delivery products and ease the constraint on the choice of appropriate solvents for assaying, it is necessary to change the material of construction of the idealized geometry from plastic to metal. To that end, the Alberta Idealized Nasal Inlet (AINI; Copley Scientific, UK), an aluminum version of the idealized geometry described above, has been designed and manufactured.

The objective of the current study is to compare regional nasal deposition measurements made using the AINI with average *in vivo* regional deposition data across a range of nasal drug products. Regional deposition with an aqueous solution formulation will additionally

be compared with previously published *in vitro* data collected in realistic nasal airway replicas.

5.2. Materials and Methods

5.2.1 Intranasal drug formulations

The choice of intranasal drug formulations for testing was motivated by two primary concerns. The first was to establish continuity of performance of the aluminum AINI with the version previously manufactured in plastic, and the second was to enable comparison of obtained *in vitro* regional deposition data with corresponding *in vivo* gamma scintigraphy data previously published in Al-Ghaneneem et al. (2008) and Leach et al. (2015) [77,95,96]. Accordingly, one aqueous solution formulation (cromolyn sodium; NasalCrom, Fisons Pharmaceuticals, Ipswich, UK), one aqueous suspension formulation (mometasone furoate; Nasonex, Merck & Co., Kenilworth, NJ, USA) and one nasal pMDI using HFA 134a as a propellant (beclomethasone dipropionate; QNASL, Teva Pharmaceutical Industries, Tikva, Israel) were selected to encompass a range of devices and formulations.

Each Nasalcrom spray pump contains 13 mL of aqueous cromolyn sodium solution, with a label claim of 100 doses per spray pump (5.2 mg of cromolyn sodium per actuation). Nasonex spray pumps contain 120 doses of aqueous mometasone furoate suspension (50 μg per actuation). Finally, each QNASL inhaler contains 120 doses of HFA-beclomethasone dipropionate formulation (80 μg per actuation).

5.2.2 Actuation parameters

Each device was mechanically actuated by a Nasal Spray Products Universal Actuator (InnovaSystems Inc., Mooretown, New Jersey, USA). For the two nasal spray pumps (NasalCrom and Nasonex), force of actuation, force rise time, force hold time and force fall time were set according to mean *in vivo* values measured in adults previously reported in Doughty et al. (Doughty et al., 2010) and are shown in Table 5.1. For QNASL, as is the case for pMDIs in general, it has been established that dosing is relatively insensitive to the aforementioned actuation parameters as long as the actuation force remains above a minimum threshold [97]. Insensitivity of the mass of the delivered dose with respect to actuation force in QNASL was confirmed in preliminary tests, with actuation forces ranging from 60 N to 116 N. For deposition experiments, the actuation force for QNASL was set at 57.09 N (5.82 kg), which is well above the typical minimum force thresholds measured *in vivo* that are reported in the scientific literature [97–99].

Actuation force (kg)	5.82
Rise time (ms)	270
Release velocity (mm/s)	34.87
Expected stroke length (mm)	5.62

Table 5.1. Actuation parameters for automated repeatable mechanic actuation of the nasal spray pump obtained from Doughty et al. (2011) [78]. Actuation force is the maximum force during the actuation, rise time is the time required to reach the maximum force while actuating the pump, release velocity is the velocity in releasing the pump and expected stroke length is the maximum displacement of the pump during actuation. Each parameter is a mean value averaged across 20 healthy adults.

Spray angle orientation (defined here as the angle the spray pump nozzle forms with the horizontal plane parallel to the lab bench surface) was chosen to correspond with the existing *in vitro* literature and to reflect patient use. Two angles, 60° and 45°, were selected both because of their high frequency of occurrence in a large number of *in vitro* nasal replica studies, and because these were the same angles used in our previous study validating the plastic idealized geometry [32,35,42,79,80,95]. Since the nozzle of QNASL is angled 24° above the horizontal when the device is placed flat on the benchtop surface, compensatory adjustments in the mechanical actuator platform orientation were made. A steady inhalation flow rate of 7.5 L/min was chosen to mimic a slow nasal inhalation through a single nostril [95]. Each device required a different number of actuations into the AINI to ensure that quantifiable levels of the active ingredient could be collected for later

UV-Vis spectroscopy: one actuation was used for NasalCrom, four actuations for Nasonex and two actuations for QNASL.

5.2.2 Experimental procedure

A full description of the experimental procedure can be found in Chen et al. (2020) [95]. Briefly, each device was aligned according to the desired spray orientation angle, with the tip of the device raised until just penetrating the AINI inlet, and then actuated into the open inlet of the AINI. An antibacterial filter was connected to the nasopharynx-side outlet of the AINI to capture any non-depositing particles escaping the AINI.

A schematic of the experimental setup is shown in Figure 5.1. After actuation, a cotton wipe was held below the inlet to collect any formulation that may have dripped out of the Vestibule region of the AINI and to wipe benchtop and spray device surfaces after spraying. The AINI was then disassembled, and the filter, cotton wipe and each region were washed in an assay-appropriate solvent (water for NasalCrom; methanol for Nasonex and QNASL). The mass of formulation caught in the filter, collected by the wipe and deposited in each region was then assayed using an ultraviolet-visible (UV-Vis) spectrophotometer (Cary 8454 UV - VIS System, Agilent Technologies, Santa Clara, California, USA).

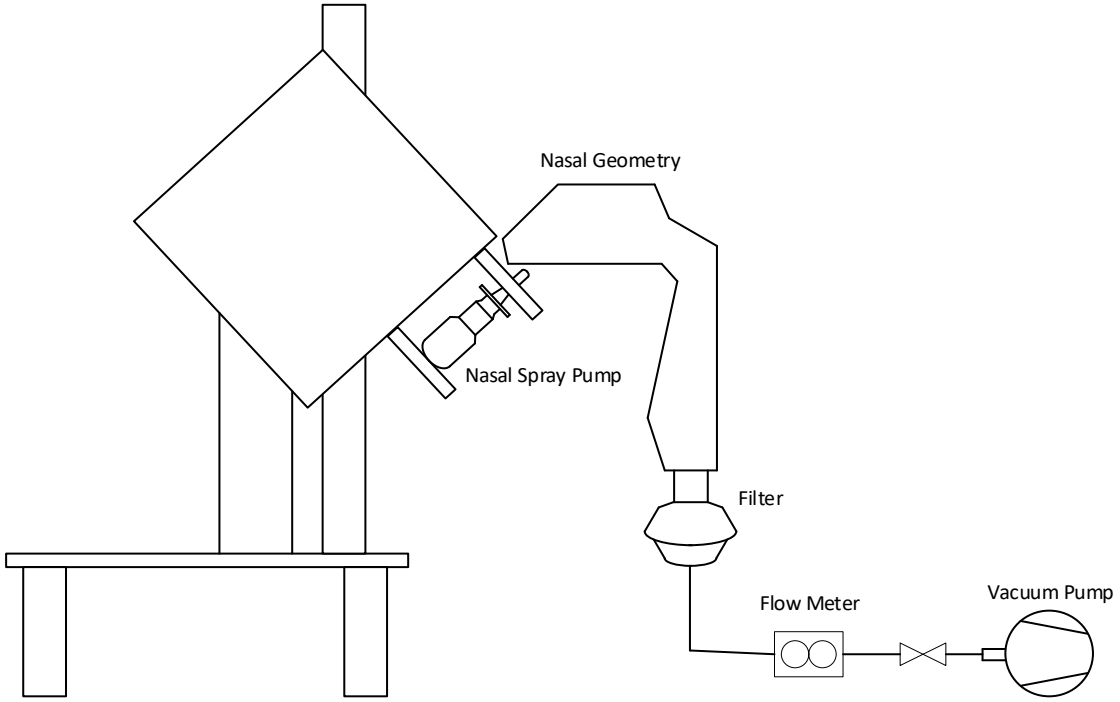

Figure 5.1. Schematic of experimental setup. Top indicates orientation of nasal spray pump; bottom indicates orientation of nasal spray pump or pMDI.

5.2.3 In vitro data analysis

Data are presented as the relative fraction of the total dose entering the AINI that deposits on each of the nasal surfaces and in the filter. In other words, the deposition fraction in a specific region was calculated by dividing the mass of drug deposited on each region by the difference between total mass of drug recovered and the mass collected from dripping or wiped from the benchtop or external surfaces of the AINI.

Since the AINI was constructed by an external collaborator, deposition in the aluminum AINI was also compared to the idealized geometry previously manufactured in plastic as described in Chen et al. (2020) [95].To facilitate comparison with available *in vivo* data from Leach et al. (2015), the Vestibule region of the AINI was identified with the *in vivo* Nose region, the combined AINI Turbinates and Olfactory region was identified with the *in vivo* combined Mid and Upper nasal region and the AINI Nasopharynx region was identified with the *in vivo* Throat region [96].

Welch's *t*-test was used to detect differences in average regional deposition data owing to material of construction (plastic vs. metal) and spray angle orientation (60° vs 45°), with $P < 0.05$ considered significant. Because *in vivo* variability in regional deposition was measured across individual patients, a statistical comparison with the *in vitro* data, with variability measured across repeats, was not possible.

5.3. Results

5.3.1. NasalCrom

Figure 5.2 shows comparisons of the regional deposition of NasalCrom in the metal AINI with previously published data taken using a plastic version of the same geometry and average *in vitro* regional deposition in a collection of realistic nasal airway replicas [95]. Figure 5.3 shows a comparison of the regional deposition profiles of NasalCrom in the AINI with *in vivo* deposition data published in Al-Ghananeem et al. (2008) [77]. The average total mass recovery from the AINI was 98.8% with a standard deviation of 2.4%. Differences observed between regional deposition in the metal and plastic versions of the

AINI were not statistically significant, indicating that the metal AINI is able to mimic *in vitro* regional deposition in a set of realistic nasal airway replicas as closely as the previously validated plastic idealized geometry. *In vivo* deposition was also closely matched by the AINI, with deposition falling between the 45° and 60° extremes.

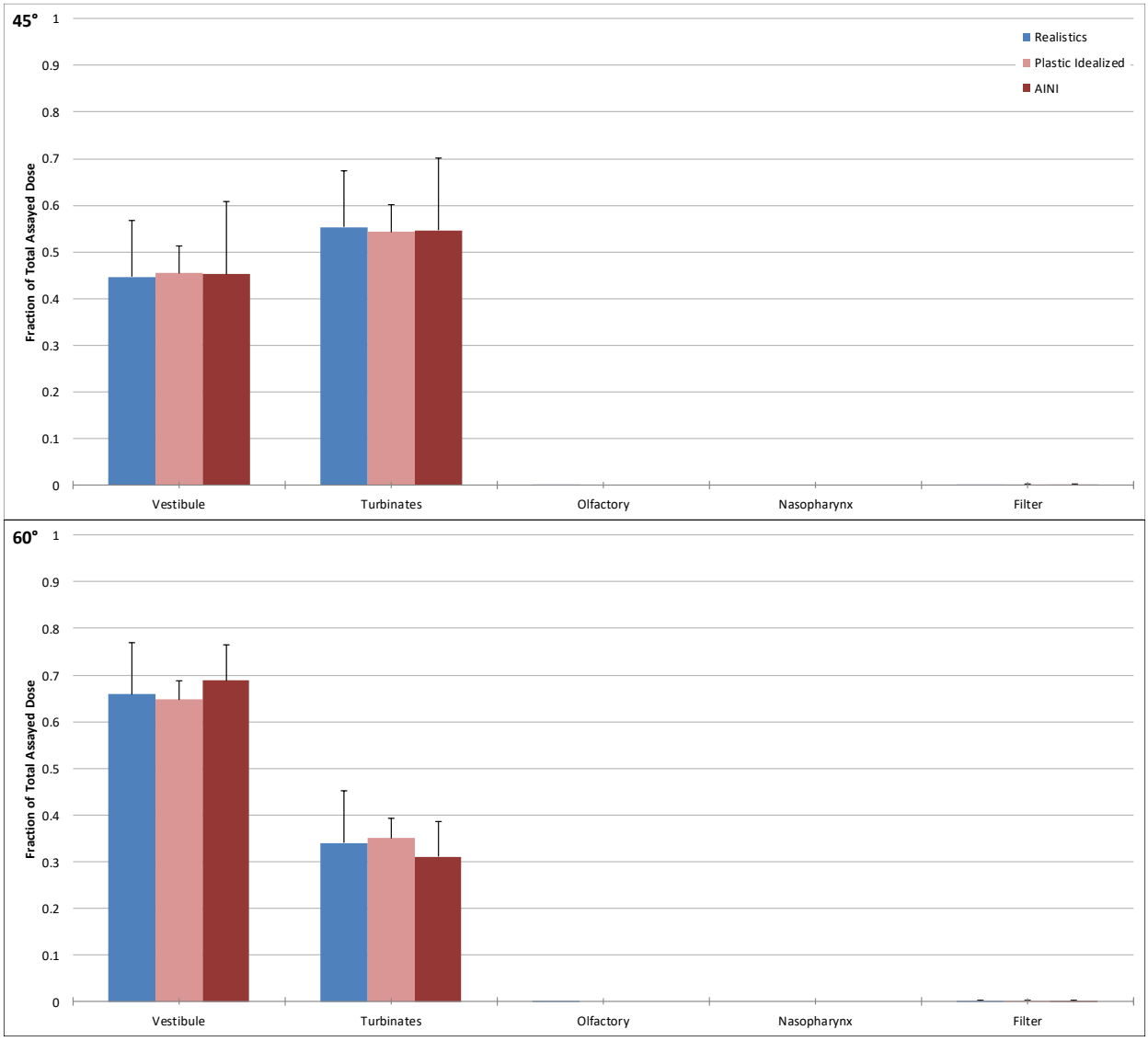

Figure 5.2. Comparison of regional deposition of NasalCrom in realistic vs. idealized geometries (n = 3 repeats for plastic idealized, n = 3 repeats for AINI, n = 9 nostrils for realistics). Error bars indicate one standard deviation (measured across geometries for realistics and across repeats for idealized).

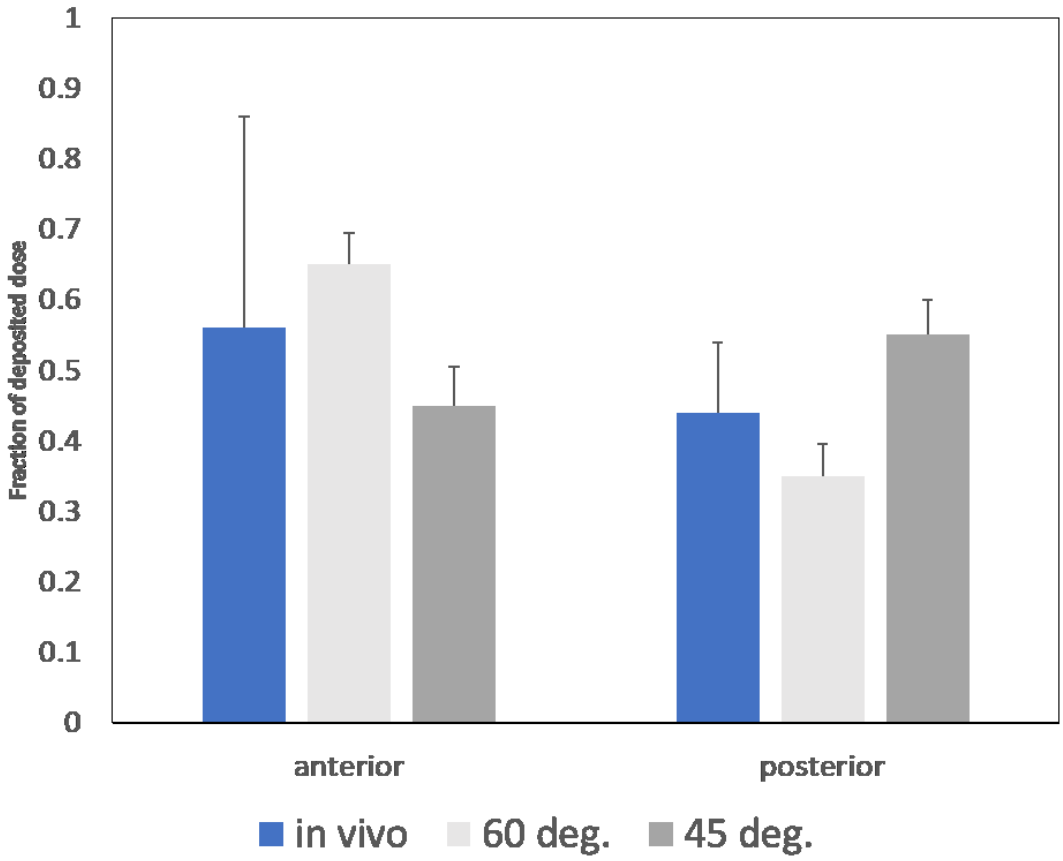

Figure 5.3. Comparison of regional deposition of NasalCrom in plastic AINI vs. *in vivo* (60° and 45°, n = 3 repeats for AINI, n = 9 nostrils for realistics). *In vivo* data taken from Al-Ghananeem et al. (2008) [77]. Note that administration angles *in vivo* were not reported. Error bars indicate one standard deviation (measured across repeats for AINI and across subjects for *in vivo*).

5.3.2. Nasonex

Figure 5.4 shows a comparison of Nasonex regional deposition in the AINI with available *in vivo* gamma scintigraphy data from Leach et al. (2015) at the 45° and the 60° orientations [96]. The average total mass recovery in the AINI was 95.1% with a standard deviation of 15.1%. Deposition at 60° was higher in the Vestibule of the AINI than at 45°, but owing to the large run to run variance, this difference was not statistically significant.

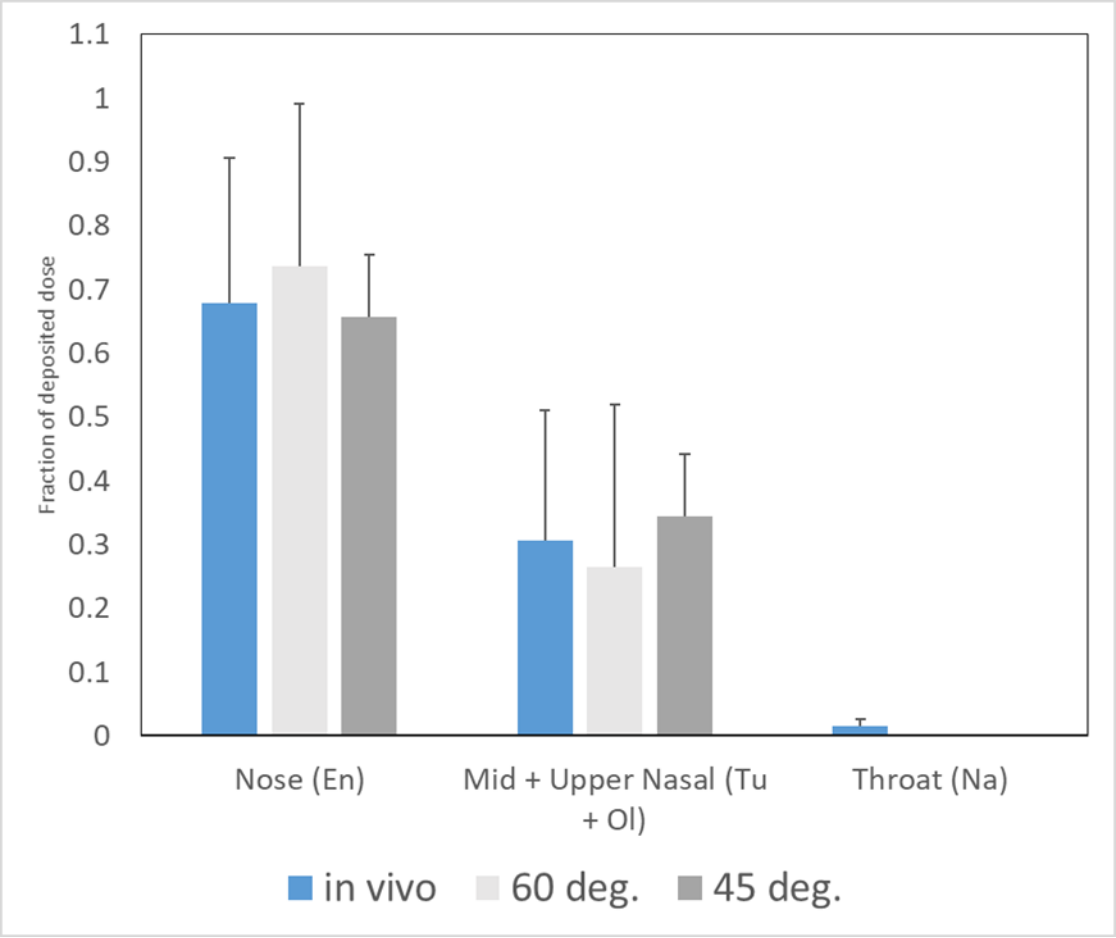

Figure 5.4. Comparison of regional deposition of Nasonex in plastic AINI vs. *in vivo* data as fraction of dose deposited in the nasal cavity (i.e. excluding filter deposition; 45° and 60°, n = 3 repeats for AINI, n = 9 subjects for *in vivo*). *In vivo* data taken from Leach et al. (2015) [96]. Note that administration angles *in vivo* were not reported. Ve = Vestibule; Tu = Turbinates; Ol = Olfactory; Na = Nasopharynx. Error bars indicate one standard deviation (measured across repeats for AINI and across subjects for *in vivo*).

5.3.3. QNASL

Figure 5.5 shows regional *in vitro* QNASL deposition in the AINI and Figure 5.6 shows a comparison of the regional deposition of QNASL in the AINI with available *in vivo* data from Leach et al. (2015) at the 45° and 60° orientations [96]. The average *in vitro* total mass recovery was 88.0% with a standard deviation of 11.2%. Although Figure 5.5 shows non-zero filter deposition, Figure 5.6 deposition fractions have been normalized for total nasal delivery (i.e. total non-filter dose) to maintain consistency with the *in vivo* data. With or without normalization, the 60° orientation resulted in consistently high Vestibule deposition, but no statistically significant differences were observed between the two spray orientation angles. Overall, given the *in vitro* run-to-run variability, the AINI was generally able to mimic the *in vivo* regional deposition pattern.

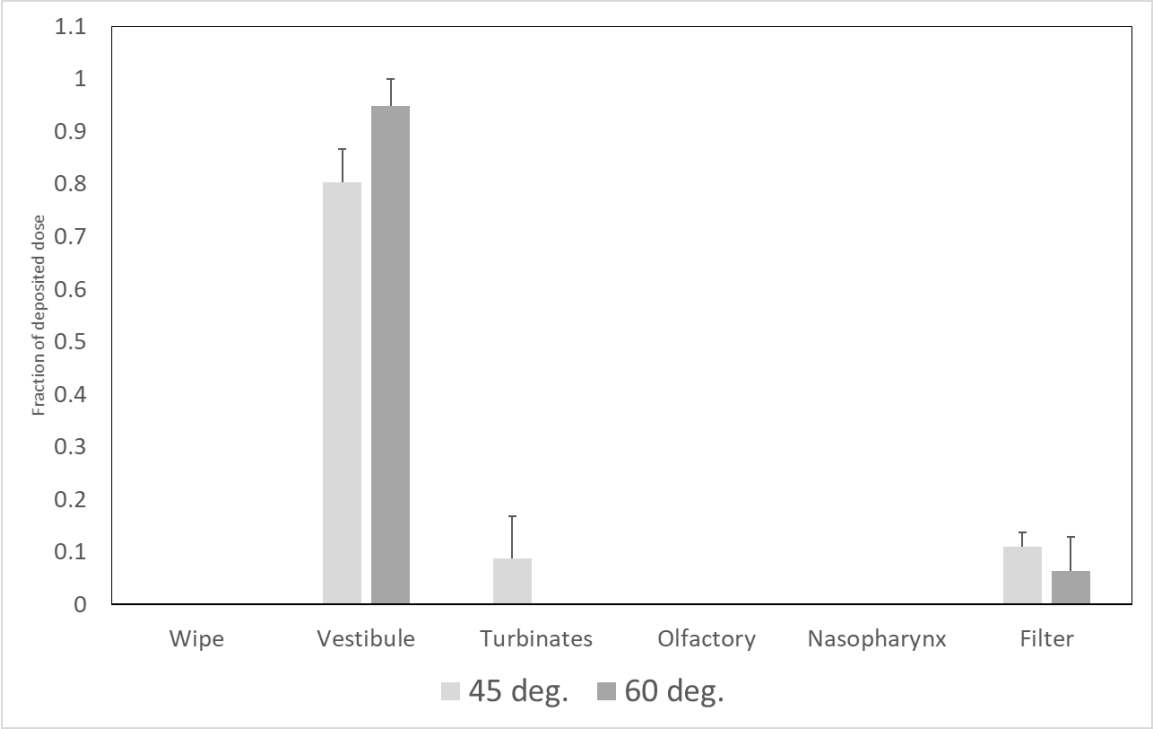

Figure 5.5. Regional deposition of QNASL in AINI as fraction of deposited dose (i.e. including filter deposition; 45° and 60°, n = 3 repeats for AINI). Error bars indicate one standard deviation (measured across repeats for AINI).

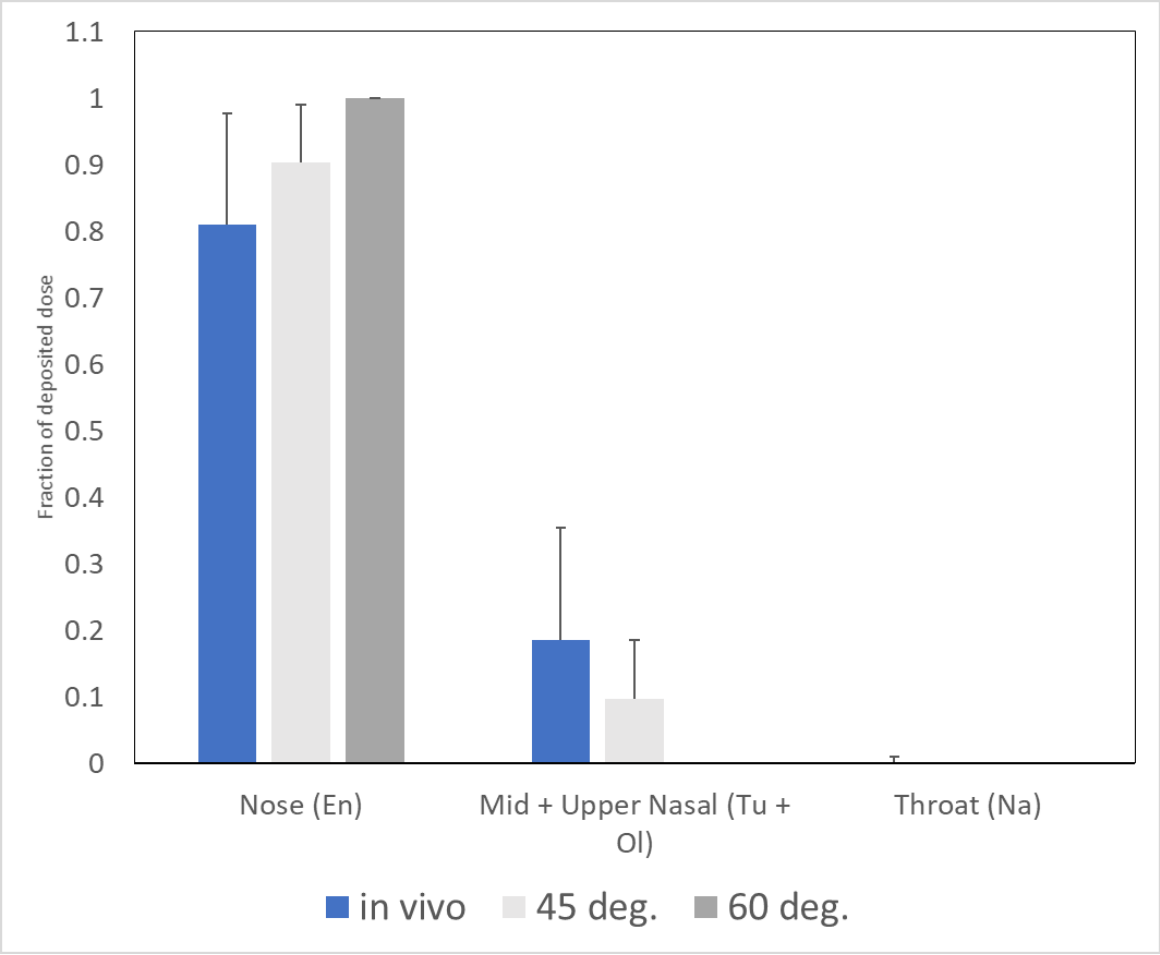

Figure 5.6. Comparison of regional deposition of QNASL in AINI vs. *in vivo* data as fraction of dose deposited in the nasal cavity (i.e. excluding filter deposition; 45° and 60°, n = 3 repeats for AINI, n = 8 subjects for *in vivo*). *In vivo* data taken from Leach et al. (2015) [96]. Note that administration angles *in vivo* were not reported. Ve = Vestibule; Tu = Turbinates; Ol = Olfactory; Na = Nasopharynx. Error bars indicate one standard deviation (measured across repeats for AINI and across subjects for *in vivo*).

5.4. Discussion

The objective of this study was to evaluate the *in vitro* performance of the AINI across a variety of nasal drug delivery products by comparing regional deposition profiles obtained from *in vitro* deposition experiments with corresponding profiles derived from previously published *in vivo* gamma scintigraphy data. Across the three devices and two spray angle orientations tested, *in vitro-in vivo* differences in deposition fractions in each individual anatomical region were not greater than 10 percentage points.

One broad trend that persisted across each of the three tested devices was the positive correlation between anterior deposition and the spray angle relative to the horizontal. This trend agrees with both the general *in vitro* literature, which has in general reported higher anterior deposition, and our previous publication utilizing the same geometry manufactured in plastic with NasalCrom as the test formulation [32,34,37,42,80,100].

As is evident from Figures 5.2 and 5.3, regional deposition fractions measured for Nasalcrom using the aluminum AINI agree with previously reported values obtained in a plastic version of the same geometry [95]. In addition, regional deposition fractions measured in the AINI matched average values previously measured across a set of realistic airway replicas at both angles of orientation, and were shown to mimic available *in vivo* deposition data for Nasalcrom (Figure 5.3).

The other two formulations, Nasonex (a suspension) and QNASL (a propellant-based formulation), were chosen as additional test formulations to determine the ability of the AINI to mimic *in vivo* regional deposition patterns for a wider range of nasal preparations

and devices. Figure 5.4 shows that the AINI was able to predict *in vivo* deposition of Nasonex well, with *in vivo* deposition in both the anterior and posterior nose lying between the respective values measured at the 60° and 45° orientations.

For QNASL, the *in vivo* data indicate that the bulk of deposition is concentrated strongly in the anterior region of the nose, a trend also reflected in the deposition pattern observed in the AINI. Notable here is the presence of a significant fraction of the delivered dose depositing on the filter, suggesting that a non-negligible portion of the dose is able to penetrate the nasal airways and possibly deposit in the lungs. Unfortunately, since lung deposition was not measured in Leach et al. (2015), it is impossible to confirm *in vivo* penetration to the lungs [96]. However, *in vitro* deposition experiments done in a nasal airway replica in the same study resulted in filter deposition of a magnitude similar to that found in the present study, which corroborates our findings and indicates the likely possibility of nonzero *in vivo* lung deposition [96]. Overall, notwithstanding factors such as the large variance *in vivo* and the differences in segmentation boundaries between the *in vivo* and *in vitro* cases that prevent an exact comparison, the AINI is able to broadly predict average *in vivo* regional deposition.

This being said, the present study is not without its limitations. As mentioned previously, the interior surfaces of the AINI are not designed to mimic the surface wetting properties of a human nasal cavity. Thus, differences may exist between *in vitro* and *in vivo* measurements in the amount of formulation dripping from the nostril post-actuation. In the present study, the fraction of the total delivered dose that dripped out of the Vestibule

region ranged from 0 to approximately 0.5 (i.e. half) for the aqueous formulations, while no drip was detected for QNASL. Given the above considerations, and owing to the high number of actuations necessary in some cases for UV-Vis spectroscopy, as well as to differing surface wetness and other factors *in vivo* and *in vitro*, the drip fraction was excluded when evaluating the ability of the AINI to mimic *in vivo* regional deposition.

The lack of a precisely standardized segmentation scheme of the nasal cavity *in vitro* and *in vivo* has also likely contributed to some of the differences observed in the *in vitro* and *in vivo* deposition patterns. Moreover, because the segmentation scheme used for the AINI is fixed, the utility of the AINI may vary depending on the aims of the end user, especially if more granular distinctions between different anatomical regions of the nasal cavity are desirable in certain applications. Finally, the AINI does not mimic dynamic changes of the nasal and oral airways throughout the breathing cycle. Thus, the AINI cannot be used to validate newer nasal drug delivery technologies that exploit such changes to improve delivery to the posterior nasal airways, for example by using changes in the soft palate during the breathing cycle to deliver drug to the nasal cavity from the back of the mouth during exhalation through the nose [18,101].

5.5. Conclusions

The main objective of this study was to validate the ability of the AINI to mimic the average regional deposition pattern in a range of nasal drug delivery products. Benchtop *in vitro* experiments were designed and conducted using the AINI, and the resulting regional deposition patterns were compared to previously reported *in vitro* data and available *in vivo*

data obtained using gamma scintigraphy. Good agreement was seen between regional deposition measured using the AINI and *in vivo* regional deposition patterns for all three nasal drug formulations that were tested. Therefore, *in vitro* testing incorporating the AINI may be useful in future intranasal drug delivery research and product development.

Chapter 6: Conclusions

6.1 Summary

The primary aim of this thesis was to extend the well-established practice of using nasal replicas in *in vitro* benchtop testing in two new areas. Thus, the thesis is broadly divided into two major arms, one focused on medical gas delivery, and the other focused on nasal spray deposition.

In the first arm of the thesis, realistic 3D printed nasal replicas, a fixture in drug development and the research of spray deposition in human airways, were introduced as a part of a novel benchtop testing methodology for quantifying and comparing the performance different supplemental oxygen delivery modalities. The development of this methodology was motivated primarily by the question of the equivalence between continuously delivered oxygen and pulsed oxygen delivered only during inhalation from a portable oxygen concentrator. Chapter 2 described this methodology in detail, which combines the realistic nasal replicas and real-time monitoring of inspired oxygen concentrations at the trachea during simulated tidal breathing through the replica. From this data, a volume-averaged tracheal FiO2 value could be calculated and used as a common standard of comparison between both continuous flow oxygen and pulse flow oxygen. Based on this value, pulse flow delivered consistently lower amounts of oxygen than continuous flow at flow rates equivalent to nominal pulse flow settings on a single portable oxygen concentrator. Based on pulse volumes and mass balance considerations, an algebraic equation predicting volume-averaged tracheal FiO2 was developed. Testing with a wide range of realistic nasal replicas also indicated that unlike with aerosol deposition in

the nose, inter-subject variability in the geometry of the nasal cavity did not result in large differences in volume-averaged tracheal FiO2. The ability to monitor the real-time oxygen concentration at the trachea also enabled identification of cases in which a portable oxygen concentrator can fail to trigger early enough or at all during inhalation, leading to incomplete delivery of the oxygen bolus or a complete inability to synchronize oxygen delivery with patient inspiratory effort. Chapter 3 extended the work done in Chapter 2 by using the previously described methodology to evaluate oxygen delivery in several commercially available portable oxygen concentrators against each other and against continuous flow oxygen. Anticipated clinically significant differences between pulse flow and continuous flow in L/min were observed at all nominally equivalent pulse flow settings higher than 2. Statistically significant differences in FiO2 were also identified between different portable oxygen concentrators operated at identical numerical pulse flow settings, with the clinically significant differences occurring at the highest settings. By coupling *in vitro* measurements with an *in silico* model of oxygen transport through the conducting airways, it was predicted that pulse flow is generally more efficient than continuous flow at delivering oxygen from the trachea to the alveolar acini, despite continuous flow delivering more oxygen overall. Significant differences in oxygen delivery persisted to the acini between portable oxygen concentrators operating at identical numerical settings.

In the second arm of the thesis, an idealized nasal replica, manufactured to mimic average regional deposition, was manufactured and validated using *in vitro* experiments against a set of realistic nasal replicas and against *in vivo* gamma scintigraphy data. The creation of a plastic version of this replica from a geometry previously designed using CFD was detailed

in Chapter 4, which also contains a description of the *in vitro* experiments executed to validate the ability of the replica to mimic averaged regional deposition in a set of realistic nasal replicas in a single nasal spray pump, and a comparison with available *in vivo* gamma scintigraphy data [46]. The plastic idealized replica was able to accurately reproduce average *in vitro* regional deposition patterns at two separate spray orientations in a set of realistic nasal airway replicas and good agreement with previously published *in vivo* gamma scintigraphy was observed. In Chapter 5, a metal version of the replica, called the Alberta Idealized Nasal Inlet (AINI) was used for further *in vitro* testing in a wider range of nasal spray products. The resulting regional deposition patterns were compared to *in vitro* data from Chapter 4 and previously published *in vivo* data obtained using gamma scintigraphy. Again, good agreement was seen between regional deposition measured using the AINI and *in vivo* regional deposition patterns for all three nasal drug formulations that were tested. Taken together, Chapters 4 and 5 demonstrate the viability of the AINI as a nasal replica that can predict average regional deposition across a range of nasal drug formulations. *In vitro* testing incorporating the AINI may be useful in future intranasal drug delivery research and product development.

6.2 Directions for future research

While the first arm of the thesis was able to achieve its stated objectives, the *in silico* modelling of oxygen transport presented in Chapter 3 cannot accurately account for rebreathing of gas from the anatomical dead space, and, while able to give an account of relative performance and efficiencies between different devices, cannot currently accurately predict *in vivo* FiO2. The model could be further extended to account for the full breathing

cycle, including a consideration of the exhaled gas remaining in the anatomical dead space, by combining it with a model for oxygen uptake at the alveoli. This would provide a more accurate prediction of *in vivo* oxygen concentrations over the course of the breath, which would in turn enable a more accurate calculation of the true FiO2 value observed *in vivo* which would include rebreathing of the gas present in the anatomical dead space.

With respect to the second arm of the thesis, further work can also be done in validating the AINI for a wider range of nasal drug delivery products, including one time use atomization and dry powder devices. Work with dry powders would also entail selection and optimization of a liquid coating agent to prevent particle bounce that does not occur in the mucous-lined airways of a human patient. A recently published study has also speculated that post-deposition motion caused by shear forces resulting from residual inspiratory effort may contribute to increased posterior deposition in the nasal cavity, and the AINI is well-equipped to systematically investigate the effect of inspiratory flow rate and formulation properties on this post deposition spreading phenomenon [102].

References

1. Tiwari G, Tiwari R, Sriwastawa B, Bhati L, Pandey P, Pandey S, et al. Drug delivery systems: An updated review. International Journal of Pharmaceutical Investigation. 2012;2:2.

2. Tepper DE. Nasal sprays for the treatment of migraine. Headache. 2013;53:577–8.

3. Taylor D, Radbruch L, Revnic J, Torres LM, Ellershaw JE, Perelman M. A Report on the Long-Term Use of Fentanyl Pectin Nasal Spray in Patients With Recurrent Breakthrough Pain. Journal of Pain and Symptom Management [Internet]. Elsevier Inc; 2013;47:1001–7. Available from: http://dx.doi.org/10.1016/j.jpainsymman.2013.07.012

4. Hagarty EM, Skorodin MS, Stiers WM, Mamdani MB, Jessen JA, Belingon EC. Performance of a Reservoir Nasal Cannula (Oxymizer) During Sleep in Hypoxemic Patients With COPD. Chest [Internet]. 1993;103:1129–34. Available from: https://linkinghub.elsevier.com/retrieve/pii/S0012369215418070

5. Griffiths MJD, Evans TW. Inhaled Nitric Oxide Therapy in Adults. New England Journal of Medicine [Internet]. 2005;353:2683–95. Available from: http://www.nejm.org/doi/abs/10.1056/NEJMra051884

6. U.S. Department of Health and Human Services, Food and Drug Administration Center for Drug Evaluation and Research D of DI (HFD-240). Draft: Guidance for Industry Bioavailability and Bioequivalence Studies for Nasal Aerosol and Nasal Sprays for Local Action. 2003; Available from: http://www.fda.gov/cder/guidance/index.htm

7. Pillay K, Chen JZ, Finlay WH, Martin AR. Inhaled nitric oxide: In vitro analysis of continuous flow noninvasive delivery via nasal cannula. Respiratory Care. 2021;66:228–39.

8. McCoy R. Oxygen-conserving techniques and devices. Respir Care [Internet]. 2000;45:95–104. Available from: https://pubmed.ncbi.nlm.nih.gov/10771785/

9. Bliss PL, McCoy RW, Adams AB. Characteristics of demand oxygen delivery systems: maximum output and setting recommendations. Respir Care. 2004;49:160–5.

10. Palwai A, Skowronski M, Coreno A, Drummond C, McFadden ER. Critical comparisons of the clinical performance of oxygen-conserving devices. American Journal of Respiratory and Critical Care Medicine. 2010;181:1061–71.

11. Gustafson JD, Yang S, Blakeman TC, Dorlac WC, Branson R. Pulsed dosed delivery of oxygen in mechanically ventilated pigs with acute lung injury. Journal of Trauma and Acute Care Surgery. 2013;75:775–9.

12. Blakeman TC, Rodriquez D, Britton TJ, Johannigman JA, Petro MC, Branson RD. Evaluation of oxygen concentrators and chemical oxygen generators at altitude and temperature extremes. Military Medicine. 2016;181:160–8.

13. Blakeman TC, Rodriquez D, Gerlach TW, Dorlac WC, Johannigman JA, Branson RD. Oxygen requirement to reverse altitude-induced hypoxemia with continuous flow and pulsed dose oxygen. Aerospace Medicine and Human Performance. 2015;86:351–6.

14. Wijkstra PJ, Guyatt GH, Ambrosino N, Celli BR, Güell R, Muir JF, et al. International approaches to the prescription of long-term oxygen therapy. European Respiratory Journal. 2001;18:909–13.

15. Grgic B, Finlay WH, Burnell PKP, Heenan AF. In vitro intersubject and intrasubject deposition measurements in realistic mouth-throat geometries. Journal of Aerosol Science. 2004;35:1025–40.

16. Laube BL. Devices for Aerosol Delivery to Treat Sinusitis. Journal of Aerosol Medicine. 2007;20:S5–18.

17. Aggarwal R, Cardozo A, Homer JJ. The assessment of topical nasal drug distribution. Clinical Otolaryngology and Allied Sciences. 2004;29:201–5.

18. Djupesland PG. Nasal drug delivery devices: Characteristics and performance in a clinical perspective-a review. Drug Delivery and Translational Research. 2013;3:42–62.

19. Miyake MM, Bleier BS. The blood-brain barrier and nasal drug delivery to the central nervous system. American Journal of Rhinology and Allergy. 2015;29:124–7.

20. Dhuria S v., Hanson LR, Frey WH. Intranasal delivery to the central nervous system: Mechanisms and experimental considerations. Journal of Pharmaceutical Sciences [Internet]. 2010;99:1654–73. Available from: https://linkinghub.elsevier.com/retrieve/pii/S0022354916304841

21. Newman SP, Pitcairn GR, Dalby RN. Drug Delivery to the Nasal Cavity: In Vitro and In Vivo Assessment. Critical Reviews in Therapeutic Drug Carrier Systems. 2004;21:46.

22. Li B v., Jin F, Lee SL, Bai T, Chowdhury, BadrulCaramenico HT, Conner DP. Bioequivalence for Locally Acting Nasal Spray and Nasal Aerosol Products: Standard Development and Generic Approval. The AAPS Journal. 2013;15:875–83.

23. Byron PR, Hindle M, Lange CF, Longest PW, McRobbie D, Oldham MJ, et al. In vivo-in vitro correlations: Predicting pulmonary drug deposition from pharmaceutical aerosols. Journal of Aerosol Medicine and Pulmonary Drug Delivery. 2010;23.

24. Sandeau J, Katz I, Fodil R, Louis B, Apiou-Sbirlea G, Caillibotte G, et al. CFD simulation of particle deposition in a reconstructed human oral extrathoracic airway for air and helium-oxygen mixtures. Journal of Aerosol Science [Internet]. Elsevier; 2010;41:281–94. Available from: http://dx.doi.org/10.1016/j.jaerosci.2009.12.001

25. Golshahi L, Vehring R, Noga ML, Finlay WH. In vitro deposition of micrometer-sized particles in the extrathoracic airways of children during tidal oral breathing. Journal of Aerosol Science [Internet]. Elsevier; 2013;57:14–21. Available from: http://dx.doi.org/10.1016/j.jaerosci.2012.10.006

26. Mygind N, Vesterhauge S. Aerosol distribution in the nose. Rhinology [Internet]. 1978;16:79–88. Available from: http://www.ncbi.nlm.nih.gov/pubmed/684327

27. Guilmette RA, Gagliano TJ. Construction of a Model of Human Nasal Airways Using <italic>In Vivo</italic> Morphometric Data. The Annals of Occupational Hygiene [Internet]. 1994;38:69–75. Available from: https://academic.oup.com/annweh/article/38/inhaled_particles_VII/69/209609/Construction-of-a-Model-of-Human-Nasal-Airways

28. Schroeter JD, Garcia GJM, Kimbell JS. Effects of surface smoothness on inertial particle deposition in human nasal models. Journal of Aerosol Science [Internet]. 2011;42:52–63. Available from: https://linkinghub.elsevier.com/retrieve/pii/S0021850210002223

29. Bliss PL, McCoy RW, Adams AB. A bench study comparison of demand oxygen delivery systems and continuous flow oxygen. Respiratory Care. 1999;44:925–31.

30. Zhou S, Chatburn RL. Effect of the anatomic reservoir on Low-Flow oxygen delivery via nasal cannula: Constant flow versus pulse flow with portable oxygen concentrator. Respiratory Care. 2014;59:1199–209.

31. Cheng YS, Holmes TD, Gao J, Guilmette RA, Li S, Surakitbanharn Y, et al. Characterization of Nasal Spray Pumps and Deposition Pattern in a Replica of the Human Nasal Airway. Journal of Aerosol Medicine. 2002;14:267–80.

32. Foo MY, Cheng Y-S, Su W-C, Donovan MD. The Influence of Spray Properties on Intranasal Deposition. Journal of Aerosol Medicine. 2007;20:495–508.

33. Guo Y, Laube B, Dalby R. The effect of formulation variables and breathing patterns on the site of nasal deposition in an anatomically correct model. Pharmaceutical Research. 2005;22:1871–8.

34. Kundoor V, Dalby RN. Assessment of nasal spray deposition pattern in a silicone human nose model using a color-based method. Pharmaceutical Research. 2010;27:30–6.

35. Kundoor V, Dalby RN. Effect of formulation- and administration-related variables on deposition pattern of nasal spray pumps evaluated using a nasal cast. Pharmaceutical Research. 2011;28:1895–904.

36. Pu Y, Goodey AP, Fang X, Jacob K. A comparison of the deposition patterns of different nasal spray formulations using a nasal cast. Aerosol Science and Technology. 2014;48:930–8.

37. Xi J, Wang Z, Nevorski D, Zhou Y, Yuan JE, Zhang Y. Visualization and Quantification of Nasal and Olfactory Deposition in a Sectional Adult Nasal Airway Cast. Pharmaceutical Research. 2016;33:1527–41.

38. Xi J, Wang Z, Nevorski D, White T, Zhou Y. Nasal and Olfactory Deposition with Normal and Bidirectional Intranasal Delivery Techniques: In Vitro Tests and Numerical Simulations. Journal of Aerosol Medicine and Pulmonary Drug Delivery. 2016;30:118–31.

39. Kelly JT, Asgharian B, Kimbell JS, Wong BA. Particle Deposition in Human Nasal Airway Replicas Manufactured by Different Methods. Part I: Inertial Regime Particles. Aerosol Science and Technology. 2011;38:1063–71.

40. Swift DL, Montassier N, Hopke PK, Karpen-Hayes K, Cheng Y-S, Yin Fong Su, et al. Inspiratory deposition of ultrafine particles in human nasal replicate cast. Journal of Aerosol Science [Internet]. 1992;23:65–72. Available from: http://linkinghub.elsevier.com/retrieve/pii/002185029290318P

41. Schroeter JD, Tewksbury EW, Wong BA, Kimbell JS. Experimental Measurements and Computational Predictions of Regional Particle Deposition in a Sectional Nasal Model. Journal of Aerosol Medicine and Pulmonary Drug Delivery. 2014;28:20–9.

42. Hughes R, Watterson J, Dickens C, Ward D, Banaszek A. Development of a nasal cast model to test medicinal nasal devices. Proceedings of the Institution of Mechanical Engineers, Part H: Journal of Engineering in Medicine. 2008;222:1013–22.

43. Shah SA, George C, Berger R, Gupta P, Wan J, Connor A, et al. In Vivo Nasal Deposition from Different Delivery Devices and Formulations. International Pharmaceutical Aerosol Consortium on Regulation & Science Conference. 2011. p. 2.

44. Shah SA, Dickens CJ, Ward DJ, Banaszek AA, George C, Horodnik W. Design of Experiments to Optimize an In Vitro Cast to Predict Human Nasal Drug Deposition. Journal of Aerosol Medicine and Pulmonary Drug Delivery. 2013;27:21–9.

45. Liu Y, Johnson MR, Matida EA, Kherani S, Marsan J. Creation of a standardized geometry of the human nasal cavity. Journal of Applied Physiology. 2009;106:784–95.

46. Kiaee M, Wachtel H, Noga ML, Martin AR, Finlay WH. An idealized geometry that mimics average nasal spray deposition in adults: A computational study. Computers in Biology and Medicine [Internet]. 2019;107:206–17. Available from: https://linkinghub.elsevier.com/retrieve/pii/S0010482519300605

47. Yáñez AM, Prat JP, Álvarez-Sala JL, Calle M, Lobato SD, Gonzalez JLG, et al. Oxygenation with a single portable pulse-dose oxygen-conserving device and combined

stationary and portable oxygen delivery devices in subjects with COPD. Respiratory Care. 2015;60:382–7.

48. Manual P. FreeStyle ™ Portable Oxygen Concentrator.

49. Katz I, Pichelin M, Montesantos S, Kang MY, Sapoval B, Zhu K, et al. An in silico analysis of oxygen uptake of a mild COPD patient during rest and exercise using a portable oxygen concentrator. International Journal of COPD. 2016;11:2427–34.

50. Garrod R, Bestall JC, Paul E, Wedzicha JA. Evaluation of pulsed dose oxygen delivery during exercise in patients with severe chronic obstructive pulmonary disease. Thorax. 1999;54:242–4.

51. Carter R, Tashkin D, Djahed B, Hathaway E, Nicotra MB, Tiep BL. Demand oxygen delivery for patients with restrictive lung disease. Chest. 1989;96:1307–11.

52. Braun SR, Spratt G, Scott GC, Ellersieck M. Comparison of six oxygen delivery systems for COPD patients at rest and during exercise. Chest [Internet]. The American College of Chest Physicians; 1992;102:694–8. Available from: http://dx.doi.org/10.1378/chest.102.3.694

53. Chatburn RL, Williams TJ. Performance comparison of 4 portable oxygen concentrators. Respiratory Care. 2010;55:433–42.

54. Martin AR, Katz IM, Lipsitz Y, Terzibachi K, Caillibotte G, Texereau J. Methods for evaluation of helium/oxygen delivery through non-rebreather facemasks. Medical Gas Research. 2012;2:31.

55. Golshahi L, Noga ML, Thompson RB, Finlay WH. In vitro deposition measurement of inhaled micrometer-sized particles in extrathoracic airways of children and adolescents during nose breathing. Journal of Aerosol Science [Internet]. Elsevier; 2011;42:474–88. Available from: http://dx.doi.org/10.1016/j.jaerosci.2011.04.002

56. Finlay WH. The Mechanics of Inhaled Pharmaceutical Aerosols. 2nd ed. Elsevier; 2019.

57. Knoch M, Wunderlich E. Effect of Age Related Breathing Parameters on the Performance of a New Nebulizer System: An In-Vitro Study. Journal of Aerosol Medicine: Deposition, Clearance, and Effects in the Lung. 1995;8:285–8.

58. Coates AL, MacNeish CF, Allen PD, Ho SL, Lands LC. Do sinusoidal models of respiration accurately reflect the respiratory events of patients breathing on nebulizers? Journal of Aerosol Medicine: Deposition, Clearance, and Effects in the Lung. 1999;12:265–73.

59. Prokop RM, Finlay WH, Stapleton KW. An in vitro technique for calculating the regional dosages of drugs delivered by an ultrasonic nebulizer. Journal of Aerosol Science. 1995;26:847–60.

60. Weber A, Morlin G, Cohen M, Williams-Warren J, Ramsey B, Smith A. Effect of nebulizer type and antibiotic concentration on device performance. Pediatric Pulmonology [Internet]. 1997;23:249–60. Available from: https://onlinelibrary.wiley.com/doi/10.1002/(SICI)1099-0496(199704)23:4%3C249::AID-PPUL2%3E3.0.CO;2-H

61. Langer AW, Hutchenson JS, Charlton JD, McCubbin JA, Orist PA, Stoney CM. On-Line Minicomputerized Measurement of Cardiopulmonary Function On a Breath-By-Breath Basis. Psychophysiology [Internet]. 1985;22:50–7. Available from: https://onlinelibrary.wiley.com/doi/10.1111/j.1469-8986.1985.tb01560.x

62. Chatila W, Nugent T, Vance G, Gaughan J, Criner GJ. The effects of high-flow vs low-flow oxygen on exercise in advanced obstructive airways disease. Chest. 2004;126:1108–15.

63. Hudgel DW, Martin RJ, Capehart M, Johnson B, Hill P. Contribution of hypoventilation to sleep oxygen desaturation in chronic obstructive pulmonary disease. Journal of Applied Physiology Respiratory Environmental and Exercise Physiology. 1983;55:669–77.

64. C.P. M, W. F. Investigating intersubject variability in pulsed oxygen delivery using adult nasal airway replicas. American Journal of Respiratory and Critical Care Medicine [Internet]. 2015;191:150. Available from: http://www.atsjournals.org/doi/pdf/10.1164/ajrccm-conference.2015.191.1_MeetingAbstracts.A5811%0Ahttp://ovidsp.ovid.com/ovidweb.cgi?T=JS&PAGE=reference&D=emed17&NEWS=N&AN=72053709

65. Waldau T, Larsen VH, Bonde J. Evaluation of five oxygen delivery devices in spontaneously breathing subjects by oxygraphy. Anaesthesia. 1998;53:256–63.

66. Wettstein RB, Shelledy DC, Peters JI. Delivered oxygen concentrations using low-flow and high-flow nasal cannulas. Respiratory Care. 2005;50:604–9.

67. Casaburi R. Assessing the dose of supplemental oxygen: Let us compare methodologies. Respiratory Care. 2005;50:594–5.

68. Croxton TL, Bailey WC. Long-term oxygen treatment in chronic obstructive pulmonary disease: recommendations for future research: An NHLBI workshop report. American Journal of Respiratory and Critical Care Medicine. 2006;174:373–8.

69. Lacasse Y, Tan A-YM, Maltais F, Krishnan JA. Home Oxygen in Chronic Obstructive Pulmonary Disease. American Journal of Respiratory and Critical Care Medicine [Internet]. 2018;197:1254–64. Available from: https://www.atsjournals.org/doi/10.1164/rccm.201802-0382CI

70. Tiep B. Portable oxygen therapy with oxygen conserving devices and methodologies. Monaldi Arch Chest Dis [Internet]. 1995;50:51–7. Available from: http://www.ncbi.nlm.nih.gov/pubmed/7742825

71. Chen JZ, Katz IM, Pichelin M, Zhu K, Caillibotte G, Noga ML, et al. Comparison of pulsed versus continuous oxygen delivery using realistic adult nasal airway replicas. International Journal of COPD. 2017;12:2559–71.

72. Martin AR, Jackson C, Katz IM, Caillibotte G. Variability in uptake efficiency for pulsed versus constant concentration delivery of inhaled nitric oxide. Medical Gas Research [Internet]. Medical Gas Research; 2014;4:1–13. Available from: Medical Gas Research

73. Phillips CG, Kaye SR, Schroter RC. A diameter-based reconstruction of the branching pattern of the human bronchial tree Part I. Description and application. Respiration

Physiology [Internet]. 1994;98:193–217. Available from: https://linkinghub.elsevier.com/retrieve/pii/0034568794000425

74. Liu Y, Matida EA, Johnson MR. Experimental measurements and computational modeling of aerosol deposition in the Carleton-Civic standardized human nasal cavity. Journal of Aerosol Science [Internet]. Elsevier; 2010;41:569–86. Available from: http://dx.doi.org/10.1016/j.jaerosci.2010.02.014

75. Kiaee M, Wachtel H, Noga ML, Martin AR, Finlay WH. Regional deposition of nasal sprays in adults: A wide ranging computational study. International Journal for Numerical Methods in Biomedical Engineering. 2018;34:1–13.

76. Darunkola MK. Simulation of Spray Deposition in Adults Nasal Airway. 2018.

77. Al-Ghananeem AM, Sandefer EP, Doll WJ, Page RC, Chang Y, Digenis GA. Gamma scintigraphy for testing bioequivalence: A case study on two cromolyn sodium nasal spray preparations. International Journal of Pharmaceutics. 2008;357:70–6.

78. Doughty D v., Vibbert C, Kewalramani A, Bollinger ME, Dalby RN. Automated actuation of nasal spray products: determination and comparison of adult and pediatric settings. Drug Development and Industrial Pharmacy. 2010;37:359–66.

79. Inthavong K, Fung MC, Yang W, Tu J. Measurements of Droplet Size Distribution and Analysis of Nasal Spray Atomization from Different Actuation Pressure. Journal of Aerosol Medicine and Pulmonary Drug Delivery. 2014;28:59–67.

80. Warnken ZN, Smyth HDC, Davis DA, Weitman S, Williams RO, Kuhn JG. Personalized Medicine in Nasal Delivery: The Use of Patient-Specific Administration Parameters To Improve Nasal Drug Targeting Using 3D-Printed Nasal Replica Casts. Molecular Pharmaceutics. 2018;15:1392–402.

81. Frank DO, Kimbell JS, Cannon D, Pawar SS, Rhee JS. Deviated nasal septum hinders intranasal sprays: a computer simulation study. Rhinology [Internet]. 2012;50:311–8. Available from: http://www.ncbi.nlm.nih.gov/pubmed/22888490

82. Frank DO, Kimbell JS, Cannon D, Rhee JS. Computed intranasal spray penetration: comparisons before and after nasal surgery. Int Forum Allergy Rhinol [Internet]. 2013;3:48–55. Available from: http://www.ncbi.nlm.nih.gov/pubmed/22927179

83. Dayal P, Shaik MS, Singh M. Evaluation of different parameters that affect droplet-size distribution from nasal sprays using the Malvern Spraytec®. Journal of Pharmaceutical Sciences [Internet]. Elsevier Masson SAS; 2004;93:1725–42. Available from: http://dx.doi.org/10.1002/jps.20090

84. Lelong N, Junqua-Moullet A, Diot P, Vecellio L. Comparison of Laser Diffraction Measurements by Mastersizer X and Spraytec to Characterize Droplet Size Distribution of Medical Liquid Aerosols. Journal of Aerosol Medicine and Pulmonary Drug Delivery. 2013;27:94–102.

85. Below A, Bickmann D, Breitkreutz J. Assessing the performance of two dry powder inhalers in preschool children using an idealized pediatric upper airway model. International Journal of Pharmaceutics. Elsevier B.V.; 2013;444:169–74.

86. Javaherin E, Golshahi L, Finlaynn WH. An idealized geometry that mimics average infant nasal airway deposition. Journal of Aerosol Science. Elsevier; 2013;55:137–48.

87. Delvadia RR, Longest PW, Byron PR. In vitro tests for aerosol deposition. i: Scaling a physical model of the upper airways to predict drug deposition variation in normal humans. Journal of Aerosol Medicine and Pulmonary Drug Delivery. 2012;25:32–40.

88. Golshahi L, Finlay WH. An idealized child throat that mimics average pediatric oropharyngeal deposition. Aerosol Science and Technology. 2012;46.

89. Ruzycki CA, Murphy B, Nathoo H, Finlay WH, Martin AR. Combined in Vitro-in Silico Approach to Predict Deposition and Pharmacokinetics of Budesonide Dry Powder Inhalers. Pharmaceutical Research. Pharmaceutical Research; 2020;37.

90. Ruzycki CA, Martin AR, Finlay WH. An Exploration of Factors Affecting in Vitro Deposition of Pharmaceutical Aerosols in the Alberta Idealized Throat. Journal of Aerosol Medicine and Pulmonary Drug Delivery. 2019;32:405–17.

91. Garcia GJM, Tewksbury EW, Wong BA, Kimbell JS. Interindividual Variability in Nasal Filtration as a Function of Nasal Cavity Geometry. Journal of Aerosol Medicine and Pulmonary Drug Delivery [Internet]. 2009;22:139–56. Available from: http://www.liebertpub.com/doi/10.1089/jamp.2008.0713

92. Basu S, Holbrook LT, Kudlaty K, Fasanmade O, Wu J, Burke A, et al. Numerical evaluation of spray position for improved nasal drug delivery. Scientific Reports [Internet]. 2020;10:10568. Available from: http://www.nature.com/articles/s41598-020-66716-0

93. Foo MY, Sawant N, Overholtzer E, Donovan MD. A Simplified Geometric Model to Predict Nasal Spray Deposition in Children and Adults. AAPS PharmSciTech. AAPS PharmSciTech; 2018;19:2767–77.

94. T. Schönbrodt et al. Method development for deposition studies in a nasal cast. In: R.N. Dalby, editor. Respiratory Drug Delivery 2010. Orlando Florida: Davies Healthcare International Publishing; 2010. p. 445–449.

95. Chen JZ, Kiaee M, Martin AR, Finlay WH. In vitro assessment of an idealized nose for nasal spray testing: Comparison with regional deposition in realistic nasal replicas. International Journal of Pharmaceutics [Internet]. Elsevier; 2020;582:119341. Available from: https://doi.org/10.1016/j.ijpharm.2020.119341

96. Leach CL, Kuehl PJ, Chand R, McDonald JD. Nasal Deposition of HFA-Beclomethasone, Aqueous Fluticasone Propionate and Aqueous Mometasone Furoate in Allergic Rhinitis Patients. Journal of Aerosol Medicine and Pulmonary Drug Delivery. 2015;28:334–40.

97. Ciciliani AM, Langguth P, Wachtel H. Handling forces for the use of different inhaler devices. International Journal of Pharmaceutics. Elsevier; 2019;560:315–21.

98. Young PM, Price R. Comparative measurements of pressurised metered dose inhaler (pMDI) stem displacement. Drug Development and Industrial Pharmacy. 2008;34:90–4.

99. Nakada H, Aomori T, Mochizuki M. Effect of a lever aid on hand strength required for using a handheld inhaler correctly. International Journal of Pharmaceutics. Elsevier B.V.; 2021;596:120249.

100. Inthavong K, Tian ZF, Li HF, Tu J, Yang W, Xue CL, et al. A numerical study of spray particle deposition in a human nasal cavity. Aerosol Science and Technology. 2006;40:1034–45.

101. Kleven M, Melaaen MC, Reimers M, Røtnes JS, Aurdal L, Djupesland PG. Using Computational Fluid Dynamics (CFD) to Improve the Bi-Directional Nasal Drug Delivery Concept. Food and Bioproducts Processing [Internet]. 2005;83:107–17. Available from: https://linkinghub.elsevier.com/retrieve/pii/S0960308505704740

102. Sosnowski TR, Rapiejko P, Sova J, Dobrowolska K. Impact of physicochemical properties of nasal spray products on drug deposition and transport in the pediatric nasal cavity model. International Journal of Pharmaceutics. Elsevier; 2020;574:118911.

103. Agusti AGN, Barbera JA, Roca J, Wagner PD, Guitart R, Rodriguez-Roisin R. Hypoxic pulmonary vasoconstriction and gas exchange during exercise in chronic obstructive pulmonary disease. Chest. 1990;97:268–75.

104. Finlay WH. The Mechanics of Inhaled Pharmaceutical Aerosols. 2nd ed. Elsevier; 2019.

105. Katz I, Caillibotte G, Martin AR, Arpentinier P. Property value estimation for inhaled therapeutic binary gas mixtures: He, Xe, N2O, and N2with O2. Medical Gas Research

[Internet]. BioMed Central Ltd; 2011;1:28. Available from:

http://www.medicalgasresearch.com/content/1/1/28

Appendix A

These airway lengths and diameters can be scaled for different FRC values using the following equation:[15]

$$l = l_0 (FRC/FRC_0)^{1/3} \quad (3)$$

where l_0 is the unscaled dimension for FRC_0 = 3000 mL, *FRC* is the new volume basis for scaling, and *l* is the new scaled airway dimension.

For the present study, FRC = 3845 mL was chosen based on values from Agusti et al. (1990) for COPD patients at rest and during exercise [103].

Dispersion of oxygen through the airways was characterized according to the framework given in Finlay (2019) and developed in Martin et al. (2014) [72,104]. Briefly, the equation modelling dispersion and transport through the airways is a 1-dimensional convection-diffusion partial differential equation and can be written as:

$$A(\partial c/\partial t) = \partial/\partial t(AD_{eff}\partial c/\partial t) - \partial/\partial x(Acu) \quad (4)$$

where *A* is the total cross-sectional area of the airways at a given depth in the lung *x*, *t* is time, *u* and *c* are the average velocity and oxygen concentration, respectively, over the cross-section of the airway and D_{eff} is an effective diffusion coefficient (measure of dispersion of gas along the direction of flow) taking into consideration both molecular diffusion and other dispersion phenomena arising from non-uniform velocity and concentration profiles in the airway.

Through most of the conducting airways, D_{eff} may be defined as:

$$D_{eff} = \alpha u d \quad (5)$$

where d is the diameter of the airway and $\alpha = 1.08$ for inspiration. In the small airways approaching the acinar region, the molecular diffusivity of oxygen in air becomes significant. In these regions, the molecular diffusion coefficient of oxygen in air at 37°C is given as $D_m = 0.2206$ cm^2/s [105].

Equation (4) was discretized over finite divisions of length using an upwind approximation for the convective term and a central difference approximation for the diffusive term [72].[15]

Concentrations were then advanced in time explicitly using the Euler method. Based on previous grid size dependence studies, a grid size of 5 divisions per airway generation was chosen [72]. For such a grid size, it was previously found that 5000 time steps per breath were necessary to ensure convergence [72].